172(1), 2018

COMBUSTION ENGINES

Poznan University of Technology

Institute of Combustion Engines and Transport

POLAND, 60-965 Poznan, Piotrowo 3 str., tel. 48 61 6652207, fax. 48 61 6652204

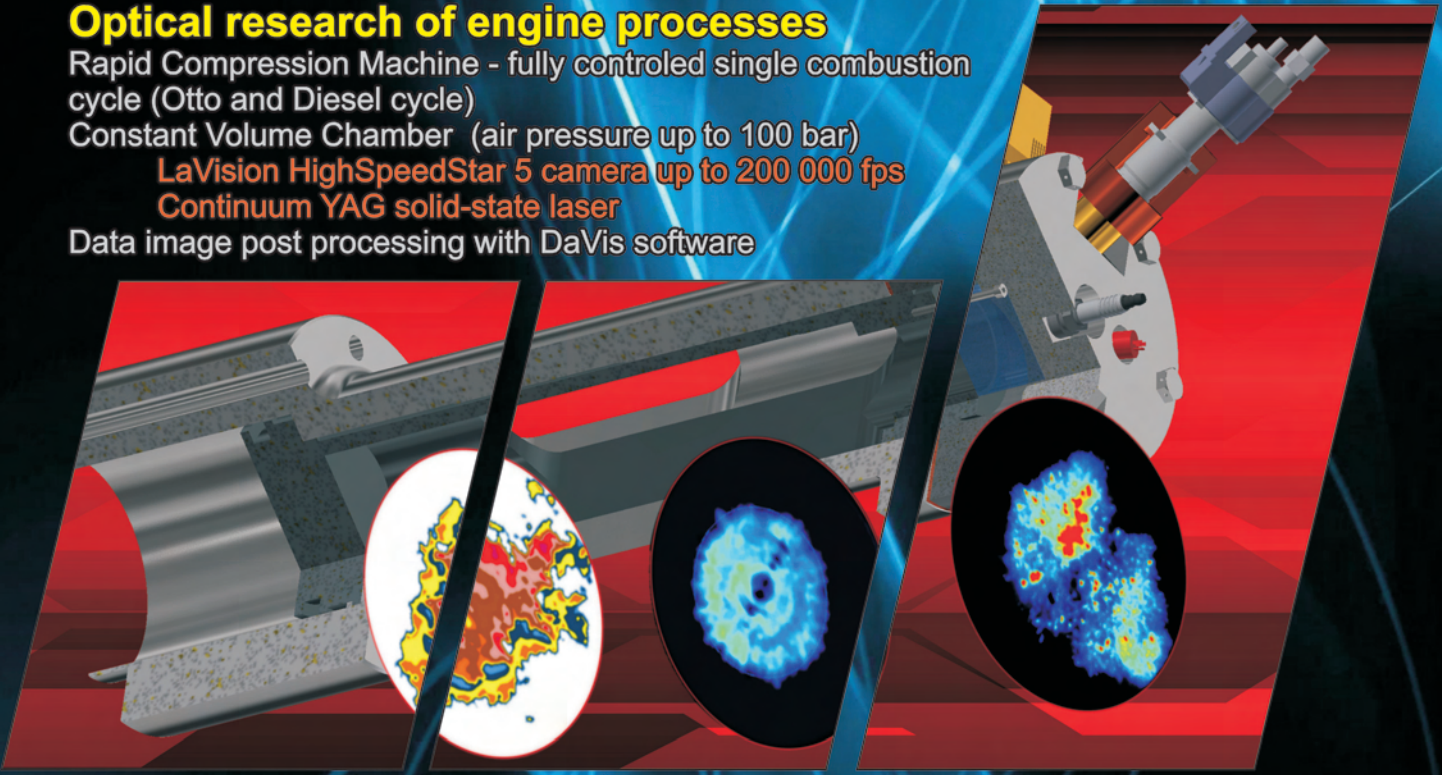

Optical research of engine processes

Rapid Compression Machine - fully controled single combustion cycle (Otto and Diesel cycle)

Constant Volume Chamber (air pressure up to 100 bar)

- LaVision HighSpeedStar 5 camera up to 200 000 fps
- Continuum YAG solid-state laser

Data image post processing with DaVis software

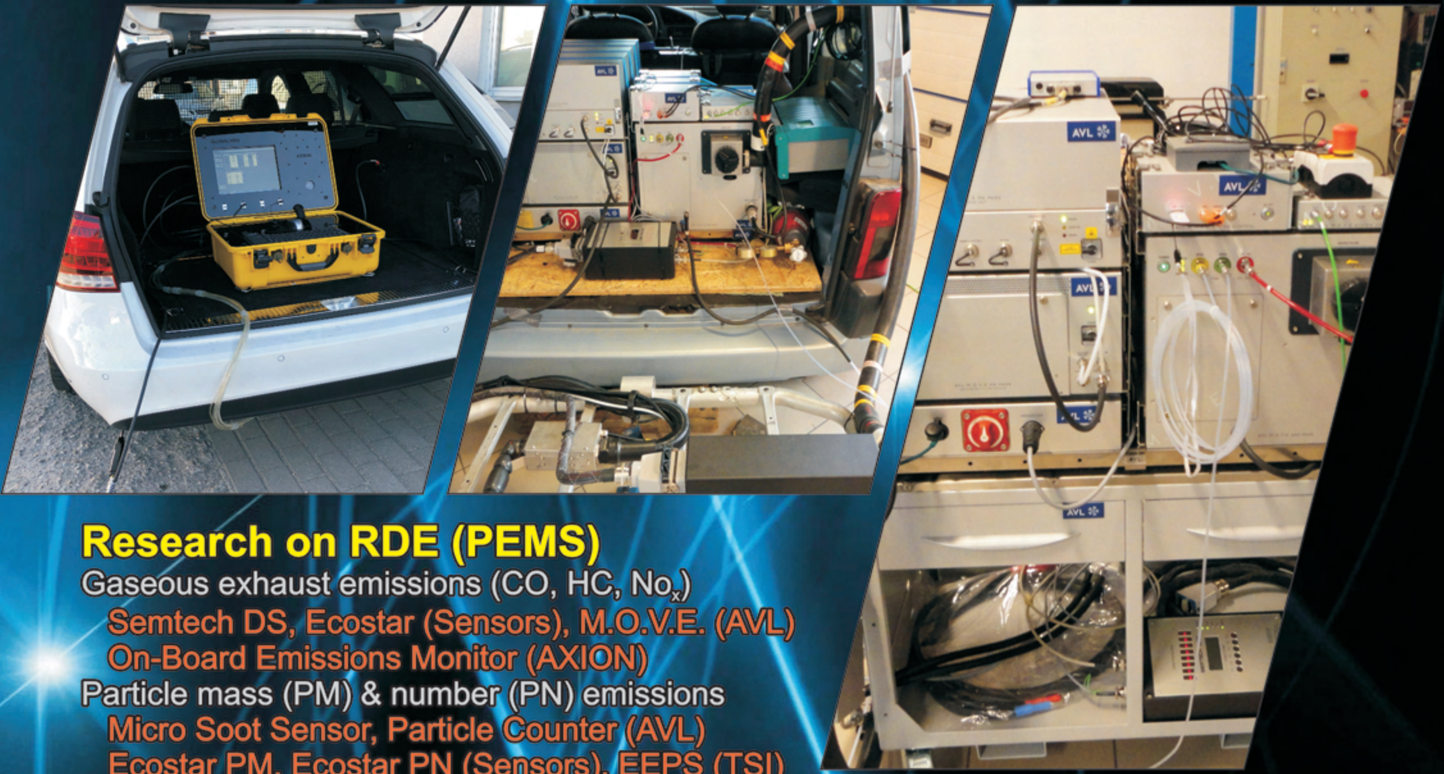

Research on RDE (PEMS)

Gaseous exhaust emissions (CO, HC, No_x)

- Semtech DS, Ecostar (Sensors), M.O.V.E. (AVL)
- On-Board Emissions Monitor (AXION)

Particle mass (PM) & number (PN) emissions

- Micro Soot Sensor, Particle Counter (AVL)
- Ecostar PM, Ecostar PN (Sensors), EEPS (TSI)

www.cel.put.poznan.pl

PTNSS Supporting Members
Członkowie wspierający PTNSS

BOSMAL Automotive Research and Development Institute Ltd
Instytut Badań i Rozwoju Motoryzacji BOSMAL Sp. z o.o

Motor Transport Institute
Instytut Transportu Samochodowego

The Institute for Sustainable Technologies
Instytut Technologii Eksploatacji

Institute of Aviation
Instytut Lotnictwa

Automotive Industry Institute
Przemysłowy Instytut Motoryzacji

The Rail Vehicles Institute TABOR
Instytut Pojazdów Szynowych TABOR

Institute of Mechanised Construction and Rock Mining
Instytut Mechanizacji Budownictwa i Górnictwa Skalnego

Institute of Logistics and Warehousing
Instytut Logistyki i Magazynowania

Industrial Institute of Agricultural Engineering
Przemysłowy Instytut Maszyn Rolniczych

AVL List GmbH

Solaris Bus & Coach S.A.

Air Force Institute of Technology
Instytut Techniczny Wojsk Lotniczych

COMBUSTION ENGINES

A Scientific Magazine
2018, 172(1)
Year LVII
PL ISSN 2300-9896

Editor:
Polskie Towarzystwo Naukowe Silników Spalinowych
43-300 Bielsko-Biała, Sarni Stok 93 Street, Poland
tel.: +48 33 8130402, fax: +48 33 8125038
E-mail: sekretariat@ptnss.pl
WebSite: http://www.ptnss.pl
Papers available on-line: http://combustion-engines.eu

Editorial:
Institute of Combustion Engines and Transport
Poznan University of Technology
60-965 Poznan, Piotrowo 3 Street
tel.: +48 61 2244505, +48 61 2244502
E-mail: papers@ptnss.pl

Contents

Kalociński T., Rymaniak Ł., Fuć P. Powertrain technology transfer between F1 and the automotive industry based on Mercedes-Benz (CE-2018-101) 3

Kałużny J., Merkisz J., Kempa K., Gapiński B., Wróbewski E., Stepanenko A., Al-Karawi M. Friction reducing performance of carbon nanotubes covered pistons in internal combustion engines – engine test results (CE-2018-102) 14

Dziubak T. Operational properties of performance engine intake air cleaners (CE-2018-103) 25

Sidorowicz M., Pielecha I. The impact of injector placement on the dose preparation conditions in a gasoline direct injection system (CE-2018-104) 35

Gołębiowski W., Wolak A., Zając G. Definition of oil change intervals based on the analysis of selected physicochemical properties of used engine oils (CE-2018-105).......................................44

Pielecha I., Cieślik W., Szałek A. The use of electric drive in urban driving conditions using a hydrogen powered vehicle – Toyota Mirai (CE-2018-106) 51

Kowalski J. The influence of the fuel spray nozzle geometry on the exhaust gas composition from the marine 4-stroke diesel engine (CE-2018-107) 59

Czerwinski J., Comte P., Engelmann D., Bonsack P. Non-legislated emissions and PN of two passenger cars with gasoline-butanol blends (CE-2018-108)..64

Papers published in the
Combustion Engines
quarterly receive 13 points as stated
by the Notification of the Minister of Science
and Higher Education dated 31 December 2015.

Editor
Polish Scientific Society
of Combustion Engines
43-300 Bielsko-Biała, Sarni Stok 93 Street, Poland
tel.: +48 33 8130402, fax: +48 33 8125038
E-mail: sekretariat@ptnss.pl
WebSite: http://www.ptnss.pl

Subscriptions
Send subscription requests to the Publisher's address.
Cost of a single issue PLZ30 + VAT.

Preparation for print
ARS NOVA Publishing House
60-782 Poznań, ul. Grunwaldzka 17/10A

Circulation: 700 copies

Printing and binding
Zakład Poligraficzny Moś i Łuczak, sp. j., Poznań, ul. Piwna 1

The journal is registered
in the Polish technical
journals content database
– **BAZTECH** www.baztech.icm.edu.pl

The journal is listed
in the international database
IC Journal Master List
– **Index Copernicus** www.indexcopernicus.com

Declaration of the original version
The original version of the Combustion Engines journal
is the printed version.

Cover
I – Peugeot – e-HDI 1.5-litre 130-hp engine (*fot. uk.motor1.com*)
background (Drawing modern electronic circuit © Marisha – *Fotolia.com*)
IV – Peugeot – aftertreatment system (*fot. uk.motor1.com*)

Article citation info:
KALOCIŃSKI, T., RYMANIAK, Ł., FUĆ, P. Powertrain technology transfer between F1 and the Automotive industry based on Mercedes-Benz. *Combustion Engines*. 2018, **172**(1), 3-13. DOI: 10.19206/CE-2018-101

Tomasz KALOCIŃSKI
Łukasz RYMANIAK
Paweł FUĆ

CE-2018-101

Powertrain technology transfer between F1 and the automotive industry based on Mercedes-Benz

The paper presents evolution of the Formula One powertrain systems and its synergies with the Automotive industry. The article emphasises the influence of trends in the Automotive industry and general environmental awareness on the Formula One development. The technical regulations introduced by the FIA in 2006 made a first steps to align Formula One technology progress with course of automotive world. Improvements of the regulations in 2009 and 2014, gradually introduced hybrid systems to the Formula One and made its technology more relevant to the current production vehicles. On the other hand, paper also shows the examples of the automotive projects which utilised Formula One technology features and qualities. This review analyses technology transfer based on Mercedes-Benz and other companies dependent on Daimler AG.

Key words: *Formula One, hybrid technology, powertrain systems, technology transfer, automotive industry*

1. Introduction

Since the motor vehicle has been invented, a continuous race to be the best has started among automobile manufacturers and engineers. Motorsport seems to become one of the most popular ways to assess the construction of the vehicle and distinguish the best designs among different competitors. The first motor race took place in 1894 on the route between Paris and Rouen and highly stimulated various motor vehicles enthusiasts, engineers, manufacturers and entrepreneurs. The competition between automobile manufacturers and all different organisations involved into automobilism caused significant development in most of the automotive related fields of science. Within internal combustion engines (ICE) widely understood areas of physics, for instance: mechanics, thermodynamics or material technology have been hugely expanded. Internal combustion engines have always been the most important and the most complex part of powertrain systems. In the 20th century rapid development of this areas of the automotive industry brought increased diversification of engines and vehicles making them more specialised. Obviously since then, not all the purpose-made engines and vehicles were useful for motorsport or racing. Following that trend, racing engineering took its own path as well and since then have not always been relevant to the technology of "everyday" vehicles [4, 5].

Formula One (F1) is a great example of purpose-built engines and vehicles exclusively for motorsport. Major trend in development of F1 engines has been always their performance, specifically their maximum effective power within narrow band of speed range against the engine speed of the maximum power [6]. This established a specific direction of development for these engines as well as powertrain systems and differed substantially from common vehicle applications for many years. Fig. 1 presents Mercedes' engines specific power (maximum power related to 1000 cm^3 of engine displacement) and ICE thermal efficiency through last over 25 years.

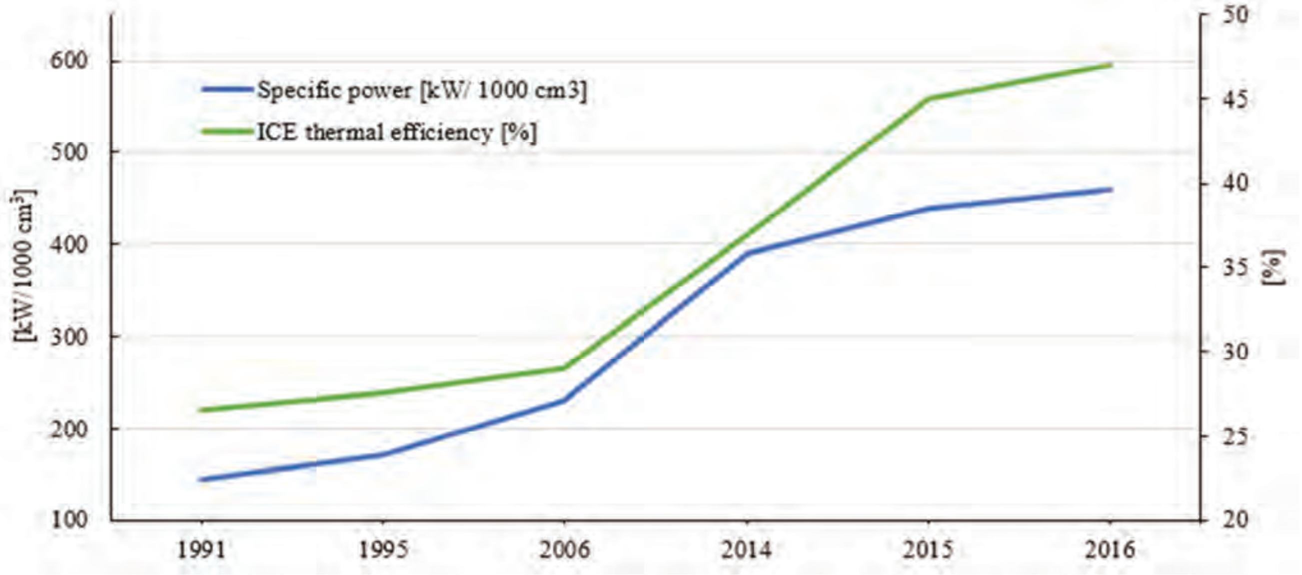

Fig. 1. Specific peak power and ICE thermal efficiency for Mercedes F1 engines between 1991-2016

In the 21st century, the situation within F1 and the automotive industry has begun to change. The governing body of the F1, the Federation Internationale de l'Automobile (FIA) started to introduce important changes to the F1 Technical Regulations. From 2006 cost reduction, increase in engine reliability and safety have been thoroughly considered. In 2009, then more widely in 2014, hybrid systems have been introduced to F1 as a response to the current trends in the automotive industry. Further reliability improvements, cost reductions and engine efficiency enhancements were also required. The steps undertaken in the first decade of the 21st century within the F1 regulations to improve technology alignment between F1 and the automotive industry have already brought satisfactory effects. Fig. 2 shows Mercedes' development timeline within over 10 last years, where F1 and Automotive industry transfer was included.

2. History of Mercedes-Benz in Formula One

From the very beginning of motorsport racing history, Mercedes-Benz has always been involved. This even includes the first motor race Paris-Rouen in 1894 where Emile Roger finished the race on in 14th position with his Benz vehicle. From 1923, Benz was widely involved in motor racing. In the 1930s, the legendary name "Silver Arrows" became famous because of Mercedes' cars domination [22, 23].

2.1. Mercedes-Benz in Formula One racing 1954-1955

Mercedes-Benz debuted in Formula One in 1954, four years after the F1 World Championship was established in 1950. The racing team managed by Alfred Neubauer had immediate success with driver Juan Manuel Fangio winning the Drivers' Championship in the first year. The success continued through entire next season with Fangio winning the Drivers' Championship again in 1955. In these seasons the name 'Silver Arrows' was already applied to the winning cars. This emphasized the team's connection to the famous Mercedes-Benz "Silver Arrow" cars dominating Grand Prix racing in Europe between 1934 and 1939 [22, 23].

The cars used in the 1954 and 1955 seasons were technologically advanced and named the Mercedes-Benz W 196 shown on Fig. 3. They were produced in two body versions: open-wheel (monoposto) and streamlined, closed-wheel. The body was made of magnesium-alloy panels built over a lightweight tubular spaceframe. Cars were also equipped with drum brakes and suspension with torsion bars.

Fig. 3. Mercedes-Benz W 196 „Silver Arrow" from 1995 [22]

According to the sport's governing body the Commission Sportive Internationale, new rules released in 1954 allowed either 2500 cm^3 naturally aspirated or 750 cm^3 would not be effective enough and a decision was made to create a new one. The newly designed engine was a straight eight, 2497 cm^3, naturally aspirated engine. It was mounted supercharged engines to be used in Formula One. Taking

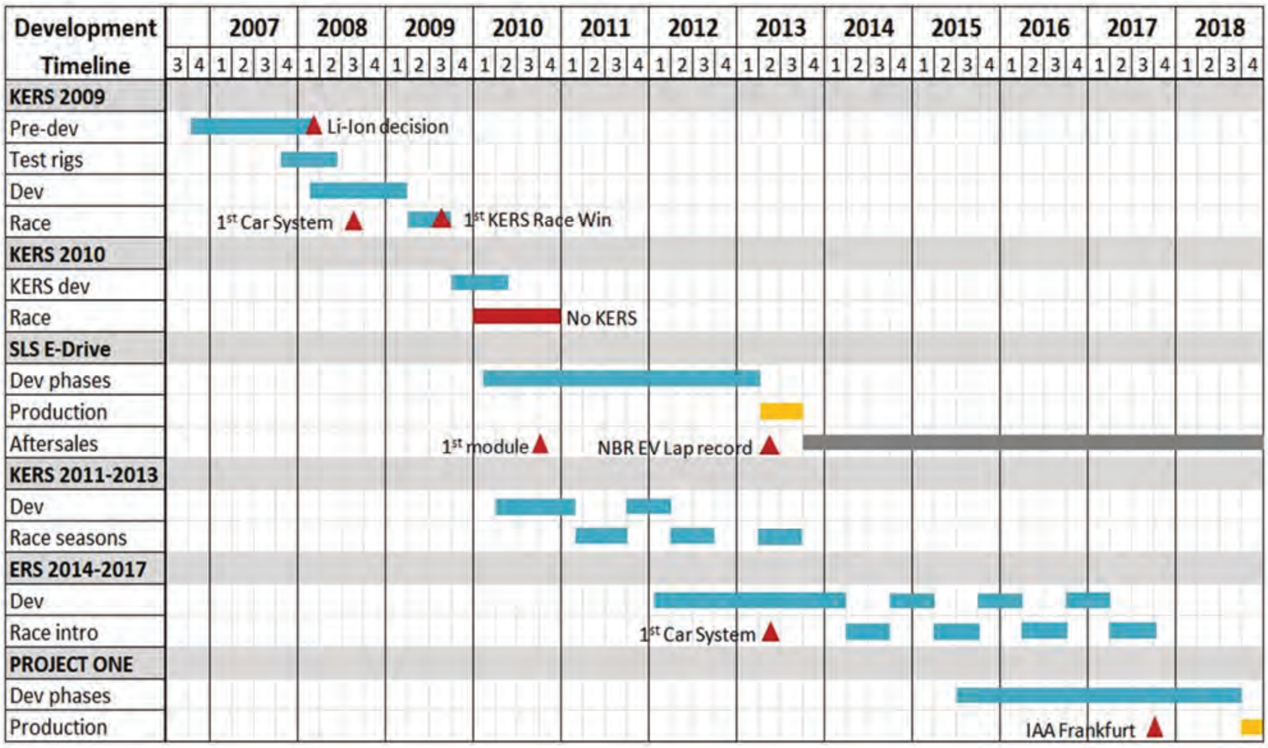

Fig. 2. Development timeline of hybrid systems and F1-related automotive projects in Mercedes-Benz

new rules into account Mercedes started extensive studies on their existing supercharged, 1500 cm^3, V8 engines from 1939. Calculations showed that a redesign of the old engine at an angle of 53 degree to the vertical axis to lower the center of the gravity and reduce the frontal area. The most important feature of this construction was a direct fuel injection developed together with Bosch which gave a significant advantage to the carbureted engines. The W 196 engine was also equipped with desmodromic valves which allowed the engine speed to exceed 8000 rpm and for bigger valves to be used without spring failure. The engine delivered 188 kW at 8260 rpm in 1954 and 213 kW at 8500 rpm in 1955 [22, 23].

The W196 was also used as the basis for the Mercedes-Benz to win the 1955 World Sportscar Championship, with the Mercedes-Benz 300 SLR. Mercedes dominated the 1955 Championship, until a catastrophic crash at Le Mans in June. Despite winning the Formula One World Championship in 1954 and 1955, as well as leading the World Sportscar Championship, Mercedes decided to withdraw from the all forms of a motorsport with immediate effect.

2.2. Mercedes-Benz as an engine supplier 1994-2005

Changes introduced to the Formula One technical regulations in 1989 completely ended the "turbo era" as new regulations allowed only 3500 cm^3, naturally aspirated engines, up to 12 cylinders. Since then turbocharging was forbidden completely in F1. On this occasion Ilmor, the company founded in 1983 by former Cosworth engineers following their successful period with IndyCar engines debuted in Formula One in 1991. They supplied the new LH10 engines for Leyton House, March and Tyrrell Formula One teams during 1991 and 1992 seasons. Ilmor LH10 was a V10, 3498 cm^3 engine generating 507 kW at 13 000 rpm in 1991 and 522 kW at 13 300 rpm in 1992 [12].

Mercedes-Benz planned to re-enter the Formula One in 1991 with Sauber as a partner, but then suspended the decision in 1992. Eventually during 1993 Mercedes-Benz took the observational role over Sauber Team and formed partnership with Ilmor. During that season "Concept by Mercedes-Benz" were written on the Sauber' engines produced by Ilmor.

Mercedes-Benz officially returned to Formula One as an engine supplier in 1994, entering the season as Sauber-Mercedes team. Mercedes provided updated and rebadged "Powered by Mercedes-Benz" version of Ilmor's engine from the previous season for Peter Sauber's Formula One team. The same year, Daimler-Benz AG (Mercedes parent company) acquired 25% of Ilmor's shares from Chevrolet consolidating their influence on the company.

For the 1995 season, significant changes to the Formula Ones technical rules were made. Due to the new regulations engines need to be naturally aspirated with displacement decreased to 3000 cm^3 and maximum of 12 cylinders. There was no limit on engine rpm. For this season Mercedes formed a partnership with McLaren and prepared the new FO 110 engine internally known as FH shown on Fig. 4. It was a 2997 cm^3, V10 with peak power of 515 kW at 15 600 rpm.

McLaren-Mercedes won the opening race of the 1997 season which was the first Mercedes-badged engine win. The following season brought both the Drivers' and Constructors' Championship with Mika Hakkinen at the wheel. Mika also went on to win the Drivers' Championship in 1999. DaimlerChrysler AG increased Mercedes-Benz' shares in Ilmor up to 55% in 2002 and renamed the outfit Mercedes-Ilmor. In 2005 DaimlerChrysler AG became the sole owner of Ilmor and renamed the company Mercedes-Benz High Performance Engines.

Fig. 4. Mercedes-Benz Fo 110, 3000 cm^3, V10 engine for 1995 F1 season

The new FIA technical regulations for 2005 limited the maximum number of engine cylinders to 10 and no more than 5 valves per one cylinder were allowed. For that season Mercedes came prepared with its last V10 engine marked FO 110R for McLaren [13].

3. First hybrid system in Mercedes – KERS (limited technology transfer)

Significant amendments were made for the 2006 season to the Formula One technical regulations. Explicit actions were also undertaken to reduce costs and increasing speeds on the Formula One cars.

3.1. Introduction of V8 engines

The most important changes were introduced to the engine specification. It had to be four stroke engine with displacement of no more than 2400 cm^3 which is 20% less than in previous regulations. The engine was arranged as a V8 with a 90 degree angle between the banks. Similarly to the previous rules, from the 2006, an engine remained naturally aspirated although for the first time an engine layout and cylinders number were given. Change from any V10 to V8 with restricted 90 degree bank angle resulted in use of single plain crankshaft which associated higher vibrations than in previous V10 engines.

Only 2 circular inlet and exhaust valves were permitted. Previous attempts to introduce 5 valves per cylinder have not been considered as increased valve area did not compensate negative impact on combustion chamber shape. Pneumatic Valve Return Systems (PVRS) and sodium cooled valves were still legal. Higher torsional vibration than in V10 on a timing system gear drive also required use of camshaft dampers. The maximum bore diameter was established as 98 mm which limits the stroke to be 39.79 mm at maximum bore. Spacing between the cylinders was set at 106.5 mm. The revolution limit remained unrestricted for 2006. This allowed Mercedes' development engine to obtain more than 20 000 rpm which with given stroke results with mean piston speed (S_p) over 26.5 m/s [1].

The use of variable inlet or exhaust geometry was not permitted and variable valve timing and variable valve lift were also banned. Indirect fuel injection was permitted only with one injector per corresponding inlet port with fuel pressure which does not exceed 10 MPa. Multiple injectors were no longer legal although increased fuel pressure allowed better atomization. Similarly, in terms of ignition, only one spark plug and spark coil per cylinder was allowed. The minimum weight of the engine was set to 95 kg.

The new rules placed a lot of emphasis on the reduction of engine development costs, specifically limiting the materials which could be used within an engine. Crankcases, cylinder heads and pistons could be manufactured only from aluminum alloys. Crankshaft and camshafts could be manufactured only form iron based alloys. Nitriding and Diamond Like Carbon (DLC) treatments were still permitted. Since 2006, no materials with density higher than 19 000 kg/m^3 were allowed to be assemble with the crankshaft which disqualified pure tungsten although tungsten alloys were still legal. Magnesium based alloys, Intermetallic materials and Metal Matrix Composites (MMC's) were forbidden. All materials containing more than 5% by weight of Beryllium, Iridium and Rhenium were also banned [10, 14].

Further cost reductions froze the engine specification and put more pressure on increasing of reliability. Engine revolution limit at 19 000 rpm was set from 2007. Since 2008 engines must last for at least four race weekends [15, 16]. Reduction of engine displacement decreased the maximum power output of about 20% in comparison to the previous engine specification, but also reduced fuel consumption up to 15%. Teams which could not afford to obtain new engines were allowed to use previous, 2005 season ones with adequate revolution limitations [9].

For 2006 season Mercedes-Benz presented a very well prepared, powerful and reliable FO 108 S engine presented on Fig. 3. It generated over 555 kW of peak power at 19 000 rpm with break mean effective pressure (BMEP) over 14.6 bar [18]. In 2007 FO108T, an updated version of the 2006 season engine powered Lewis Hamilton and Fernando Alonso driving for the Vodafone McLaren-Mercedes team to eight pole positions and eight race wins. This engine also achieved a great result of zero race weekend failures over 32 races that season. In 2008 season, Lewis Hamilton won his first Drivers' Championship with Mercedes' engine powered car.

Fig. 5. Mercedes-Benz FO 108 S, 2400 cm^3, V8 for 2006 F1 season

3.2. KERS introduced to the V8 engines

A continuation of the FIA's cost reduction policy from 2006 aligned with improvements in engine reliability was expanded in the next few seasons. In 2009, the FIA allowed the use of KERS (Kinetic Energy Recovery System) in Formula One and restricted engine revolutions even further – to 18 000 rpm. An enhancements in engine reliability was forced by the introduction of the requirement that only 8 engines could be used by a driver over a single season. KERS allows energy to be harvested during braking, stored and then deployed by the driver's decision at any point during the race, e.g. during overtaking. That explains why in some circumstances KERS might be call a regenerative braking. According to the 2009 the FIA regulations, KERS in Formula One could release no more than 400 kJ of recovered kinetic energy in any one lap. Rules also allow the transfer of no more than 60 kW of energy in and out of the KERS. Mercedes-Benz started their work on KERS in 2007, shortly after the first season with new, V8 specification engine was finished. No restrictions to the KERS technology was applied therefore different solutions were considered. Mercedes-Benz prepared three systems: flywheel, lithium-ion (Li-Ion) battery and ultracapacitor [17, 18].

Electrical KERS with motor-generator and battery was chosen (Fig.6). Battery with Li-Ion cells were developed as it has the highest energy density by mass in comparison to other electrochemical cells. In this solution, motor-generator was mechanically coupled with ICE crankshaft by fix speed ratio creating integrated hybrid system [2, 3]. The first fully operational test module was introduced in only 8 months. Tests of the new system started at the beginning of 2008, only 14 months after the pre-development stage.

Mercedes' first F1 hybrid engine unit was the FO 108W which was an improved 2008 season engine with electric motor-generator, lithium-ion battery and power electronics, internally known as FW. It generated over 555 kW of power at 18 000 rpm with an oil cooled battery pack and total

Fig. 6. First track test KERS battery and power electronics from 2008

KERS mass of 25.3 kg (Fig. 7). Efforts of Mercedes' engineers resulted in the first win of a KERS powered car-Vodafone McLaren-Mercedes during the 2009 Hungarian Grand Prix.

Fig. 7. Mercedes-Benz FO 108 W, 2400 cm^3, V8 with KERS for 2009 F1 season [25]

Later in 2009 Mercedes-Benz bought a controlling stake (75.1%) of the championship winning Brawn GP, renamed it Mercedes GP one year later and signed a sponsorship agreement with Petronas. In 2010 Mercedes GP Petronas Formula One Team drove with their „Silver Arrows" again after 55 years. KERS was still legal this year however all Formula One teams agreed not to use it. It returned to Formula One in 2011 at which point Mercedes-Benz High Performance Engines factory was renamed Mercedes AMG High Performance Powertrains. KERS was used in that form in F1 until 2013.

4. Advanced hybrid systems – ERS (improved technology transfer)

Technological changes introduced by the FIA in 2006 and then in 2009 explored new opportunities within powertrain technology in Formula One. Engines became more efficient, reliable and cheaper in development. Utilising KERS as a first hybrid technology also emphasised its relevance to current trends in the automotive industry and paved a new way in F1 powertrains. In 2010 the FIA decided to take the next step and expand technology alignment between F1 and automotive industry even further.

4.1. Changes in Technical Regulations

From 2010 the FIA started to work on new technical regulations. They wanted to attract more sponsors and vehicle manufacturers to invest in F1 by offering them a proving ground for technology development. New technical regulations which were subject to apply from 2013 included more factors affecting current automotive powertrain systems. Significant increase of thermal efficiency, downsizing and advanced hybridisation were considered. General environmental aspects, such as CO_2 reduction were also taken into account together with further enhancement of reliability. The first draft of the new technical regulations introduced a 1600 cm^3, four cylinder turbocharged engines with fuel flow rate restrictions and energy recovery systems. The provisional regulations came across major protests, which influenced the rules and postponed its introduction.

Finally, the new rules became valid from 2014 and launched a new turbocharged V6, hybrid power unit formula with a displacement of 1600 cm^3. It was a serious turn in Formula One history. The technical term- engine, was no longer applicable and changed in favour of advanced hybrid power unit. From then, power output was calculated as a combined value of the mechanical energy from the internal combustion engine based on its thermal efficiency and the electrical energy from energy recovery system (ERS). Since the new rules reduced the internal combustion engine displacement by a third in comparison to the V8, the maximum power output decreased significantly. I addition to that new requirements assumed use of direct fuel injection and maximum fuel flow rate of 100 kg/h. Following these restrictions, a decision was made to establish the maximum power of the electric motor assisting ICE (MGUK) at level of 120 kW, which is double the value of its predecessor KERS [19].

In term of material that could be used for PU, the FIA applied further restrictions to the previous rules from 2006. Since 2014, no tungsten alloys are permitted to be used at all, as well as ceramics and ceramics matrix composites. All alloys are restricted to maximum 0.25% content of beryllium, excluding copper alloys which can contain 2.75% of berylium. Copper-beryllium alloys were widely used for e.g. valve seats. Minimum weight of the PU must be a minimum of 145 kg which is 50 kg more that for previous V8 engines and allow additional weight for e.g. electric machines.

From 2014 onwards, system of tokens was introduced as a second factor besides finance to maintain costs reduction in powertrain development among different manufacturers. Power Units are broken down into 66 tokens with „weight" from 1 to 3 assigned to different power unit components. Development of certain component uses its tokens therefore manufacturers have to chose what to develop in subsequent years to keep the sustainable PU development.

4.2. Power Unit (PU) components and its operational modes

The Power Unit (PU) is a complex combination of internal combustion engine (ICE) and advanced energy recovery system (ERS). From the very beginning it was designed and developed as a sophisticated hybrid machine, significantly different to the previous 2400 cm^3, V8 engine with KERS. Having said that in order distinguish the most important parts the Power Unit is divided into 6 subsystems.

Internal combustion engine (ICE)

As per Formula One Technical Regulations introduced in 2014, internal combustion engine as a part of power unit must be a V6, turbocharged engine with 90 degrees bank angle and displacement of 1600 cm^3 at maximum.

Two inlet and two exhaust valves are required with no variable valve lift profile or timing employed. Exhaust gases may exit the cylinders only from the outside of the engine, no from the inside of the "V" arrangement. Valves stem size cannot be smaller than 5 mm.

Engine revolutions are limited to 15 000 rpm therefore lower than the latest amendment for V8 engines in 2013 (18 000 rpm). Allowed maximum cylinder bore is 80 mm (18% less than in 2400 cm^3, V8) which implies 53.05 mm of stroke. Having said that, the mean piston speed (S_p) in new V6 engine increased, and again exceeded 26.5 m/s as it was in the V8 engine from 2006 when reaching 20 000 rpm. Stroke-bore ratio also increased from 0.4 in V8 engines to approximately 0.6–0.7 in new power units. There is no fixed spacing between cylinders required as it was for V8 although the crankshaft may have only 3 connecting rods bearing journals.

The new regulations also introduced more complex fuel restrictions in comparison to the previous V8 rules introduced in 2010. Global maximum fuel flow allowed is 100 kg/h (about 35–40% less than for V8) although up to 10 500 rpm maximum fuel flow is restricted by following formula: $Q_m = 0.009\ n\ [rpm] + 5.5\ [kg/h]$. The amount of fuel that can be used during one race is also restricted to a maximum of 100 kg. Fuel needs to be delivered to the cylinder by a direct injection system. The permitted pressure of fuel that can be supplied to the injectors increased to 50 MPa. In previous V8 engines, fuel pressure only up to 10 MPa was allowed which made direct injection simply unfeasible to use. The fuel flow rate with V8 engines was usually reaching over 150 kg/h. One fuel injector per cylinder is allowed as well as one single ignition coil and one single spark plug [8]. Since restrictions about total amount of fuel that can be used in one race is not a new requirement following fuel rules from 2010, the fixed maximal fuel flow restricted is absolutely new. As a result of that, fundamentally new approach to the air excess ratio (λ) has been applied [1]. In new V6 engines air excess ratio might exceed 1.2 whereas in previous V8 was usually below 0.8 for the regions of maximum power. Having said that running less rich in case of saving fuel in V6 engines is not that feasible as it was in V8 engines without power loses [7].

Turbocharger (TC)

In 2014 turbocharging became allowed in Formula One again first time since 1988 [11]. According to the new rules compressing of air needs to be utilised with a single stage compressor joined to the single stage turbine. Both shafts need to rotate about common axis and with the same angular velocity. Charging pressure is not restricted however variable turbine geometry (VGT) is not permitted. The device responsible for recovering energy from heat, the MGU-H, can be coupled directly to the turbine. Rotational speed of the turbine shaft is restricted to 125 000 rpm.

Motor Generator Unit-Kinetic (MGU-K)

The MGU-K is an electric machine which can operate as a motor or alternatively as a generator depending on requirement. It is the sole successor of the KERS motor-generator introduced for the first time in 2009. Restrictions to the maximum power of the MGU-K rise to 120 kW in comparison to KERS's 60 kW. The maximum torque generated by the MGU-K cannot exceed 200 Nm at any point.

Only one single MGU-K is permitted to recover energy from the vehicle. It needs to be mechanically and permanently linked to the ICE crankshaft before the main clutch. A fixed speed ratio between the MGU-K and the ICE is required and might be clutched. The rotational speed of the MGU-K is restricted to 50 000 rpm.

The MGU-K is the second device after ICE, allowed to propel the vehicle. It acts as an electric motor and assists the ICE during acceleration using energy from energy store (ES) or directly from corresponding device (MGU-H), recovering energy from exhaust gases. During braking, the MGU-K switches to generator mode and assists brake, harvesting part of the kinetic energy that otherwise would be dissipated as heat [7, 19].

Motor Generator Unit-Heat (MGU-H)

Similarly to the kinetic energy recovery unit, MGU-H is a motor-generator electrical device. It needs to be mechanically connected to the turbine of the pressure charging system. The mechanical connection might be clutched although it must be a fixed speed ratio to the turbine shaft. The maximal allowed rotational speed cannot exceed 125 000 rpm. Unlike to the MGU-K, power and torque transferred from and to the MGU-H is not restricted.

Acting as a generator, MGU-H harvests the excessive heat energy from the exhaust gases flowing through the turbine and transfers it to the energy store (ES) for later use or directly to the MGH-K to propel the car. Another important function of the MGU-H is to control compressor wheel speed in some operational ranges of the ICE so the air delivered into the combustion chamber matches fuel requirements with given air fuel ratio. The generator mode of the MGU-H uses energy from the ES and accelerates the turbine shaft to reduce turbocharger response delay when exhaust gases flow is low.

Energy Store (ES)

Energy storage of the Energy Recovering System (ERS) is an electric battery which can never exceed a level of 1000 V. It needs to be designed as a single component and be wholly locate within the survival cell. The weight of the ES needs to be maintained between 20 kg and 25 kg for an entire assembly. The allowable peak difference between maximum and minimum state of charge (SOC) of the ES at any time when vehicle is on the track cannot exceed 4 MJ.

Control Electronics (CE)

The main task of control electronics is to manage energy transfer between the MGU-K, MGU-H and ES while working together with the ICE. Depending on current powertrain mode, the control electronics, driven by sophisticated software, executes predefined algorithms to fulfil the driver's demand. This includes charging and discharging of teh ES, as well as changing current form among the certain components of ERS.

Operation of Power Unit (PU)

The Power Unit (PU) consists of a sophisticated ICE and 5 advanced components of ERS. Operation of this complex assembly is based on diverse energy transfer modes among the components of the PU and depends on the chosen strategy (Fig. 8). The F1 vehicle with substantial

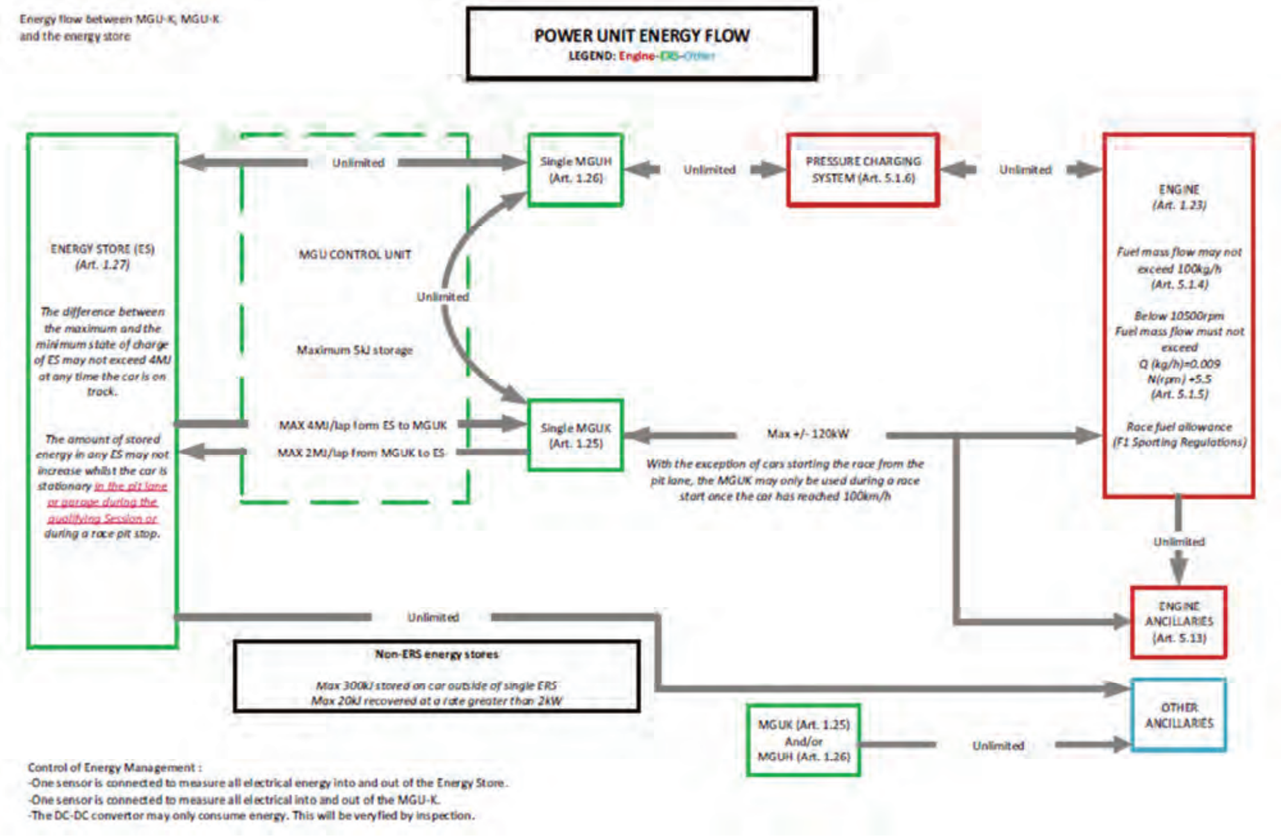

Fig. 8. Energy flow within Power Unit [20]

speed on a straight line is primarily propelled by ICE using fuel reserves, however additional energy recovered by the MGU-H (generator mode) from excessive amount of exhaust gases might be used by the MGU-K to assist the ICE. During the same event, energy harvested by the MGU-H can be also transferred to the ES for later use. Energy transferred from the MGU-H to the ES and backwards in unrestricted. The same rule applies for energy transferred from the MGU-H to the MGU-K and backwards. When a braking event occurs, the MGU-K works as a generator and assists brake, converting part of the thermal energy from braking into electric energy which can be stored in ES. The maximum amount of energy which can be transferred from the MGU-K to the ES is 2 MJ per lap. Under acceleration after the braking, the MGU-H switches to electric motor mode and propels the turbine shaft to reduce "turbo lag" effect. Additional energy from the ES not exceeding 4 MJ can be deployed to the MGU-K during the same event to support the ICE. It is also worth noting that with the exception of starting from the pit lane, the MGU-K can be used during the race only after the vehicle exceeded 100 km/h. The F1 vehicle can be also propelled by the ICE only [7, 19].

4.3. Mercedes's Power Units

Mercedes AMG High Performance Powertrains, as a part of Mercedes-Benz Formula One team, started its work on a new power unit in 2012 when the new rules regarding 1600 cm^3, V6 Power Units became firm. The biggest focus was put on the 4 teams dealing with crucial features of the new Power Unit: combustion simulation, turbocharger design, hybrid system and software development. Absence of supercharging in F1 for the last 25 years at that time led the Mercedes engine development team to search for expertise in parent Daimler company. This resulted with good cooperation with the Mercedes-Benz Trucks division as well as MTU gas turbine group. First development engine, with internal name GB, weighted over 250 kg and it was not possible to even fit it into a F1 vehicle. It was not so advanced and sophisticated as the latest ones. A separate turbocharger and MGU-H assembly was also not developed yet at this stage. Nevertheless, this module allowed the engineers to understand the mechanisms of direct injection and charge motion in the cylinder together with gas exchange and combustion. Results of this work were transferred to the single cylinder development engines which allowed goals to be set for the final module for the 2014 season (Fig. 9).

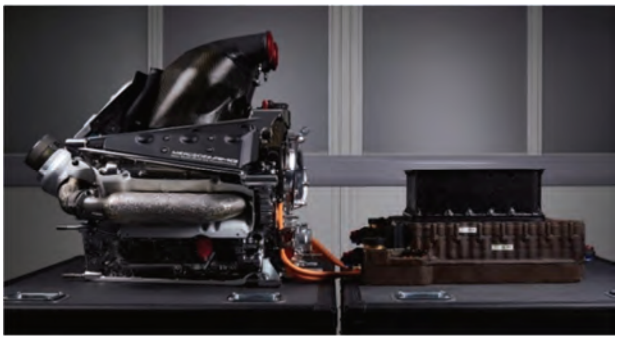

Fig. 9. Mercedes-Benz PU 106 A Hybrid, 1600 cm^3, V6 power unit for 2014 F1 season [25]

In 2014, PU 106 A Hybrid, internally known as GD, complied with the new F1 Technical Regulations and was introduced into the Mercedes F1 W05 Hybrid vehicle. It was the first Power Unit delivered by Mercedes AMG High Performance Powertrains. It led Lewis Hamilton to win his second Drivers Championship and brought Mercedes the 2014 Constructor Championship. The engine generated over 630 kW at 15 000 rpm at the end of the 2014 season and presented over 37% of thermal efficiency as a sole ICE.

The 2015 season brought slight changes to the engines specification and sporting rules. The new PU 106 B Hybrid (GE) engine, introduced for this season, presented similar architecture to its previous version although only 5% of parts were carried over from the last season without modifications. Variable length intake became permitted which was related closely to improvements in engine efficiency but also implicated some packaging challenges with larger plenums. Reliability of the engines had to increase significantly since 4 engines per season per driver were introduced in place of 5 engines in previous season. This implies over 5000 km of track time. At the end of the 2015 season PU 106 B Hybrid performed 710 kW at 15 000 rpm and over 45% of thermal efficiency. Lewis Hamilton won his third Drivers Championship and Mercedes F1 became a Constructors' Champion again [20].

In 2016, PU 106 C Hybrid (Fig. 10) raised the bar even higher establishing the thermal efficiency of the ICE over 47% and peak power at 750 kW (1000 KM) at 15 000 rpm. Moreover, overall efficiency of the PU which is ICE and ERS in 2016 exceeded 50%. This year, technical rules also included changes in tailpipe design. Separate pipes were permitted to be use from wastegate and turbocharges outlets. The change in regulations was caused by fans' complains that F1 Power Units are too quiet and suppose to make them about 20–25% lauder. Nico Rosberg won the Drivers' Championship this year and Mercedes celebrated the third Constructor Championship [8, 21].

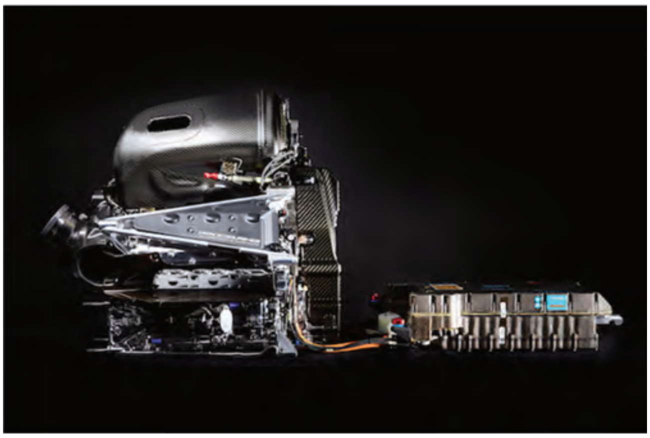

Fig. 10. Mercedes-Benz PU 106 C Hybrid, 1600 cm^3, V6 power unit for 2015 F1 season [25]

5. Technology transfer – examples

Development of KERS started in Mercedes AMG High Performance Engines in 2007. After first successful season in 2009, KERS was not used for any of F1 teams in 2010, came back in 2011 and it was used for the last time in 2013. Broad expertise in high performance hybrid systems and gap in use of KERS in 2010 was utilised by Mercedes-Benz to develop technologies which can be transferred to the automotive industry.

5.1. Mercedes-Benz SLS AMG Electric Drive

Mercedes-Benz SLS AMG Coupe Electric Drive was technically based on the Mercedes-Benz SLS AMG released in 2010 as a successor to the legendary Mercedes-Benz 300 SL "Gullwing" from 1954. Mercedes-Benz SLS AMG Coupe Electric Drive was developed by Mercedes-AMG division as its first vehicle designed independently from Mercedes-Benz. The electric powertrain and especially the battery was fundamentally based on knowledge brought from F1 KERS and developed at Mercedes AMG High Performance Engines, from 2011 known as Mercedes AMG High Performance Powertrains. The first prototype vehicle, called the Mercedes-Benz SLS AMG E-CELL, was shown in 2011 in the North American International Auto Show (Fig. 11). The production version was presented in 2012 at the Paris Motor Show and introduced to production in 2013.

Fig. 11. Mercedes-Benz SLS AMG Electric Drive- vehicle overview [24]

The powertrain of the Mercedes-Benz SLS AMG Coupe Electric Drive was based on four compact permanent-magnet synchronous electric motors. Each of them weighted 45 kg and were able to achieve 13 000 rpm. The motors could be driven selectively enabling precise torque distribution. All four motors together generated 552 kW of power and 1000 Nm of torque. The battery of the vehicle was a liquid-cooled, 400 V module with energy content of 60 kWh. It weighted 548 kg and contained 12 sections of 72 lithium-ion cells. Those 864 cells were arranged in a parallel circuit of independent modules which allowed efficient space use and enabled battery service. Similarly, as in KERS from F1, the battery can be charged by energy recuperated during vehicle deceleration. The battery module was closed in high-strength aluminium casing within the carbon-fiber reinforced plastic (CFRP) zero intrusion monocoque. This protects the battery from deformation or damage in case of crash event. In addition, battery of the vehicle could be charged at home by 22 kW device called „wall box" and supplied with the car. Charging lasts about 20 hours.

High performance power electronics covert direct current from the battery module in 3-phase alternating current for 4 synchronous electric motors and controls the energy flow within the system under variable operating conditions. The powertrain is also equipped with three low temperature, the cooling circuits, two for electric motors and separate one for the battery module. Under extremally low ambient temperature cooling systems can switch into warming mode to bring the system to the operational conditions.

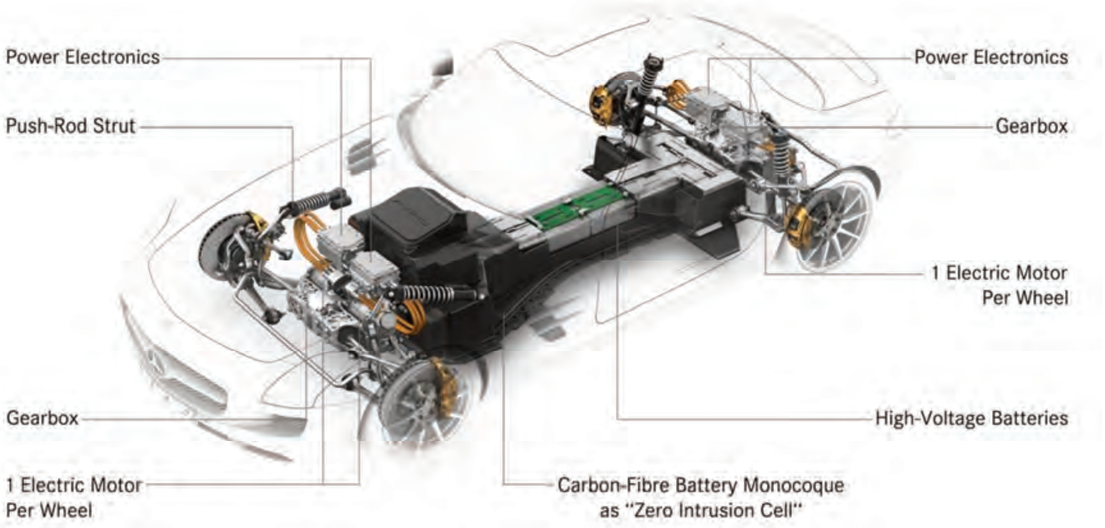

Fig. 12. Mercedes-Benz SLS AMG Electric Drive – powertrain overview [24]

The performance of Mercedes-Benz SLS AMG Coupe Electric Drive included 250 km of range (based on NEDC combined) and acceleration within 3.9 s from 0–100 km/h. The maximum vehicle speed was electronically restricted to 250 km/h. The vehicle also established a lap record of the Nurburgring for electric vehicle (EV) at 7.56 min. The most powerful combustion version of this model, the Mercedes-Benz SLS AMG Coupe Black Series with 464 kW of peak power at 7400 rpm and torque of 635 Nm at 5500 rpm, performed 0–100 km/h in 3.6 s. That comparison shows respectable performance of electric model and makes it the most powerful and the fastest electric production vehicle. From the 2010 season onwards, the combustion version of the Mercedes-Benz SLS AMG also worked as the safety car during F1 races. Later in 2012 replaced by its successor Mercedes-AMG SLS GT [24].

5.2. Mercedes-AMG Project ONE

In 2012, Mercedes AMG High Performance Powertrains had already started its work on the new F1 Power Unit defined by FIA Formula One Technical Regulations. This technical specification became applicable from the 2014 season onwards and brought significant changes to F1 powertrains.

The Power Unit introduced in 2014 by Mercedes became an enormous success and started a three years of Mercedes domination within F1. Mercedes AMG Petronas Formula 1 team collected all Drivers Championship and Constructors Championship in three consecutive years: 2014, 2015 and 2016. Following that great achievement Mercedes-AMG and Mercedes AMG High Performance Powertrains are joining their efforts again to deliver the F1 technology based hypercar. This time Mercedes wants to go a step further and deliver, for the first time in the history of motoring, a production vehicle with a F1 powertrain. The Mercedes-AMG Project ONE officially confirmed in 2016 at the Paris Motor Show.

The main idea of this vehicle is an ultimate hypercar with unaltered F1 hybrid technology with road approval. According to officially released information, the high performance F1 hybrid power unit is going to be accompanied with the purely electric and selective front axle. Overall peak power of the powertrain is going to exceed 735 kW (1000 hp). The general overview of the vehicle's powertrain is presented on the Fig. 13.

Mercedes-AMG Project ONE is going to be revealed on September 2017 at the International Motor Show in Frankfurt celebrating Mercedes-AMG's 50th anniversary.

6. Conclusions

Despite Mercedes has started its F1 experience in 1950s, the successful period did not last long and resulted with withdrawal from the motorsport. The Mercedes returned to the F1 after 40 years in 1990s. Initially, as an engine supplier, and later in 2010, as a constructor.

In 2006, FIA introduced first major amendments to the F1 Technical Regulations which included serious modifications to the powertrain system. Reduce of development costs of the engine and increase in its reliability started to play an important role in F1. An engine displacement has been reduced and its arrangement, together with the cylinder number were given for the first time.

From 2009, new regulations allowed F1 teams to use kinetic energy recovery systems. That created the first hybrid systems within F1 and shown the new directions of development.

The 2014 brought the most revolutionary changes in F1 history. The FIA made further steps into increasing of powertrain reliability and reduction of its development costs. General environmental considerations including reduction of CO_2 were also included and resulted with the

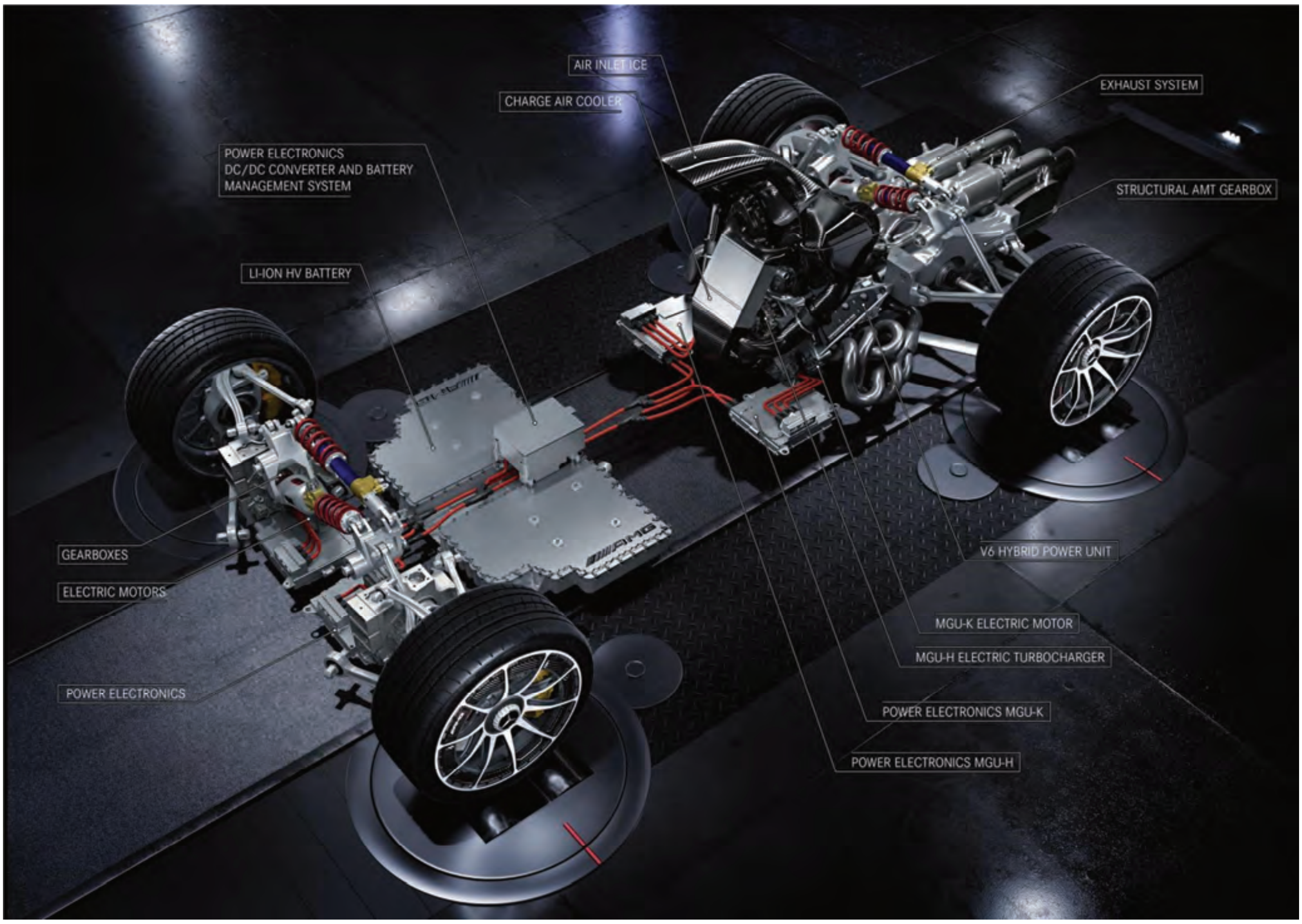

Fig. 13. Mercedes-AMG Project ONE – powertrain overview [24]

fuel restrictions. The new amendments included also higher relevance of F1 powertrain technology to the automotive world. The F1 high speed naturally aspirated engines ware changed into advanced, turbocharged hybrid power units.

The improvements introduced in 2014 to the F1 regulations returned significant achievements in several areas of powertrains performance. The fuel consumption and CO_2 emission has been reduced due to the restrictions. The thermal efficiency of the ICE increased from about 27% in 2005 to about 47% in 2016. The durability of the PU has also been enhanced from about 2500 km in 2013 to over 5000 km in 2015.The absence of KERS in F1 during 2010 motivated Mercedes to work on the F1 technology based vehicle and created the Mercedes-Benz SLS AMG Electric Drive. The expertise in the F1 hybrid systems allowed to develop electric vehicle which utilized F1 experience with Li-Ion batteries.

In 2015, Mercedes decided to make the next step and started its work on Mercedes-AMG Project ONE – vehicle which utilise entire F1 hybrid Power Unit.

Presented examples of technology transfer show that the F1 and the Automotive industry highly influence each other and provide satisfactory results. This allowed to formulate following observations:

1. The fuel restrictions to the F1 Power Units brought significant enhancement in thermal efficiency of the ICE which could be transferred to the Automotive industry.
2. The development of high performance hybrid systems might be shortly implemented in production vehicles.
3. The future FIA regulations within F1 might impose further reliability increase, reduction in fuel consumption and reduction or restrictions in exhaust gases emission.

Nomenclature

BMEP	brake mean effective pressure
CE	control electronics
CFRP	carbon-fiber reinforced prastic
DLC	diamond like carbon
ERS	energy recovery system
ES	energy store
EV	electric vehicle
FIA	Federation Internationale de l'Automobile
F1	Formula One
ICE	internal combustion engine
KERS	kinetic energy recovery system
Li-Ion	lithium-ion
MGU-H	motor generator unit-heat
MGU-K	motor generator unit-kinetic
MMC	metal matrix composites
NEDC	New European Driving Cycle

PU	power unit
PVRS	pneumatic valve retuen system
TC	turbocharger
VGT	variable geometry turbocharger

Bibliography

[1] HEYWOOD, J.B. Internal Combustion Engine Fundamentals. *McGraw-Hill, Inc.* 1988.
[2] MERKISZ, J., PIELECHA, I. Układy mechaniczne pojazdów hybrydowych. *Wydawnictwo Politechniki Poznańskiej*. Poznań 2015.
[3] MERKISZ, J., PIELECHA, I. Układy elektryczne pojazdów hybrydowych. *Wydawnictwo Politechniki Poznańskiej*. Poznań 2015.
[4] MERKISZ, J., PIELECHA, I., MARKOWSKI, J. Wskaźniki pracy silników pojazdów wyczynowych. *Combustion Engines*. 2007, **4**(131), 3-18.
[5] RYCHTER, W. Dzieje samochodu. *Wydawnictwo Komunikacji i Łączności*. Warszawa 1979.
[6] STĘPIEŃ, Z. A new generation of F1 engines – hybrid power units. *Combustion Engines*. 2016, **167**(4), 22-37.
[7] The F1s new power generation. *F1 race technology*. 2014
[8] The half way to impossible. *Race Car Engineering*. 2016.
[9] The last of the V8s. *Race Car Engineering*. 2013.
[10] The V8 F1 Engine. *Formula One Technology*. 2006, 38-43.
[11] 1988 Formula One Technical Regulations – Federation Internationale de l'Automobile.
[12] 1994 Formula One Technical Regulations – Federation Internationale de l'Automobile
[13] 2005 Formula One Technical Regulations – Federation Internationale de l'Automobile
[14] 2006 Formula One Technical Regulations – Federation Internationale de l'Automobile
[15] 2007 Formula One Technical Regulations – Federation Internationale de l'Automobile
[16] 2008 Formula One Technical Regulations – Federation Internationale de l'Automobile
[17] 2009 Formula One Technical Regulations – Federation Internationale de l'Automobile
[18] 2013 Formula One Technical Regulations – Federation Internationale de l'Automobile
[19] 2014 Formula One Technical Regulations – Federation Internationale de l'Automobile
[20] 2015 Formula One Technical Regulations – Federation Internationale de l'Automobile
[21] 2016 Formula One Technical Regulations – Federation Internationale de l'Automobile
[22] www.mercedes-benz.com
[23] www.mercedesamgf1.com
[24] www.mercedes-amg.com
[25] www.mercedes-amg-hpp.com

Tomasz Kalociński, MEng. – Mechanical Engineer at Mercedes AMG High Performance Powertrains in Brixworth, UK.

e-mail: *Tomasz.Kalocinski@mercedes-amg-hpp.com*

Paweł Fuć, DSc., DEng. – Faculty of Machines and Transport at Poznan University of Technology.

e-mail: *Pawel.Fuc@put.poznan.pl*

Łukasz Rymaniak, DEng. – Faculty of Machines and Transport at Poznan University of Technology.

e-mail: *Lukasz.Rymaniak@put.poznan.pl*

Article citation info:
KAŁUŻNY, J., MERKISZ, J., KEMPA, K. et al. Friction reducing performance of carbon nanotubes covered pistons in internal combustion engines – engine test results. *Combustion Engines*. 2018, **172**(1), 14-24. DOI: 10.19206/CE-2018-102

Jarosław KAŁUŻNY
Jerzy MERKISZ
Krzysztof KEMPA
Bartosz GAPIŃSKI
Emil WRÓBEWSKI
Aleksander STEPANENKO
Mohanad AL-KARAWI

CE-2018-102

Friction reducing performance of carbon nanotubes covered pistons in internal combustion engines – engine test results

This article discusses the posibility of reducing friction losses in internal combustion engines by using carbon nanotubes, pointing out the large potential of this application. Experimental pistons were made of standard aluminum alloy and coated with a layer of nanotube deposits by spraying them with an aqueous solution containing the binder. The proposed technology of applying layers of nanotubes can be adopted in industrial-scale production. Engine tests were carried out showing a significant reduction of the engine motoring torque, up to 16% for the experimental pistons, thus confirming the favorable tribological properties of nanotubes observed in tribological research and reported by many authors. Supplementary tests were carried out: SEM, EDS, coordinate measuring technique, and x-ray tomography. An alternative technology for hierarchical nanotube multilayer coatings electro-deposition was proposed.

Key words: c*ombustion engines, piston, carbon nanotubes, friction*

1. Introduction

1.1. Significance of friction losses in internal combustion engine and the ways to reduce it

There are currently about 1 billion cars in use worldwide, the vast majority of them are powered with piston engines. Tens of millions of new cars are manufactured around the globe every year, also among these cars a great majority is still powered by piston engines. A popular opinion in recent years is the mistaken belief that car emissions are a major source of environmental pollution and a major cause of the greenhouse effect, and that the solution to this is to replace the internal combustion engine with an electric one. In fact, the use of electric cars makes sense only in the centers of large cities where emission problems are not successfully controlled.

Well-to-wheel analysis has shown that even if there were a breakthrough in the construction of the battery in the near future, wide use of electric motors in car powertrains would have a negative net carbon dioxide emissions balance [6, 39]. The solution to this issue would be a radical increase in the share of renewable energy sources in global electricity production, but this task would take decades to achieve.

Contemporary conditions mean that efforts to make the internal combustion engines more environmentally friendly and powerful are the most important. The overall efficiency of the modern automobile engine reaches 45%, but only for medium speed and high load conditions. In these operating conditions the friction loss contribution in the total energy balance of the engine is small, which is expressed by the mechanical efficiency exceeding 90%. Unfortunately, in normal operation the car engine works most of the time at small and very small load conditions, and then the friction loss plays a dominant role in the overall energy balance. The most frequent operating condition of the internal combustion engine is one where the actual power is very small in comparison to the engine's maximum power, but still all the engine components are kept in motion, and thus produce a frictional force similar to that produced under high load. Mechanical efficiency of the engine in the NEDC test and under normal operation of the vehicle is significantly less than 50%, thus becoming the main factor determining the low overall efficiency of the engine. This is a well-known problem where direct methods of approach, based on reduction of friction losses, have already been widely exploited [18, 41] leaving very little scope for further improvement.

Another, indirect and more effective way to reduce friction losses is to replace a large engine with a smaller one, usually with lower number of cylinders, and to compensate the power deficit through the application of turbocharging. This concept is called "downsizing" [17] and has been successfully implemented for most car engines produced in Europe in the last 10 years. The higher the degree of downsizing, the greater the benefits in terms of improving the efficiency and reducing fuel consumption. The barrier is the increasing mechanical and thermal load of the engine structure, which can be controlled by the use of new materials with properties superior to the conventional materials used to date [17].

In the opinion of the authors, the next step in the process of improving the design of internal combustion engines can be the application of nanomaterials. Carbon nanotubes (CNT) are a relatively recently discovered and intensively studied material [4, 11]; among their unique features extremely beneficial tribological properties are often mentioned [8, 22].

1.2. Results of atomic scale carbon nanotube research

The authors expect that the use of CNTs in the design of internal combustion engines may reduce friction loss and fuel consumption. Furthermore, CNTs can allow for increasing the permissible normal load in sliding contact, e.g. on the piston skirt. This can allow for shifting the border of downsizing and may be an indirect but very effective approach to increase the overall efficiency and reduce fuel consumption of vehicle engines. Checking the validity of the above hypothesis requires multi-stage research, with special emphasis on engine tests. These are pioneering studies and the authors do not know of any international publications which contain results of similar studies

The literature presents numerous papers whose experimental work consisted of determining the friction coefficient of CNTs by the method of simulation of dynamic processes on the atomic scale [31, 38, 44]. The friction and adhesion phenomena, in relation to a single CNT, were also the subject of research conducted using atomic force microscopes (AFM) [9, 15, 30].

The work carried out independently in a number of research groups has led to determining the coefficients of friction that differ by two orders of magnitude or more. Adhesion occurring at the atomic level makes it difficult to extrapolate the results of research conducted for single CNTs on the surfaces of macroscopic size. The results of the research of friction processes in the microscopic scale, however, allow for clarification of the following information for the engine tests:

- the friction force of CNTs is largely dependent on the direction of movement relative to their axis
- an increase in temperature increases the thermal motions of atoms and in the atomic scale leads to increased friction force
- the diameter of the CNT does not substantially affect the value of the friction force
- the friction force increases with the speed of the CNT movement relative to the substrate
- atoms of non-carbon elements attached to the outer surface of the CNTs can greatly reduce the friction force; the use of fluoride [42] can reduce the coefficient of friction by 0.002–0.070.

Due to the relatively weak interaction between the opposite walls in multi-walled carbon nanotubes (MWCNTs), solely resulting from van der Waals forces, they are deformable. The deformations are elastic and reversible, and the CNTs are not destroyed in the process, due to the strong covalent bonds between adjacent carbon atoms. In the studies discussed in [37] single-wall and multi-wall nanotubes were subjected to loads in the plane perpendicular to their axis. A linear dependence of strength and deformation was found, which allowed for the determination of the Young's modulus. For single-wall carbon nanotubes (SWCNTs) a modulus of 810 ±410 GPa was obtained, while for MWCNTs with a diameter of 26 nm to 76 nm, it was 1.28 ±0.59 TPa. In the same study it was found that the mechanical properties obtained in the catalytic synthesis of MWCNTs strongly depend on their structure. The resiliency of the atomic structure of the CNT may be used for the covering layer of the piston skirt to dampen the forces caused by lateral motion of the piston.

1.3. Research of layers formed from carbon nanotubes performed outside the engine

The laboratory research of layers of CNTs obtained by the catalytic synthesis on the surface of silicon carbide is documented in the literature [3]. The surface of the substrate was sprayed with nickel nanoparticles which constitute a catalyst for the synthesis of CNTs. This synthesis was plasma-assisted, and the choice of plasma parameters enabled the shaping of adhesive properties in obtained layers. The tribological testing was performed using a ball pressed against a rotating plate, in a vacuum and in moist air. The results show the benefits of the strong bond between the layers of CNTs and the parent material. The lowest friction coefficient of less than 0.1 was obtained for layers with high adhesion, which did not undergo mechanical destruction. Furthermore, it was observed that in order to reduce friction, it is desirable to use layers of CNTs with a high order parameter.

A later, independent project [1] synthesized CNTs of ordered parallel structure on the sample surface of stainless steel. In one of the experiment series an intermediate layer of cobalt was used, resulting in more compact growth of CNTs and strongly favorable tribological properties.

Although the research results shown did not include the use of oil or any other lubricant, the information formulated on the basis of these results may be useful in understanding the phenomena of the boundary lubricating regime on the piston skirt.

The subject of the research presented in [40] was the vibration damping properties of epoxy resin containing carbon fibers, on the surface of which CNTs have been synthesized. CNTs entangling the carbon fibers led to a substantial increase in contact area with the resin, and enabled a significant improvement in the damping properties of the composite. The damping and energy dissipation, the authors explained, is the result of the friction occurring between the resin and CNTs. Presented composites [27, 40] may serve as an inspiration to create layers to replace the graphite piston skirt coating. Similar materials are already used in commercially produced friction bearings [2, 34, 36].

In parallel to the research into resins described above, works are also carried out in order to create CNT reinforced composites based on aluminum. This is usually achieved by using powder metallurgy; CNTs are mixed with metal powder, sintered and subjected to an extrusion process [25]. The technique is time-consuming, costly and difficult to use in high-volume production of engine pistons. The alternative is a modification of the piston surface material, which may include the introduction of CNTs into the aluminum alloy in the friction stir process. A description of such a successful experiment can be found in [21, 28, 29], where at the same time the resistance of the SWCNTs to high temperature that occurs temporarily during the friction process was confirmed.

2. Materials and methods

2.1. Research concept

Particularly preferential tribological properties of carbon nanotubes reported in microscopic scale studies using AFM were confirmed also in relation to the macroscopic surface properties studied in a tribometer. The aim of the research presented in this article was to verify whether carbon nanotubes deposited on the piston skirt can effectively contribute to the reduction of internal combustion engine friction losses.

The authors conducted their most extensive studies of CNT covered pistons using the original test stand built as part of a doctoral thesis [24] and described in detail later in the monograph [23]. Due to its design the constructed test stand allows the simulation of research conditions closer to the complete working engine than a classic tribometer. This test stand is used to measure the sum of friction losses in the piston assembly and the crankshaft bearings in conditions similar to those prevailing in an operating engine.

The concept of the study is a comparison of the motoring torque of engine mounted with the standard pistons with the corresponding values for engine with the experimental pistons coated with a layer of MWCNTs on the skirt.

Directly after installing the experimental pistons in the engine preliminary test lasting 100 minutes was performed at a constant oil temperature of 80°C and at a constant speed of 1000 rpm, while monitoring the torque. The purpose of this initial test was the rejection of pistons, which did not provide stable working conditions.

Both for the reference pistons and the experimental pistons fundamental tests were performed for 96 operating points of the engine at a wide range of oil temperatures (50°C, 80°C and 110°C), rotational speeds of the crankshaft (set in steps of 250 rpm starting at 500 rpm up to 3000 rpm) and load, simulated by changing the air pressure for the cylinder supply (0 bar, 1 bar and 1.5 bar).

The experimental pistons which passed through all the stages of engine research had a total engine running time of about 10 hours.

2.2. Experimental pistons

Experimental pistons were made by the NanoLab Inc. company using a procedure developed by that company. Experimental pistons were prepared by covering the skirt surface of the standard aluminum pistons with a layer of industrial grade MWCNTs of diameter around 15 nm, and the of length in the range 5…20 μm. The solution was prepared from four constituents: 100 ml of distilled water, 300 mg of dodecylbenzensulfonic acid (DBS), 300 mg of MWCNT PD15L5-20, 5 ml of potassium silicate solution (KASIL 1, 2.50 weight ratio potassium silicate, 29.1% K_4SiO_4 solution in water. PQ Corporation, P.O. Box 840, Valley Forge, Pa. 19482, USA.) The distilled water, MWNCTs, and DBS were sonicated with a horn sonicator for 10 min. The potassium silicate was then added, and the complete solution was stirred for 1 min.

The aqueous solution of CNTs was applied in a number of successive passes by spraying onto the surface of the piston, which had been pre-heated to 95°C. A few tens of milliliters of the solution were used to cover the skirt surface of a single piston. The process was finalized by keeping the piston at 300°C for 1 h.

In order to develop the technology, many tests have been performed using cut parts of the piston and later with whole pistons. In total, tens of pistons were used, but only six of them were considered adequate to test in the engine, creating three sets of pistons for a two-cylinder engine. Finally, only one set of pistons (pistons labelled A2 and A3) successfully passed the preliminary engine test and was used in the fundamental friction tests. Figure 1 is a view of a standard aluminum piston used for the reference test and the final version of the experimental piston with a layer of CNTs on the side surface. The proposed coating of CNTs is the subject of extensive research as an alternative to the standard coatings of graphite or molybdenum [12–14, 26, 32].

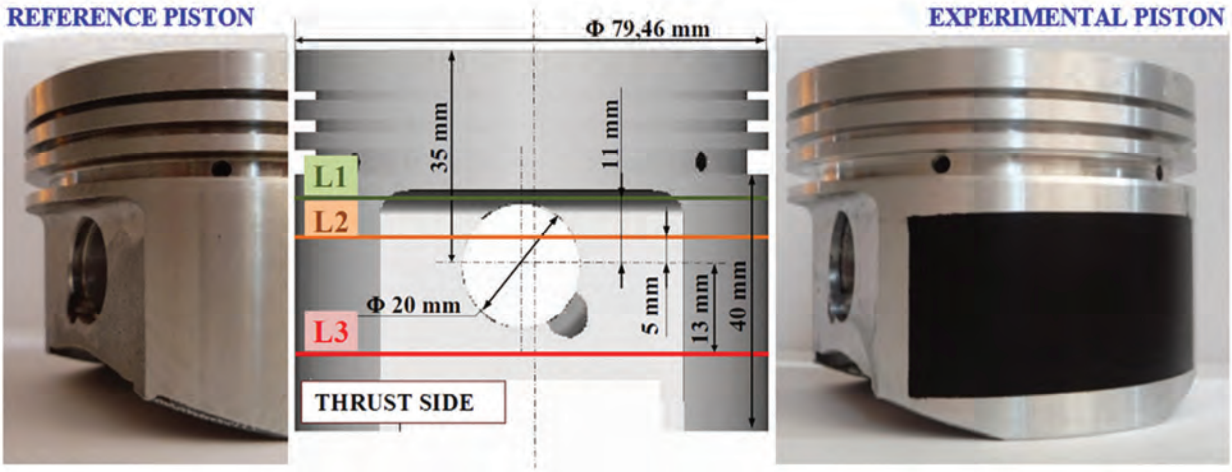

Fig. 1. The original piston made out of aluminum alloy, and an experimental piston coated with CNTs, showing horizontal levels L1-L3 determined for further assessment of wear

2.3. Test bench

The test bench (Fig. 2) consists of a modified two-cylinder in-line internal combustion engine driven by an electric motor. The torque is transmitted through the shaft with an HBM type T5 torque meter of range 50 Nm, which enables accurate measurement of torque (the relative standard deviation of reproducibility declared by manufacturer according to DIN 1319 was as low as ±0.025 Nm). The Spider 8 device produced by HBM was used for recording the measurement signal. Each of the torque values presented in this paper is an average calculated from 20,000 consecutive measurements recorded at a frequency of 9.6 kHz.

The engine camshaft is immobilized, leaving all valves in the closed position; the crankshaft-driven water and oil pumps were also immobilized and replaced with outside units, powered by individual electric motors. The applied changes meant that during each revolution of the crankshaft the piston forces compression and decompression of the load contained in the cylinder, while a portion of the cylinder load leaks into the crankcase. With the engine valves closed, blow-by gases can be countered by the use of additional one-way valves mounted in place of the spark plugs, and named load refill valves. The test bench design permits opening and closing of these valves to allow free air intake, either from the ambient air or of air supplied at a certain overpressure. Funneling more air into the cylinder at the beginning of the compression stroke under increased pressure causes an increase in the maximum cylinder pressure. This is a method to simulate increased load in a real engine.

A very important original feature is the system that maintains a constant oil temperature with an oil-engine cooling liquid heat exchanger, with a radiator, a heater and electrically powered coolant and oil pumps. The PID controller makes it possible to maintain the desired oil temperature with ±0.2°C accuracy, ensuring the reproducibility of the measurements. For the standard engine configuration the deviation of the medium torque value in a series of 20 000 standard recording data points never exceeded 0.05 Nm. This was confirmed during the tests involving the same working conditions, performed independently at seven day intervals.

In comparative studies presented later in this article, a standard Castrol Edge engine oil with viscosity grade 5W/30 and quality class API SL was always used.

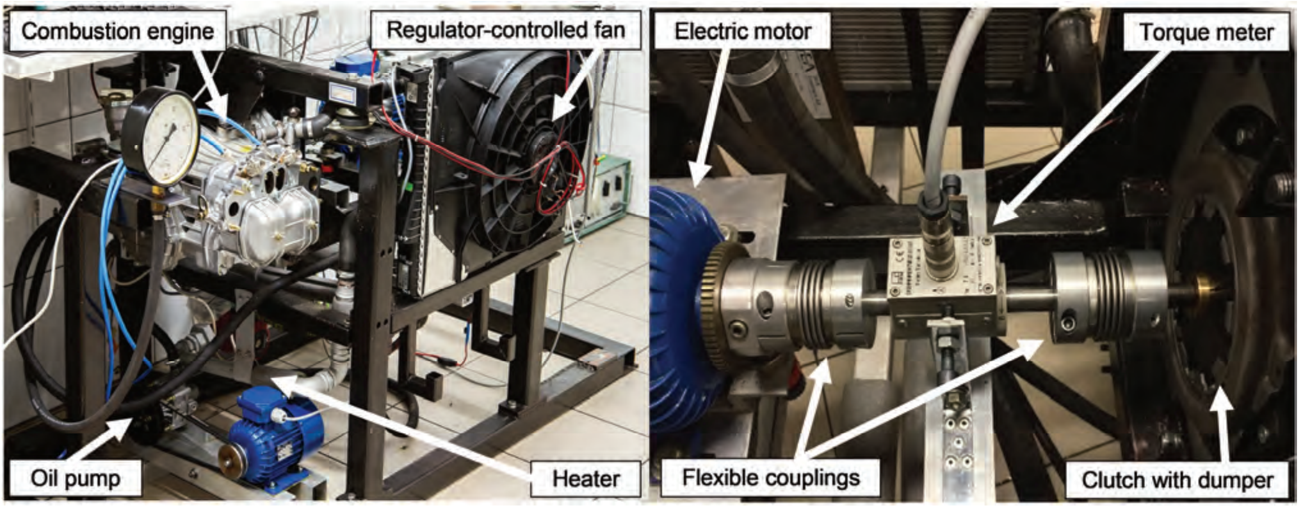

Fig. 2. The test bench for measuring the friction losses in the crank mechanism; general view on the left and a method for measuring the torque of the motoring torque on the right

2.4. Piston surface characterization

Studies of experimental engine pistons are preceded by a series of experiments designed to characterize the layer of carbon nanotubes; many of these studies were repeated after the engine test and removing the pistons from the engine.

- Testing the roughness of reference pistons surface, experimental pistons before application of CNTs, after application of CNTs, after the engine tests: Mahr Perthen Perthometer S8P profiler with a contact measuring tip RHT6-50 was used. Stylus tip radius was 5 μm and the pressure force was 0.8...1.2 mN.
- Examination of the surface shape of the reference and experimental pistons before the application of CNTs, after the application of CNTs and after engine tests: Coordinate measuring machine DEA Global Image 7.7.5. with the Renishaw SP25M probe head and SM25-2 module; measuring tip with a length of 62 mm and a measuring ball of diameter 6 mm was used.
- Formtester used for the measurement of the CNT layers' wear: Hommel etamic roundscan 535.
- Examining the shape of the cylinder walls before and after the tests, to determine the wear of cylinder running surfaces: digital bore gauge Mitutoyo 511-501.
- Computer tomography of the pistons in order to eliminate hidden defects in materials: GE v|tome|x s 240.
- Examining the CNT layer structure: SEM Mira 3 Tescan and Jeol JSM-7001F microscopes.
- EDS: Princeton Gamma-Tech, Inc.

3. Results

3.1. Engine friction measurement

Figure 3 shows a comparison of the results obtained in preliminary tests made on one of a test version of the pistons and the final version of the piston. Due to the clearly unstable behavior of the friction losses of the engine pistons with experimental pistons the test was discontinued, the test made for the final version of pistons was completed successfully. Due to the fact that the methodology of measurement in the preliminary test and the actual tests was identical, the obtained results may also be used to assess the reproducibility of the measurements.

Figure 4 shows a comparison between the motoring torque for the engine with the standard and experimental pistons A2 and A3. Each of the three graphs shows the torque registered over speed range for a defined oil temperature. Each point in Figure 4 was created by calculating the mean value of engine motoring torque, which was recorded for about two seconds. The example comparison of instantaneous engine motoring torque for reference and CNT covered pistons, registered at 500 rpm and 50 Celsius degree of the oil temperature, is show in Fig. 5. For each temperature there were three series of tests, varying in terms of piston side load, resulting from the pressure of the air supplied to the cylinder. The oil temperature and cylinder supply air pressure are given in the description of the measurement series; the higher the air pressure, the higher the gas force and the resulting normal force pressing the piston against the cylinder wall.

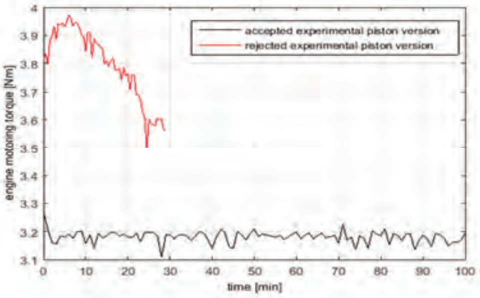

Fig. 3. Preliminary engine test of two CNT-coated experimental piston versions representing early and final development stages; comparing the stability of the engine motoring torque over time

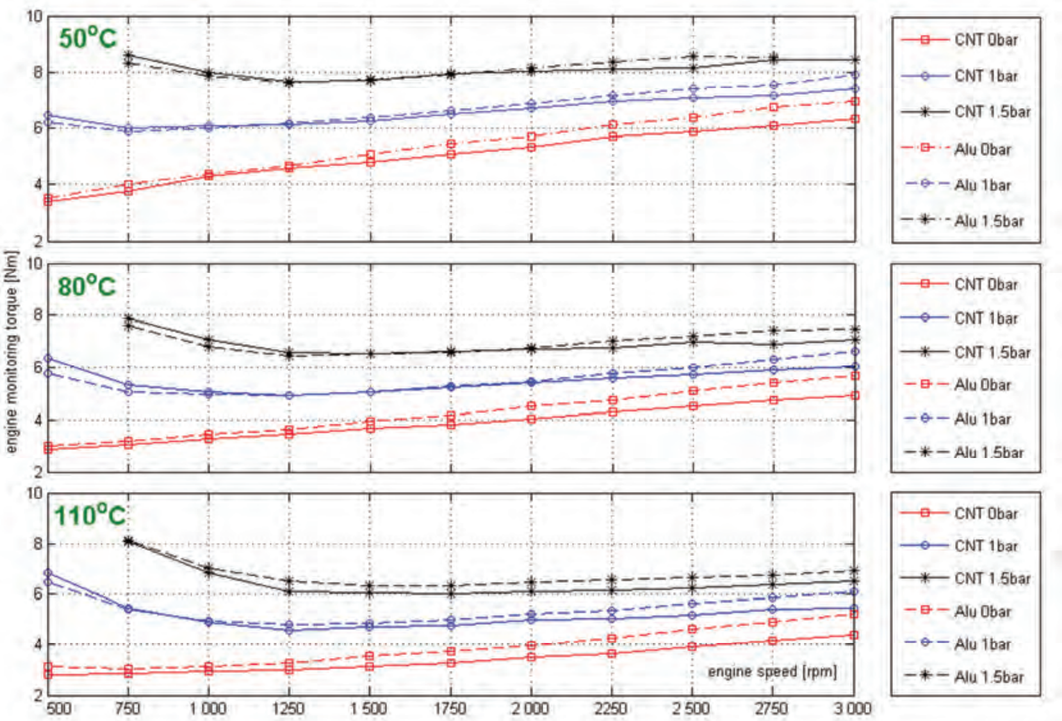

Fig. 4. Comparison of engine friction losses of standard aluminum pistons and pistons coated with CNTs, as a function of engine speed; results measured at different engine oil temperatures and cylinder supply pressures

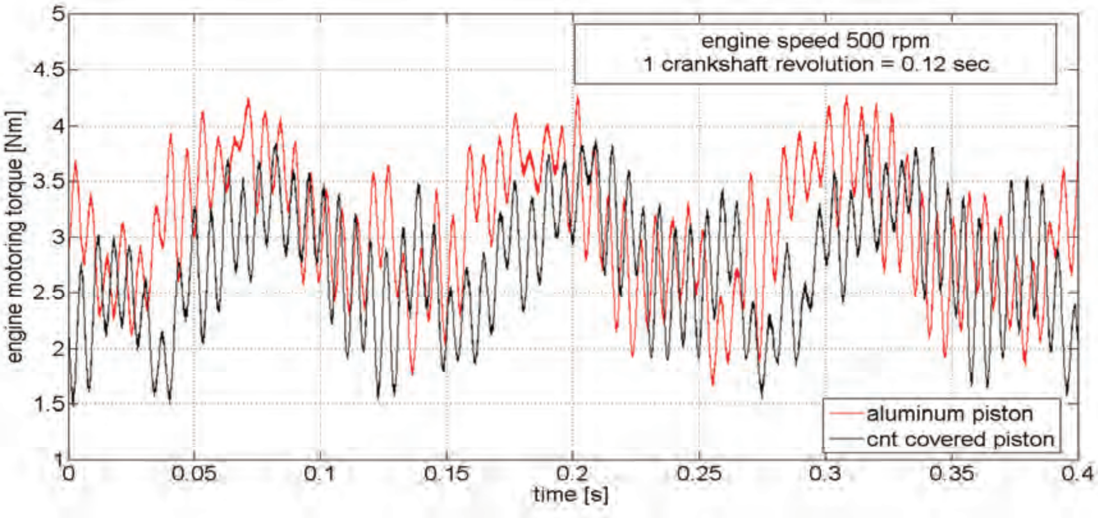

Fig. 5. Comparison of engine motoring torque raw signal for reference aluminum and CNT covered pistons

3.2. Characterization of the CNT layer on the experimental pistons

After dismounting the experimental pistons from the engine, it was found that the adhesion of the layer of CNTs on the aluminum surface of the piston was sufficient and no layer peeling occurred. Signs of rubbing of the layer of CNTs on the cylinder wall could be seen by naked eye; the layer of CNTs had been clearly smoothed, but at no point was it scratched to reveal the aluminum surface. The intensity of the abrasion phenomenon of the layer of CNTs can be inferred from Fig. 6, which shows the results of measurement of the shape of the experimental piston skirt before mounting it in the engine and after the engine test. Indirectly, the wear on the CNT layer surface also shows a reduction in surface roughness during engine operation. Surface roughness was measured for each of the piston for six sections symmetrically located on the circumference, each measuring section had a length of about 12 mm. The most characteristic surface profiles are shown in Fig. 7, an overview of the basic parameters is shown in Table 1.

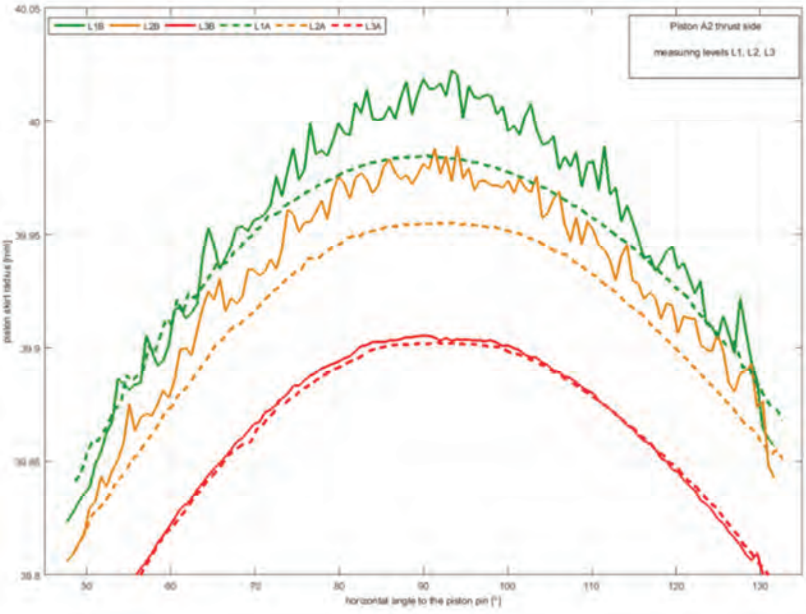

Fig. 6. The radius of the piston skirt coated with CNTs, measurements on the piston thrust side in horizontal levels L1, L2, L3. Results obtained with the coordinate measuring technique before installing the piston in the engine (solid line L1B, L2B, L3B) and after the engine test (dashed line L1A, L2A, L3A)

Table. 1. Parameters describing the surface roughness of tested pistons

Piston		Reference	A2 and A3 Experimental (average values)				
Research phase		after engine tests	before applying CNTs	before engine tests	after engine tests		
Measurement method		mean	mean	mean	major thrust side	minor thrust side	mean after tests
Parameter	Ra	3.99	3.39	4.72	3.33	4.18	3.75
	Rq	4.57	3.95	5.78	3.80	4.85	4.33
	Rt	15.57	16.91	38.41	17.42	24.21	20.82
	Rsk	–0.06	0.79	0.4	0.26	0.23	0.24

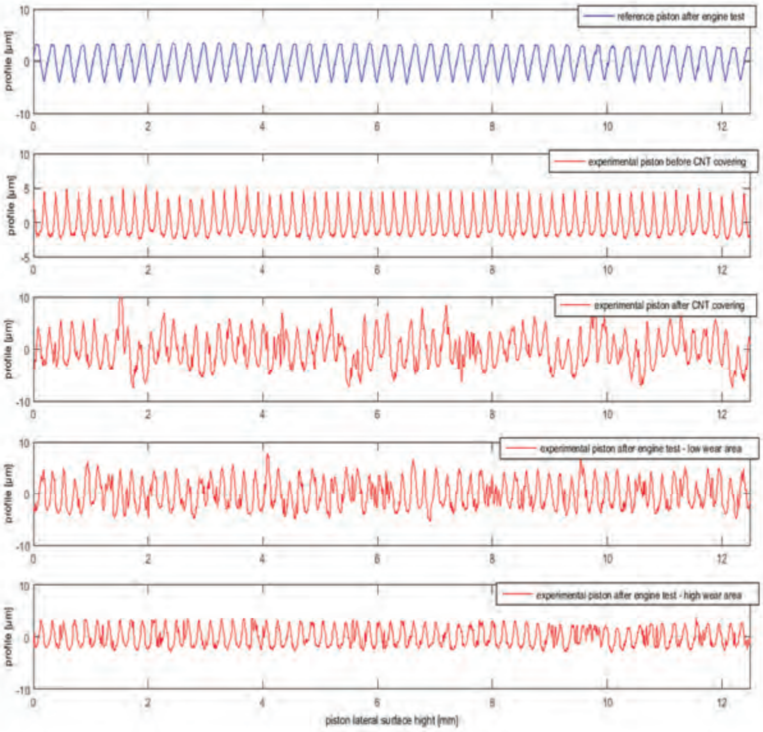

Fig. 7. Selected characteristic profiles of the lateral surface of the pistons used in the friction measurements

The upper part of Fig. 8 shows the shape of the bearing surface of the piston with a layer of nanotubes. The piston shape is presented, where the horizontal axis represents the perimeter of the piston's bottom side. The lower part of the figure presents the topography of the surface in the same form. The images on the left show the major thrust side of the piston, while the images on the right the minor thrust side. All the data shown relate to piston A3, where the relative values were the same for the second experimental piston. The images show the surface of pistons that were taken out of the engine after the end of the engine tests.

Before mounting the piston and at the end of the engine tests the diameter of the cylinders was measured in 52 cylinder sections. There were no significant signs of wear and the average wear of all sections was 0.8 µm.

Figure 9 shows the structure of a layer of CNTs on the surface of the experimental piston. This SEM image was recorded for the piston taken out of the engine at the end of the engine experiment. Before taking the image, the sample was washed in acetone.

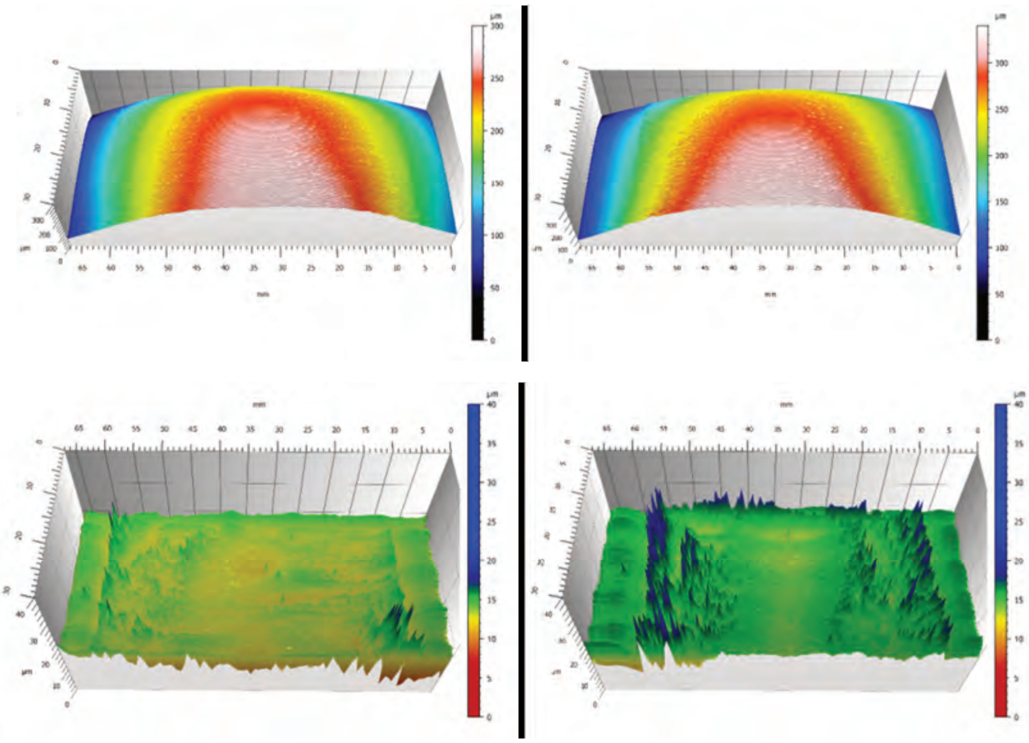

Fig. 8. Piston wear as a result of the engine tests; the bearing surface on the major thrust side shown on the left and minor thrust side on the right; the shape of the bearing surface of the piston coated with nanotubes shown on the top and the surface topography on the bottom

The EDS analysis has found that in addition to carbon, the surface composition also contained aluminum and iron, which are the products of abrasion of friction components. The aluminum alloy also contained silicon; while oxygen and potassium are substances used in the process of applying the CNTs. Spectroscopy results are shown in Fig. 10.

The EDS analysis has found that in addition to carbon, the surface composition also contained aluminum and iron, which are the products of abrasion of friction components. The aluminum alloy also contained silicon; while oxygen and potassium are substances used in the process of applying the CNTs.

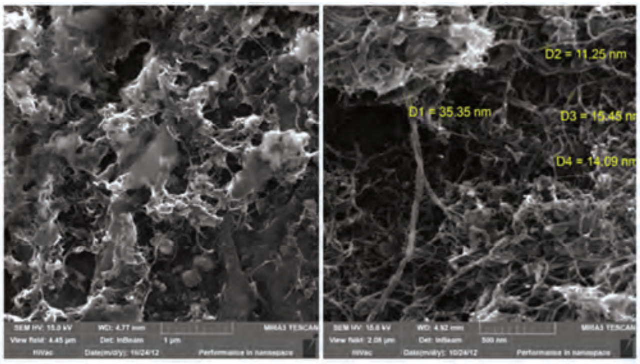

Fig. 9. The surface of the CNTs on the piston; image captured after the completion of the engine tests from a sample washed in acetone

Live Time: 65.31 Count Rate: 3169 Dead Time: 27.55 %
Beam Voltage: 10.00 Beam Current: 2.00 Takeoff Angle: 55.22

ELEMENT	LINE	WT %	AT %
C	KA1	77.94	86.40
O	KA1	10.15	8.44
Si	KA1	6.81	3.23
K	KA1	1.94	0.66
Fe	KA1	1.08	0.26
Al	KA1	0.92	0.46
Na	KA1	0.55	0.32
S	KA1	0.35	0.14
Ca	KA1	0.26	0.09
TOTAL		100.00	100.00

Fig. 10. EDS spectroscopy for the surface of CNT layer on the piston dismounted after completing the engine tests

A series of experimental studies of pistons was finalized with a computer X-ray tomography of the experimental pistons. CT scan shows the close adhesion of the CNTs to the material of the piston; no presence of any air bubbles was found at the layer border.

3.3. Ideas for improving the technology for application of carbon nanotubes

This article presents a spray method of application of CNTs on the piston skirt which is only one of many possible methods. An alternative technique is to use a layer of resins, polymers containing CNTs with proved favorable tribological properties [10, 16, 19, 20, 34, 35, 40, 43]. The use of IG-type CNTs with ferromagnetic catalyst nanoparticles at their ends enables an external electromagnetic field to interact with the CNTs and produce an ordered spatial structure.

The authors have, however, researched the possibility of using another original method based on electrolytic deposition of MWCNTs from an aqueous solution. Suitable preparation of the piston surface, and conducting the CNT deposition process using a periodically reversing current, made it possible to obtain a layer with high adhesion and promising properties. These layers are characterized by a relatively ordered spatial structure (Fig. 11), different from the structures obtained by spraying CNTs onto a surface. Using the piston layer of CNTs obtained by the process of electrodeposition, the anisotropic properties of the CNTs could be taken advantage of in order to reduce friction.

In the long term one can imagine a hierarchical, multi-layered structure of CNTs applied on the piston skirt, where each layer would have a specialized function. The layer closest to the piston material would provide high adhesion, then a layer of damping, the next layer with favorable tribological properties, and the contact surface layer would protect a new engine from seizing. It seems likely that the use of nanoparticles of established favorable tribological characteristics (Co, Mo, W) could contribute to the improvement of properties of hierarchical layers based on CNTs.

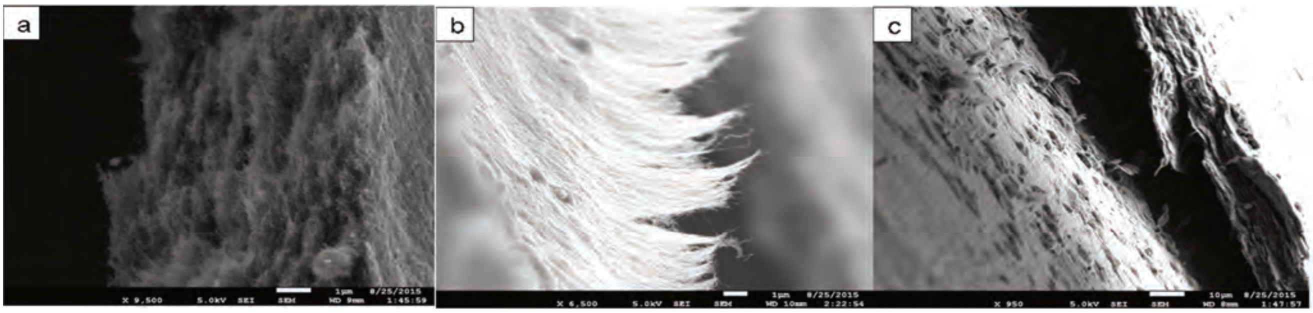

Fig. 11. The layers of CNTs obtained in the process of electrolytic deposition: a) ordered structure of CNTs shown in a cross-section of layers; b) ordered structure of CNTs on the surface of the layer after bending and rupture; c) oxide layer on the metal surface formed by a chemical method significantly enhances the CNT adhesion to the base metal surface (left part of the picture), even if the CNT layer is broken down the metal surface will not be cleaned of CNTs

4. Analysis of the results

The analysis of the results was divided into two parts: the main part concerns the results of friction losses, the second part is a supplementary research conducted to better understand the phenomena and processes occurring in the engine and determining friction and wear.

4.1. Ideas for improving the technology for application of carbon nanotubes

It should be considered that the recorded engine motoring torque values are determined by the following main components:

a) friction losses occurring between the piston skirt and the cylinder, which are the subject of the analysis in this study
b) friction losses between the piston rings and the cylinder
c) friction losses in the crankshaft bearings
d) the escape of part of the compressed load from the cylinder to the crankcase (blow-by), and thermodynamic losses associated with heating the cylinder walls.

It can be assumed that the layer of CNTs on the piston skirt surface does not substantially affect the processes listed in points b-d. Therefore, comparison of the engine motoring torque registered in the same operating conditions of the engine for the standard pistons and piston coated with CNTs should allow determining the impact of the layer of CNTs on friction losses.

The use of CNTs on the piston skirts resulted in a significant reduction in friction losses, expressed by a decrease in the engine motoring torque, reaching up to 16% in certain engine operating conditions (Fig. 4). It should be emphasized that the disclosed difference relates to the overall friction losses, which beside the loss at the piston skirt, also consists of friction losses caused by piston rings and bearings of the crankshaft. The test results presented in the literature indicate that all three of these kinematic pairs are comparable in terms of friction losses [32, 33]. Therefore, the reduction of friction losses recorded after installing the experimental pistons, in which only the skirt surface material was changed, is surprisingly high.

It is suspected that such a large reduction in friction losses, observed after mounting the experimental pistons with a CNT layer, should not be attributed solely to friction changes on the piston skirt. Supplementary research has shown that the prototype CNT layer was characterized by rapid wear – during a few hours of research preceded by several hours of engine run-in the CNT layer thickness receded by about 20 μm due to wear (see Figs 6 and 8). The ablated CNTs have probably dispersed well in the engine oil, due to the continuity of the process of attrition, and could reach all the friction components with the oil circulating in the engine and noticeably reduce the total friction losses.

The study compares the engine friction losses for CNT coated experimental pistons with the corresponding values measured for standard pistons provided by the engine manufacturer, which are aluminum pistons without any additional layers on the side surfaces. The resin containing graphite or molybdenum disulfide substances widely used nowadays to cover pistons may also help to reduce friction losses, but the benefits are incomparably smaller than the values observed in our studies [12, 17, 26, 32].

Engine friction losses under normal operating conditions occur primarily in the hydrodynamic friction regime. The share of the engine friction losses induced in the mixed friction regime, which become particularly noticeable at low engine speed and high engine load is limited in comparison. CNTs present in the oil may reduce friction losses for both the hydrodynamic and mixed friction regimes, the relevant mechanisms (the effects of nanotubes) are discussed in detail in [8]. The study described in this paper shows a clear relation between reducing friction losses resulting from the application of nanotubes and engine speed and load. The higher the engine speed and the lower the engine load, the more pronounced the observable benefits of using nanotubes. This may seem to indicate that CNTs in the oil reduce the friction losses primarily in the hydrodynamic friction regime. However, according to the authors, the reasons for the observed reduction in friction losses relative to the engine speed are much more complex, and may include the mechanisms described in [8]; furthermore, high engine speed promotes better dispersion of nanotubes in the oil circulating in the engine lubrication system.

4.2. Analysis of supplementary research results

Testing the shape of the pistons using the coordinate measuring technique was performed for the reference and experimental pistons before and after the engine test. The diameter of the reference pistons measured after completion of the study was 79.998 mm and the diameter of the experimental pistons dismounted from the engine after the study was 79.990 mm. These values are similar and it can be assumed that the difference of 8 microns did not have a direct impact on the recorded friction losses.

The surface roughness of the reference piston and the run-in experimental piston had similar Ra values equal to 3.99 microns and 3.75 microns, respectively. A very important condition for ensuring comparability of results of friction losses was therefore satisfied.

The applied layer of CNTs originally had a thickness of about 40 microns (Fig. 6), although the precise value is difficult to determine because of the roughness of the surface of the aluminum piston and the surface roughness of the nanotubes. Similar relationships exist with respect to standard graphite layers and molybdenum.

In the images showing the surface of the pistons taken out of the engine at the end of the study (Fig. 8) the edges of the regions covered with nanotubes are easily visible, mainly as the lines perpendicular to the horizontal axis, intersecting the axis around the coordinates 5 mm and 60 mm. The images showing the surface topography reveal the character of the wear in CNT layers, where the roughness of the CNT layer surface is visibly reduced in the central part of the piston surface. As expected, the wear process occurred more heavily on the major thrust side of the piston.

The layer of CNTs does undergo wear while the engine operates, which is due to the limited cohesion of the spray-coated CNT layer. SEM images of the CNTs taken on the piston dismounted after the engine tests show, however, that the conditions in the engine do not lead to the destruction of the CNTs.

Comparing the shape of the cylinder measured before and after the piston test does not indicate the existence of significantly accelerated cylinder liner wear; however, the relatively short test cannot replace durability tests. The disassembly of the engine carried out after completing the experimental piston tests did not reveal any worrying signs of accelerated wear in any of the friction components, in particular in the piston assembly and the crankshaft bearings.

Based on the SEM images and the EDS analysis, the ability of CNTs to attach foreign particles onto their surface can be observed. These particles attached during engine running could be called pollution in the technical evaluation of CNT images, but from the tribological point of view they can play a beneficial role. This feature can be used to deliberately decorate the CNTs with nanoparticles which have proven favorable tribological properties.

5. Conclusions

A prototype piston with a CNT-coated skirt was prepared and successfully tested for the first time in an engine. The described technique of applying CNT layers enabled the creation of experimental pistons, but it requires improvements in order to enhance the layer durability. Therefore, it is not yet suitable for industrial use. After successful modification of certain details, the proposed technology of applying layers of CNTs can be adapted for use in industrial-scale production.

Images of the samples taken at the surface of the piston after engine tests, recorded using a scanning electron microscope (SEM), confirm the survivability of the CNTs and their resistance to the chemical environment and mechanical loads on the piston skirts.

The experimental pistons dismounted from the engine were not significantly different in outer diameter or surface roughness compared to the reference pistons; thus the basic criterion for the comparability of friction losses was fulfilled.

The results of the main part of the study indicate that following the application of CNTs onto experimental pistons, significantly decreased friction losses occurred. The difference in motoring torque of the engine with regular pistons and the CNTs coated pistons reached up to 16%.

On the basis of measurements of piston surface roughness and shape made before and after engine tests a high level of abrasion of the CNTs layer can be observed. However, this problem arises primarily from the type of binder, and not the properties of the CNTs and so this may be easily resolved in the future.

It is likely that the significant reduction in the engine motoring torque registered in the experiments using pistons coated with CNTs is not solely due to the modification of the contact conditions of the piston with the cylinder. The CNTs are continuously abraded off the surface of the piston and dispersed in the oil where they can then reach all the friction components in the engine. If the described effect indeed appeared during engine operation, it would be possible to use easily replaceable elements to control the release of CNTs into the oil, for example: timing chain guides. This approach would be a good solution to the instability problem of CNT enriched oils.

It has been shown that CNTs do not adversely affect the process of wear of the cylinder liner.

The results of the research on alternative, electrodeposition methods of applying the CNT layers onto the surface of the piston have been presented and a functionally specialized hierarchical CNT multilayer coating was proposed.

ACKNOWLEDGEMENT – The authors would like to thank all those who contributed to the final outcomes presented in the paper, by giving inspiration for the research, supporting laboratory tests, scientific cooperation, development and revision of the article. We are particularly thankful to David Carnahan, the president of NanoLab Inc., the exclusive supplier of the CNTs used in our research. We wish to give special thanks to professors Antoni Iskra and Michał Ciałkowski.

FUNDING – This work was supported by the Polish National Science Centre [N N502 511240], the Institute of Combustion Engines and Transport, Poznan University of Technology, Poland and NanoLab, Inc. Waltham, MA, USA.

Bibliography

[1] ABAD, M.D., SÁNCHEZ-LÓPEZ, J.C., BERENGUER-MURCIA, A. et al. Catalytic growth of carbon nanotubes on stainless steel: characterization and frictional properties. *Diamond and Related Materials*. 2008, **17**(11).

[2] ADAM, A., PREFOT, M., WILHELM, M. Kurbelwellenlager für Motoren mit Start-Stop-System, *MTZ*. 2010, **12**.

[3] ATSUSHI, H., NOBUAKI, Y. Sliding friction properties of carbon nanotube coatings deposited by microwave plasma chemical vapor deposition. *Tribology International*. 2004, **37**(11-12).

[4] BAUGHMAN, R.H., ZAKHIDOV, A.A., DE HEER, W.A. Carbon Nanotubes – the route toward applications. *Science*. 2002, 787-792.

[5] BHUSHAN, B. Handbook of nanotechnology. *Springer-Verlag*. Berlin-Heidelberg 2010.

[6] BOSSDORF-ZIMMER, B., KRINKE, S., LÖSCHE-TER, H.T. Die well-to-wheel-Analyse Umwelteigenschaften mess- und planbar Machen. *MTZ*. 2012, **2**.

[7] Carbon nanotubes, www.nano-lab.com.

[8] CHAUVEAU, V. Le pouvoir lubrifiant des nanotubes de carbonne. *PhD dissertation*. L'Ecole Centrale de Lyon, 2010.

[9] COOK, E.H., BUEHLER, M.J., SPAKOVSZKY, Z.S. Mechanism of friction in rotating carbon nanotube bearings. *Journal of the Mechanics and Physics of Solids*. 2013, **61**, 652-673.

[10] CUI, L.J., GENG, H.Z., WANG, W.Y. et al. Functionalization of multi-wall carbon nanotubes to reduce the coefficient of the friction and improve the wear resistance of multi-wall carbon nanotube/epoxy composites. *Carbon*. 2013, **54**.

[11] DE VOLDER, M.F., TAWFICK, S.H., BAUGHMAN, R.H. et al. Carbon nanotubes: present and future commercial applications. *Science*. 2013, 339.

[12] DEUSS, T., EHNIS, H., BASSET, M. et al. Reibleistungsmessungen am Befeuerten Dieselmotor – Zyklusrelevante CO2-Ersparnis. *MTZ*. 2011, **12**.

[13] DEUSS, T., EHNIS, H., FREIER, R. et al. Reibleistungsmessungen am Befeuerten Dieselmotor – Potenziale der Kolbengruppe. *MTZ*. 2010, **5**.

[14] DEUSS, T., EHNIS, H., ROSE, R.K. et al. Reibleistungsmessungen am Befeuerten Dieselmotor – Einfluss von Kolbenschaftbeschichtungen. *MTZ*. 2011, **4**.

[15] FENIMORE, A.M., YUZVINSKY, T.D., HAN, W.Q. et al. Rotational actuators based on carbon nanotubes. *Nature*. 2003, **424**.

[16] GOLCHIN, A., WIKNER, A., EMAMI, N. An investigation into tribological behavior of multi-walled carbon nanotube/graphene oxide reinforced UHMWPE in water lubricated contacts. *Tribology International*. 2016, **95**.

[17] GOLLOCH, R. Downsizing bei Verbrennungsmotoren. *Springer-Verlag*. Berlin-Heidelberg 2005.

[18] HOLMBERG, K., ANDERSSON, P., ERDEMIR, A. Global energy consumption due to friction in passenger cars. *Tribology International*. 2012, **47**.

[19] HUANG, Y.Y., TERENTJEV, E.M. Dispersion of carbon nanotubes: mixing, sonication, stabilization and composite properties. *Polymers*. 2012, **4**.

[20] HWANG, H.J., JUNG, S.L., CHO, K.H. et al. Tribological performance of brake friction materials containing carbon nanotubes. *Wear*. 2010, **268**.

[21] JOHANNE, L.B., YOWELL, L.L., SOSA, E. et al. Survivability of single-walled carbon nanotubes during friction stir processing. *Nanotechnology*. 2006, **17**.

[22] JOLY-POTTUZ, L., DASSENOY, F., VACHER, B. et al. Ultralow friction and wear behavior of Ni/Y-based single wall carbon nanotubes (SWNTs). *Tribology International*. 2004, **37**.

[23] KAŁUŻNY, J. Experimental applications of carbon nanotubes in the construction of internal combustion engines. *Poznan University of Technology Publishing House*, Poznan 2013.

[24] KAŁUŻNY, J. Wpływ kształtu powierzchni bocznej tłoka na parametry filmu olejowego pokrywającego gładź cylindra. *Doctoral dissertation*. Poznan 2004.

[25] KASHYAP, K.T., RAHUL, R., YAMDAGNI, S. Strengthening in carbon nanotube/aluminum (CNT/Al) composites. *Scripta Materialia*. 2005.

[26] KENNEDY, M., HOPPE, S., ESSER, J. Kolbenringbeschichtung zur Reibleistungssenkung im Ottomotor. *MTZ*. 2012, **5**.

[27] LIN, R.M., LU, C. Modeling of interfacial friction damping of carbon nanotube-based nanocomposites. *Mechanical Systems and Signal Processing*. 2010, **24**(8).

[28] LIU, Q., KE, L., LIU, F. et al. Microstructure and mechanical property of multi-walled carbon nanotubes reinforced aluminum matrix composites fabricated by friction stir processing. *Materials and Design*. 2013, **45**.

[29] LIU, Z.Y., XIAO, B.L., WANG, W.G. et al. Developing high-performance aluminum matrix composites with directionally aligned carbon nanotubes by combining friction stir processing and subsequent rolling. *Carbon*. 2013, **62**.

[30] LU, H. et al. Friction and adhesion properties of vertically aligned multi-walled carbon nanotube arrays and fluoro-nanodiamond films. *Carbon*. 2008, **46**.

[31] LUCAS, M., PALACI, I., RIEDO, E. et al. Hindered rolling and friction anisotropy in supported carbon nanotubes. *Nature Materials*. 2009, **8**.

[32] Mahle GmbH – Piston and engine testing. Stuttgart 2012.

[33] MAUCH, A., TOPHOVEN, J., TRZEBIATOWSKI, T. et al. Potenziale und Grenzen des Downsizing beim Dieselmotor. *MTZ*. 2011, **7-8**.

[34] MENG, H., SUI, G.X., XIE, G.Y. et al. Friction and wear behavior of carbon nanotubes reinforced polyamide 6 composites under sliding and water lubricated condition. *Composites Science and Technology*. 2009, **69**(5).

[35] OLEK, M., KEMPA, K., JURGA, S. et al. Nanomechanical properties of silica coated multiwall carbon nanotubes-poly(methyl methacrylate) composites. *Langmuir*. 2005, **21**.

[36] QIANMING, G., DAN, L., XIAOSU, Y. et al. Tribology of polymeric nanocomposites. *Friction and Wear of Bulk Materials and Coatings*. 2013.

[37] SALVETAT, J.P. et al. Mechanical properties of carbon nanotubes. *Applied Physics*. 1999, **69**.

[38] SERVANTIR, J., GASPARD, P. Rotational dynamics and friction in double-walled carbon nanotubes. *Physical Review*. 2006, **73**.

[39] SPICHER, U. Analyse der Effizienz zukünftiger Antriebssysteme für die individuelle Mobilität. *MTZ*. 2012, **2**.

[40] TEHRANI, M. et al. Hybrid carbon fiber/carbon nanotube composites for structural damping applications. *Nanotechnology*. 2013, **24**.

[41] TUNG, S.C., MCMILLAN, M.L. Automotive tribology overview of current advances and challenges for the future. *Tribology International*. 2004, **37**.

[42] VANDER WALL, R.L. et al. Friction properties of surface-fluorinated carbon nanotubes. *Wear*. 2005, **259**(1-6).

[43] YAN, L., WANG, H., WANG, CH. et al. Friction and wear properties of aligned carbon nanotubes reinforced epoxy composites under water lubricated condition. *Wear*. 2013, **308**.

[44] ZHANG, S., LIU, W.K., RUOFF, R.S. Atomistic simulations of double-walled carbon nanotubes (DWCNTs) as rotational bearings. *Nano Letters*. 2004, **4**.

Jarosław Kałużny, DSc, DEng. – Faculty of Machines and Transport at Poznan University of Technology.

e-mail: *Jaroslaw.Kaluzny@put.poznan.pl*

Prof. Jerzy Merkisz, DSc., DEng. – Professor in the Faculty of Machines and Transport at University of Technology.

e-mail*: Jerzy.Merkisz@put.poznan.pl*

Krzysztof Kempa – Professor of Physics at Boston College, Department of Physics, Boston College.

e-mail: *Kris.Kempa@bc.edu*

Bartosz Gapiński, DEng. – Faculty of Mechanical Engineering and Management at Poznan University of Technology.
e-mail: *Bartosz.Gapinski@put.poznan.pl*

Emil Wróblewski, MEng. – postgraduate in the Faculty of Machines and Transport at Poznan University of Technology.

e-mail: *Emil.Z.Wroblewski@doctorate.put.poznan.pl*

Aleksander Stepanenko, MEng. – postgraduate in the Faculty of Machines and Transport at Poznan University of Technology.

e-mail: *Stepanenko@wp.pl.*

Mohanad Al-Karawi, MEng. – postgraduate in the Faculty of Machines and Transport at Poznan University of Technology.

e-mail: *Mohanad.Al-Karawi@doctorate.put.poznan.pl*

Article citation info:
DZIUBAK, T. Operational properties of performance engine intake air cleaners. *Combustion Engines*. 2018, **172**(1), 25-34.
DOI: 10.19206/CE-2018-103

Tadeusz DZIUBAK

CE-2018-103

Operational properties of performance engine intake air cleaners

The paper presents an analysis of the design of air cleaners in performance vehicles. The paper confirms that their fundamental property is a much lower flow resistance compared to standard air cleaners. The consequences of replacing a standard air filter element with a performance one have been described. The impact of this modification i.e. an increase (decrease) in the engine torque and power output has been shown. A need to perform tests related to the filtration properties of performance air cleaners has been indicated. A methodology of laboratory research has been developed for performance vehicle air cleaners. The results of the research on the filtration efficiency and accuracy characteristics have been presented along with the flow resistance of air filter elements/air cleaners depending on the dust absorbance coefficient k_m. The accuracy of the filter element has been evaluated following a Pamas particle counter measurement.

Key words: *combustion engine, air cleaner, efficiency and accuracy of filtration, filter element flow resistance, size of the dust grains*

1. Introduction

One of the factors influencing the engine repair intervals of modern combustion engines is the purity of the intake air. The said purity is ensured proper design of the air cleaner, the chemical and granulometric composition of the dust and its concentration in the intake air. The dust grains passing through to the engine penetrate the engine friction pairs damaging the structure of the mating pairs. The main friction assembly exposed to the destructive action of the dust is the piston-piston ring-cylinder assembly (P-PR-C). Following a premature wear of the said friction pair, a drop in the air tightness of the combustion chamber occurs leading to an increased blow-by to the crankcase, a reduction of the engine compression, hence a decrease in the engine power [4, 11, 20]. The most extensive engine wear is caused by grains of the size of 5–35 μm [1, 5, 6, 8, 26], which is why grains of the size exceeding 5 μm should be trapped by the air cleaners with a maximum (over 99.9%) efficiency [1, 3–5, 7, 17]. This job is performed by air filter elements with a paper filtering partition characterized by high density of packing and the dust absorbance limited by the admissible resistance Δp_{fdop}. Nanofibers are increasingly used in the production of the filtering partitions. Such nanofibers are obtained through electrospinning or meltblown [2, 13, 16, 19, 27].

With a steady value of the admissible resistance Δp_{fdop} the extension of the vehicle mileage can be obtained through the application of:

- Filter elements of greater filtering area,
- Materials of higher dust absorbance or lower initial flow resistance.

In recent years, fitting performance air cleaners in standard vehicles has become very popular. These air cleaners are mainly characterized by low flow resistance, and the possibility of multiple regeneration [28, 29]. From the available data [14, 15, 28, 29] we know that performance air cleaners replacing the OEM (Original Equipment Manufacturer) ones usually lead to an increase in the engine torque and power output as well as vehicle acceleration. According to [32], the efficiency of the filtration of performance air cleaners determined using the AC-coarse dust (d_{zmax} = 200 μm) reaches a value of 99.5–99.8% i.e. a value not much lower than that obtained for filters with a standard filtering partition measured with the AC-fine dust (d_{zmax} = = 80 μm). There are no data on the accuracy of filtration of performance air cleaners i.e. a parameter that, aside from the filtering efficiency, is the most decisive of the engine durability and its wear resistance.

The paper presents a methodology and results of reconnaissance research of performance air cleaners in terms of filtering efficiency and accuracy as well as flow resistance following the application of a PTC-D test dust (d_{zmax} = = 80 μm) – a local replacement dust for AC-fine according to the PN-ISO 5011 Polish standard [21].

2. The design of performance air cleaners

A performance air cleaner commonly denotes a non-standard air cleaner manufactured in a technology other than traditional paper filter elements. The filtering material is a multilayer cotton or cotton synthetic fiber soaked in a dedicated oily formula, which boosts the filtering efficiency. The layers of fibers are reinforced with a metal mesh on both sides to strengthen the construction – Fig. 1. The filtering component is pleated just like in the case of a traditional filter and then formed into the filtering element – Fig. 2. The design of the filtering layer allows its periodic regeneration consisting in cleaning with detergents and soaking it again in dedicated oil.

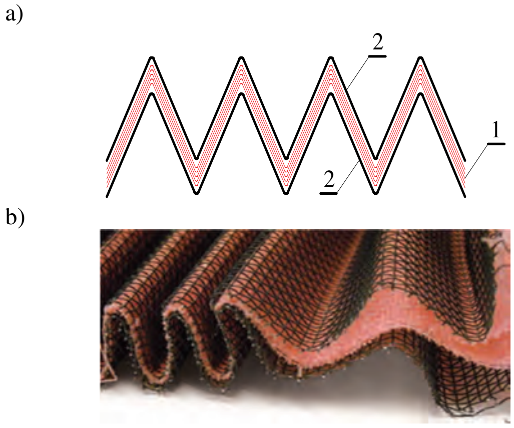

Fig. 1. The filtering layer of a performance air cleaner following the pleating procedure: 1 – fiber, 2 – protective mesh

Performance air cleaners are made in two versions:

- as a ring element (Fig. 2a) or a panel element (Fig. 2e) allowing its fitting into the original air cleaner replacing the OEM one,
- as filtering elements of a conical or cylindrical shape (Fig. 2b, 2c, 2d) fitted on an extended flexible pipe directly to the intake system following a removal of the original air cleaner.

Filters of performance vehicles are mostly shaped into cut cones or cylinders, usually with an inner cone (counter cone – confuser) – Fig. 2d. Performance filters with a counter cone have an increased filtering area, thus a more efficiently used space. The lack of the filter casing and the inflow of air directly from the surroundings reduce the flow resistance compared to standard solutions – Fig. 3.

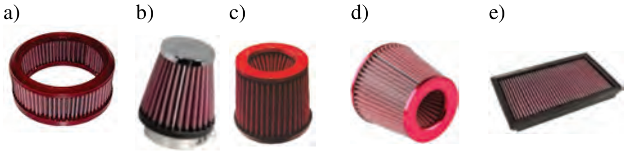

Fig. 2. Filter element: a) ring filter element, b) conical filter element, c) cylinder filter element with a counter cone, d) conical filter element with a counter cone, e) filtering panel [28, 29, 34]

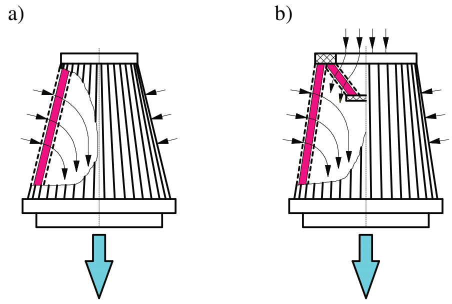

Fig. 3. Schematics of the airflow through a performance filter element: a) cone shaped, b) cone shaped with a counter-cone

Fitting of a performance filter element in the engine intake system causes the filter to suck in hot air from the engine compartment, which is why it is necessary to separate the filter from the engine with a special partition – Fig. 4.

Fig. 4. A performance air cleaner in a vehicle [33]

Fitting of a performance air filter element substituting the standard one results in a reduction of the flow resistance in the engine intake system. A significant reduction of the flow resistance is obtained when conical or cylindrical filters are fitted. The elimination of the air cleaner casing results in the air flowing directly from the surroundings over the entire area of the filter element not a narrow pipe in the case of an EOM solution. The conical filter element eliminates swirls inside the filter and directs the airflow.

Figure 5 presents (determined for the nominal airflow Q_{max}) the values of the flow resistance Δp_f of an OEM filter of a Subaru passenger car and the performance air filter elements (Fig. 6) fitted in the engine intake system. From the presented analysis we know that the conical filters (clean before operation) have their flow resistance levels lower by 60–75% compared with the OEM Subaru air cleaner.

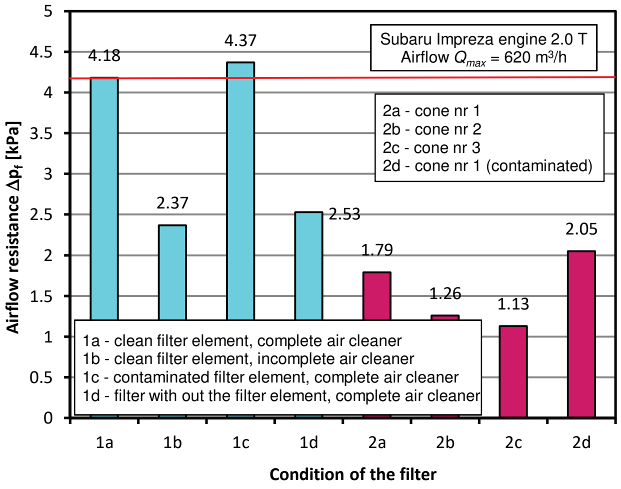

Fig. 5. Flow resistance Δp_f of an OEM air cleaner of Subaru and the performance air cleaners

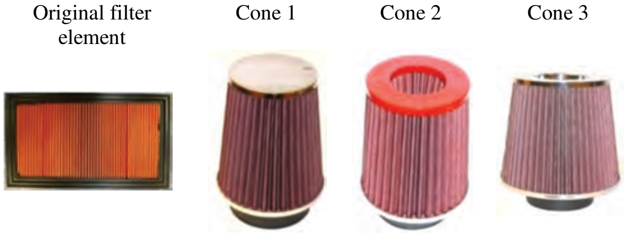

Fig. 6. Investigated filter elements of performance vehicles

3. The effects of fitting of a performance air cleaner in a passenger car

Fitting of a performance air cleaner in place of an OEM one usually brings measurable results such as the increase of power, torque and acceleration. This is confirmed by few experimental investigations of passenger car engines. Fig. 7 shows example results of these investigations performed on a 1.6 GTI Volkswagen Polo, where the original filter element was replaced with a performance one (BMC) [28]. An increment of power and torque were obtained on the level of 4.22% and 3.61% respectively.

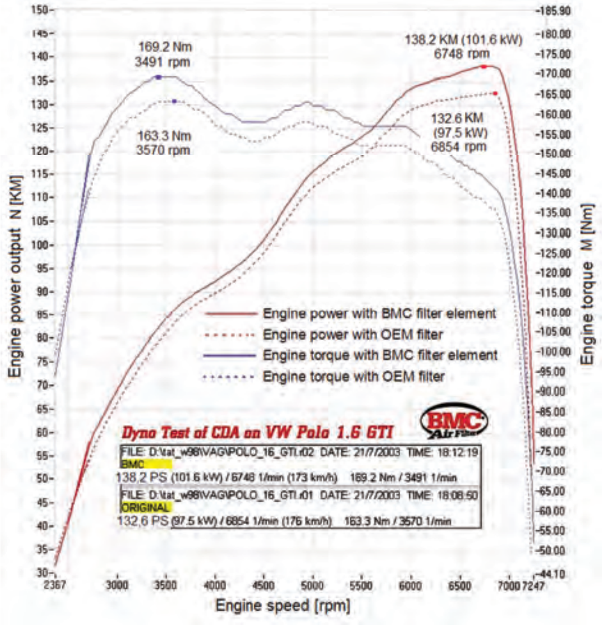

Fig. 7. Power output N = f(n) and torque M = f(n) characteristics of a 1.6 GTI Volkswagen Polo generated on a chassis dynamometer [28]

Table 1 presents the results of investigations performed on other vehicle engines whose OEM air cleaner was replaced with a BMC one. The percentage increment of the maximum power output N_{emax} and the maximum torque M_{omax} is different for each of the tested vehicles and falls in the range between 3.2–12.9% and 2.2–10.2% respectively. Besides, the increment of the engine torque is not proportional to the increment of power (Fig. 8).

The results of investigations, in which the OEM filter element of an Alfa Romeo 156 (but in two separate engines – spark ignition 2.0 TS and diesel 1.9 JTD Sportwagon) was replaced with a performance BMC filter an then with a conical BMC filter have been presented in Fig. 9. The investigations have shown an increase in the power output and a drop in the maximum torque.

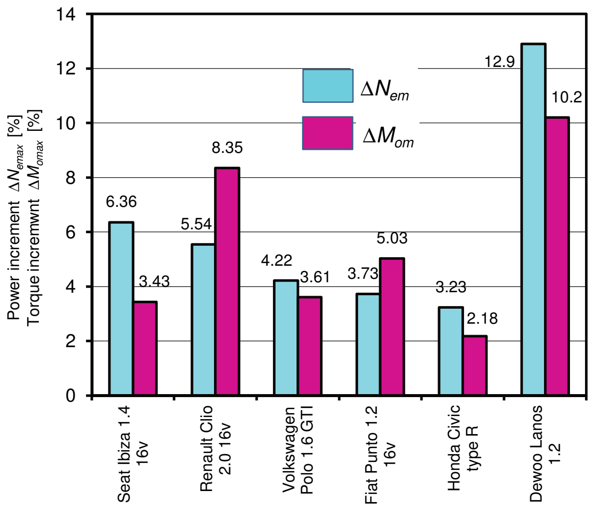

Fig. 8. Percentage increments in the power output N_{emax} and the maximum torque M_{omax} following an OEM filter replacement with a performance one

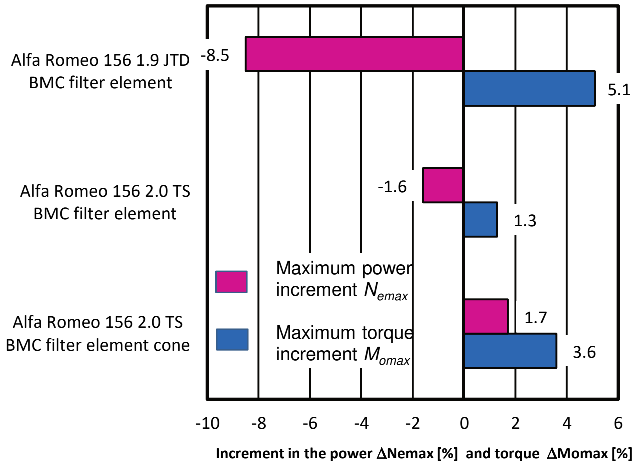

Fig. 9. Changes in the power output N_{emax} and torque M_{omax} of a 1.9 JTD Alfa Romeo 156 and 2.0 TS Sportwagon [14]

Table 1. Value of the maximum power output and the maximum torque for passenger vehicles fitted with a BMC CDA performance air cleaner [28–31]

No.	Vehicle make	Engine type	Power output N_{emax} with an OEM air cleaner [kW] / [KM]	Increment of engine maximum power output ΔN_{emax} [kW] / [%]	Engine torque M_{omax} fitted with an OEM air cleaner [Nm]	Increment of engine maximum torque ΔM_{omax} [Nm] / [%]
1	Seat Ibiza 1.4 16v	Spark ignition naturally aspirated	74.06 / 100.7	4.7 / 6.36	134.0	4.6 / 3.43
2	Renault Clio 2.0 16v	Spark ignition naturally aspirated	119.3 / 162.2	6.6 / 5.54	191.6	16.0 / 8.35
3	Volkswagen Polo 1.6 GTI	Spark ignition naturally aspirated	97.53 / 132.6	4.2 / 4.22	163.3	5.9 / 3.61
4	Fiat Punto 1.2 16v	Spark ignition turbo-charged	59.13 / 80.4	2.2 / 3.73	117.4	5.9 / 5.03
5	Honda Civic type R	Spark ignition naturally aspirated	139.3 / 189.4	4.5 / 3.23	192.9	4.2 / 2.18
6	Dewoo Lanos 1.2	Spark ignition naturally aspirated	49.35 / 67.1	6.4 / 12.9	79.3	8.1 / 10.2

In the case of the 1.9 JTD diesel engine, the increase in the power output is significant and amounts to 5.1% of the maximum power N_{emax}. In both engines, upon fitting of the BMC conical filter element the torque decreased. In the case of the Alfa Romeo 156 1.9 JTD engine, the drop in the maximum torque reaches as much as 8.5%. In the case of the conical filter element fitted directly on the intake manifold, the engine torque increased but only by 1.7%.

Upon replacement of the OEM filter with the performance one, a reduction of time t_a of the vehicle reaching the required speed (for both cars) was recorded. For Alfa Romeo fitted with the 1.9 JTD engine (Sportwagon), the time to reach the said speed from v = 0 to v = 120 km/h was reduced from t_a = 13.5 s to t_a = 12.7 s i.e. by 6%. For Alfa Romeo 156 2.0 TS Sportwagon, fitting the BMC conical filter element resulted in the reduction of this time from t_a = = 13.9 s to t_a = 13.6 s i.e. only by 1.5%. The obtained increments of the vehicle acceleration are rather small and may go unnoticed by the driver.

From the above analysis it results that the application of a filter element of lower flow resistance causes additional mass of air passing to the cylinders. Increasing the mass of air in the cylinder forces an increased mass of fuel in order to keep the stoichiometric nature of the mixture. As a result, the engine power output increases, but, as we know from the performed analysis, it is not the case for all engines that had the filters replaced. The intake system of modern vehicles is designed to ensure maximum power outputs. The diameters and lengths of the intake and exhaust ducts as well as the air cleaners are selected to obtain a dynamic engine boost relying on the wave phenomena. It consists in generating resonance between the pressure shockwaves and the frequency of the vibrations of the gas inside the intake duct. A characteristic feature of this form of boosting is the fact that the resonance occurs in a narrow range of engine speeds, usually the engine speed of the maximum torque n_M [25]. Any parameter-related interference with such a precisely composed intake system (changing the air cleaner, changing the length of the intake duct) may lead to a fading effect of the resonance boosting, hence a shift of the maximum torque towards different engine speeds. The effect is that the replacement of the original filter element with a performance one, aside from generating a small increase in the power output and torque, does not bring measurable results (vehicle acceleration).

Performance engines are designed to reach maximum power outputs at high engine speeds n_N, reaching 11000 rpm. It makes much sense to apply performance filter elements in such engines as these filters are characterized by low flow resistance at high airflows. Engines of passenger vehicles are designed to operate at lower engine speeds n_N, not exceeding 6000 rpm.

From the above data we do not know how the fuel consumption changes after OEM to performance filter replacement. An increased mass of fuel mixed with the increased mass of air results in an increase in the hourly fuel consumption in order to keep the stoichiometric regime. The data related to fuel consumption are intentionally omitted by the manufacturers of performance filters for obvious reasons. The available data do not contain values of the filtration accuracy of the base material, let alone the value of the flow resistance of the OEM and the performance filters. This obstructs a full analysis of the impact of a performance filter on the engine parameters in a passenger car. Such data are well available for filtration papers predominantly used in filtration of vehicle consumable fluids.

It is, thus, necessary to carry out experimental investigations of the performance filter elements in terms of their efficiency, filtration accuracy and flow resistance, which would allow assessing their applicability as replacement components in passenger vehicles.

4. Aim and subject of the research

The aim of the research was to determine the filtration properties of a performance air cleaner and a paper filter element through the obtainment the following characteristics:

- Filtration efficiency $\varphi_f = f(k_{mj})$ and flow resistance $\Delta p_f = f(k_{mj})$ as a function of coefficient of absorbance k_{mj} of the filtration material,
- Dust granulometric composition downstream of the filter,
- Filtration accuracy $d_{zmax} = f(k_{mj})$ – the size of the maximum dust grains in the air downstream of the filter as a function of coefficient of dust absorbance k_m

where: k_{mj} – coefficient of absorbance determining the mass of dust m_{ZFj} trapped per 1 m^2 of active surface A_{cz} of the filtration material until the end of a j-th measurement cycle expressed with a relation:

$$k_{mj} = \frac{\sum_{j=1}^{n} m_{ZFj}}{A_{cz}} \; [g/m^2] \tag{1}$$

The objects of the investigations were K&N performance air cleaners in the shape of a cut cone and a paper filter element (Fig. 10).

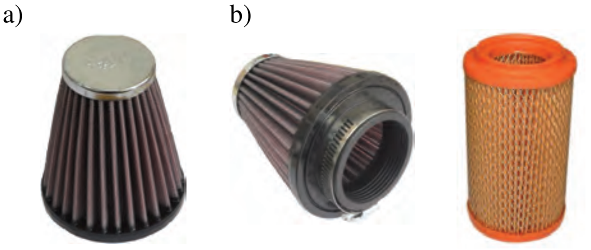

Fig. 10. Investigated air cleaners; a) performance air cleaner by K&N, b) AP 019 air filter element

The filtration material in the performance air cleaner is a natural-synthetic fiber formed in layers and reinforced with a metal mesh on the inflow and outflow sides. The filtration material has 28 pleats of the height of h = 15 mm, which ensures an active surface area of the filtration material of $A_{cz} = 0.0452\ m^2$.

The investigated performance air cleaner was applied in a $V_{ss} = 0.9\ dm^3$ engine of a sports car – Seicento Citymatic. The airflow passing through the filter calculated from the air demand of the engine was determined according to the principles and relations presented in [21, 22]. At n_{min} = = 1000 rpm and the engine speed of the maximum power output n_N = 5500 rpm, it assumes the following values respectively: $Q_{min} = 25\ m^3/h$ and $Q_N = 135\ m^3/h$.

The filtration rate υ_F of the investigated performance air cleaner of the surface area of the filtration material A_{cz} = = 0.0452 m² calculated from the relation below assumes values in the range υ_F = 0.156–0.829 m/s.

$$\upsilon_F = \frac{Q_{min,(max)}}{3600 \cdot A_{cz}} \; [m/s] \tag{2}$$

The cylindrical filter element (AP 019) fitted in Fiat 126p was made from J.C. BINZER 796/1 VH 186 filtration paper of the surface area A_{cz} = 0.148 m².

The investigations of performance air cleaners were carried out in three stages. In the first stage characteristics were determined for three new performance air cleaners each operating at different filtration rates:

- $\upsilon_{F1} = 0.16$ m/s,
- $\upsilon_{F2} = 0.32$ m/s,
- $\upsilon_{F3} = 0.48$ m/s.

In the second stage, characteristics of a filter regenerated in detergents after the first trial were determined. Upon drying and moisturizing, the characteristics of this filter at the filtration rate of $\upsilon_{F2R} = 0.32$ m/s were determined.

The third stage consisted in determining of the characteristics of a paper filter element of the filtration rate $\upsilon_{Fp} = 0.08$ m/s. For the filtration papers, the maximum rate should not exceed $\upsilon_{Fmax} = 0.07–0.12$ m/s [1, 5, 10, 23, 24].

5. Research methodology and conditions

The investigations were carried out on a typical flow test stand (Fig. 11) allowing determination of the fundamental characteristics: efficiency, filtration accuracy and airflow resistance for standard air filter elements of passenger cars within the airflow range 40–300 m^3/h and dust concentration up to 2 g/m^3.

The test stand was equipped with a particle counter (Pamas – 2132 with a HCB-LD-2A-2000-1 sensor) recording the number and size of the particles in the mass flow Q (downstream of the filter) of the range 0.7–100 µm in i = 32 measurement intervals constituting ranges limited by the diameters (d_{zimin}–d_{zimax}). The test dust was dispensed to the dust chamber where it mixed with the intake air subsequently sucked in by the investigated air cleaner.

At an appropriate distance downstream of the investigated filter a measurement probe was placed centrally in the axis of the duct that uptakes the air to the Pamas – 2132 particle counter. The measurement duct ends with a special filter protecting the rotameter from the dust.

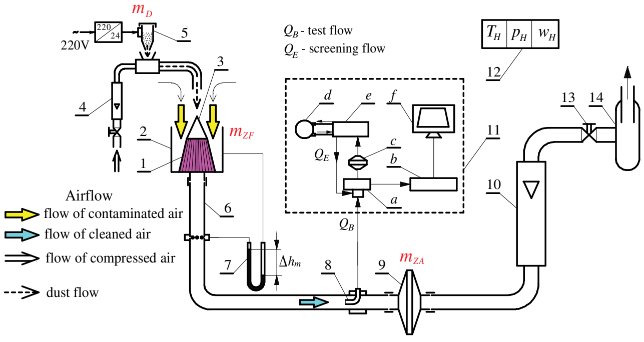

Fig. 11. Functional schematics of the filter test stand: 1 – filter, 2 – dust chamber, 3 – protective cone, 4 – rotameter, 5 – dust dispenser, 6 – measurement duct, 7 –U-type pipe manometer, 8 – measurement probe, 9 – absolute filter, 10 – rotameter, 11 – Pamas particle counter (a – sensor, b – microprocessor, c – test flow filter, d – vacuum pump, e – flow control block, f – readout panel), 12 – micromanometer, 12 – pressure, humidity and ambient temperature measurement set, 13 – airflow adjustment valve, 14 – suction fan

During the tests, a research cycle was applied, in which five counts of the dust grains in the range 0.7–50 µm were programmed, divided into 28 identical measurement intervals limited with diameters (d_{zimin}–d_{zimax}) with a step of Δd_{zi} = 0.4 µm (0.7–1.1 µm; 1.1–1.5 µm; 1.5–1.9 µm; …; 11.5–11.9 µm) and four intervals of diameter measurement (d_{zimin}–d_{zimax}) 11.9–17.9 µm, 17.9–25 µm, 25–42 µm and 42–50 µm respectively.

The tests were performed in measurement cycles resulting from time t_p of even dust dispense to the filter. During the measurement cycle at a moment $t_z = ½\, t_p$, the procedure of counting of the particle number and measurement of its size was initiated in the counter downstream of the filter.

After each j-th measurement cycle the following were determined:

1. Flow resistance Δp_{fj} of the filter was determined as a drop in the static pressure upstream and downstream of the filter based on the measured (upon completion of the dust dispense) height Δh_{mj} on the water manometer (U-pipe) utilizing the relation:

$$\Delta p_{fj} = \frac{\Delta h_{mj}}{1000}(\rho_m - \rho_H)g \quad [\text{Pa}] \tag{3}$$

where: ρ_m – manometer fluid density (H_2O) at the measurement temperature, t_H, ρ_H – density of the atmospheric air, g – local gravitational acceleration.

2. The calculated value of the flow resistance Δp_{fj} was converted to normal conditions (T_n = 293K i p_n = 1013 kPa) using [22]:

$$\Delta p_{fnj} = \frac{p_H}{1013} \cdot \frac{293}{T_H} \cdot \Delta p_f \quad [\text{kPa}] \tag{4}$$

where: t_H, p_H – average temperature and pressure during the tests.

3. The efficiency of filtration (as per [21]) – as a quotient of the mass of the dust m_{ZFj} trapped by the filter and the mass of the dust m_{Dj} introduced into the filter during the subsequent j-th measurement cycle based on the relation:

$$\varphi_{fj} = \frac{m_{ZFj}}{m_{Dj}} 100\% \tag{5}$$

4. Coefficient of absorbance k_{mj} of the investigated filtration material:

$$k_{mj} = \frac{\sum_{j=1}^{n} m_{ZFj}}{A_{cz}} \quad [\text{g/m}^2] \tag{6}$$

5. The number N_{zi} of the dust grains in the airflow downstream of the filter (passed through by the filtering material) in the measurement intervals limited with diameters (d_{zimin}–d_{zimax}).

6. The accuracy of filtration – as the greatest size of the dust grain $d_{zj} = d_{zmax}$ in the airflow downstream of the filter.

7. Percentage share of individual dust grain fractions in the air downstream of the filter for a given test cycle:

$$U_{zi} = \frac{N_{zi}}{N_z} = \frac{N_{zi}}{\sum_{i=1}^{32} N_{zi}} 100\% \tag{7}$$

where: $N_z = \sum_{i=1}^{32} N_{zi}$ – total number of dust grains passed through by the filter (from all measurement intervals) in the test cycle.

According to the PN-ISO 5011 standard [21], the dust concentration in the intake air was assumed at s = 0.5 g/m^3.

The actual dust concentration was determined each time upon completion of the test cycle. For the tests, PTC-D test dust was applied whose chemical and granulometric composition has been given in [21, 22].

6. Analysis of the results

The results of the investigations and the calculations of the efficiency φ_f and accuracy d_{zmax} of filtration as well as the flow resistance Δp_f of the investigated air cleaners have been presented in Fig. 12. As the mass of the trapped dust in the filtration layer grows (increase in the k_m coefficient) the efficiency and accuracy of filtration and the flow resistance assume increasingly higher values. This is a result of filling of the inter-fiber spaces (pores) with dust, which is in agreement with the literature knowledge [7, 9, 17, 18].

The operation of the performance filters, whose characteristics have been presented in Fig. 12, can be divided into two stages. The first (initial) stage of the filter operation (I) is characterized by low efficiency and accuracy of filtration as well as low flow resistance. The higher the filtration rate the higher the efficiency of the filtration. After the first test cycle, the filtration efficiency for $\upsilon_{F1} = 0.16$ m/s, $\upsilon_{F2} = 0.32$ m/s and $\upsilon_{F3} = 0.48$ m/s assumes the values $\varphi_{f1} = 46.6\%$ $\varphi_{f2} = 61.4\%$ and $\varphi_{f3} = 86.1\%$ respectively. During this time, the particles deposit on the elements of the porous structure (on the surface of the fibers). The condition for the particle deposition from the fluid flow on the surface of the fiber is the following relation [17]:

$$F_b + F_p + F_t + F_c < F_s + F_o \qquad (8)$$

where: F_b – inertia force of the particle, F_p – adhesion force of the particle to the surface, F_t – friction force, F_c – gravity force, F_s – force of elastic collision, F_o – resistance force.

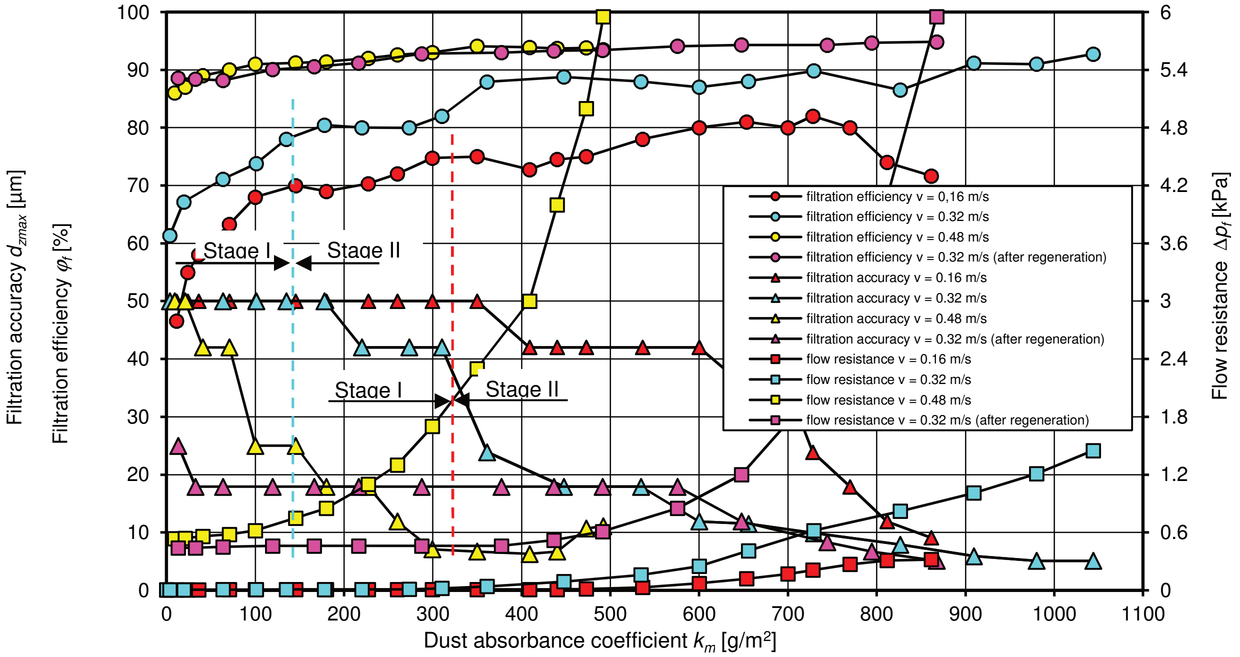

Fig. 12. Characteristics of efficiency φf , accuracy of filtration d_{zmax} and flow resistance Δp_f depending on the dust absorbance coefficient k_m of the investigated performance air cleaners

It was assumed that the first (I) stage of the filter operation lasts until the increase in the filtering accuracy, i.e. a clear drop in the maximum size of the grains d_{zmax} in the air downstream of the filter. For filter 1 (tested at $\upsilon_{F1} = 0.16$ m/s), this period lasts until the coefficient of dust absorbance reaches $k_{m1} = 350$ g/m^2. At this time the maximum size of the grains d_{zmax} maintains the level of $d_{zmax1} = 50$ µm, the filtration efficiency increases from $\varphi_{f1} = 46.6\%$ to $\varphi_{f1} = 75\%$ and the flow resistance changes only slightly from $\Delta p_{f1} = 0.0051$ kPa to $\Delta p_{f1} = 0.0085$ kPa. For higher filtration rates the initial stage is shorter. For filter 2 (tested at the rate of $\upsilon_{F2} = 0.32$ m/s), the first stage ends as the coefficient of absorbance reaches $k_{m2} = 178$ g/m^2. For filter 3 ($\upsilon_{F3} = 0.48$ m/s), the first stage of the filtration process is very short ($k_{m3} = 21$ g/m^2) and a clear drop in the maximum size of the grains d_{zmax} downstream of the filter can be observed.

The second stage (II) of the filter operation is characterized by a further growth in the filtration efficiency, but it is less intense compared to the first stage. The first particles deposited on the porous structure form a layer that serves as another porous structure for the subsequent particles flowing with the intake air. Agglomerates form growing significantly filling the spaces between the fibers – Fig. 13 [12].

The formation of a layer of dust around the filtration components results in a modification of the gas flow conditions and a separation of subsequent inflowing dust grains. The distances among the fragments surrounded by the dust get smaller (porosity of the filtration material is reduced), which results in an increase in the flow velocity, hence increasing the hydrodynamic flow resistance in the filtration layer along with the filtering capability of the layer. The rate of formation of the agglomerates and their size mainly depend on the density of the filtering partition and the aerosol flow rate υ_F.

The filter tested at υ_{F1} = 0.16 m/s reached a maximum value of efficiency φ_{fmax1} = 82% at k_{m1} = 862 g/m^2 and then an abrupt drop occurred to φ_{f1} = 71.6 %. This phenomenon was accompanied by a drop in the filtration accuracy– increase in the maximum size of the grains d_{zmax}. The phenomenon of the efficiency drop may have been caused by the fact that the detaching forces (vacuum) exceeded the adhesion forces of the grains to the surface. An avalanche detachment of the grains took place and the grains subsequently moved further inside or were grabbed by the outlet air from the filter. As a result, the filter partly lost its properties. For this reason as well as due to the falling of the dust particles previously trapped in the filter upon completion of the measurement cycle, the tests were terminated.

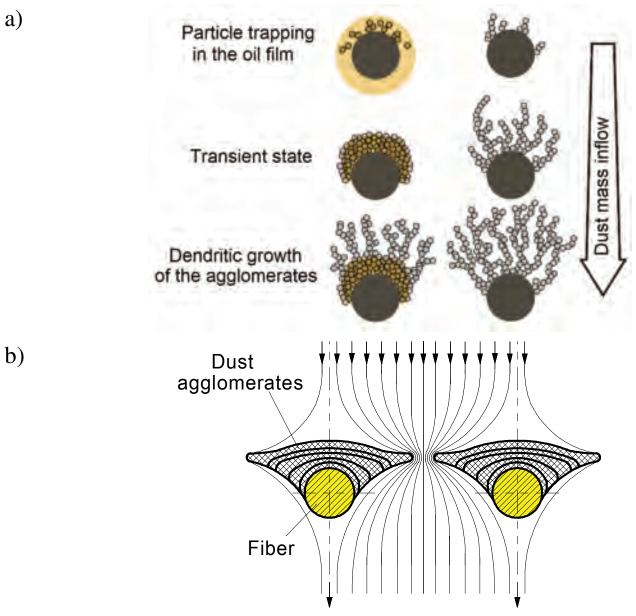

Fig. 13. Schematics of the agglomerates formation: a) subsequent phases of particle trapping in a fiber moisturized with oil and a dry one [12], b) flow of aerosol between the fibers covered with dust agglomerates

The higher the filtration rate the higher the efficiencies of the investigated filters in the entire operating range. The filter tested at υ_{F2} = 0.32 m/s reached a maximum value of efficiency φ_{fmax2} = 92.7% (k_{m2max} = 1044 g/m^2) and for the filter tested at υ_{F3} = 0.48 m/s the maximum value of filter efficiency was φ_{fmax3} = 93.8% (k_{m3max} = 493 g/m^2). At the same time, the dust grains d_{zmax} assumed increasingly lower values. At the final (II) stage, filter 1 reached a value d_{zmax1} = = 9.1 µm, filter 2 d_{zmax2} = 5.5 µm and filter 3 d_{zmax3} = 5.1 µm.

With the increase of the dust trapped in the filtration layer (increased coefficient k_m) a continuous increase in the resistance Δp_f takes place, only the intensity of the growth at the second stage of the filter operation is much higher. Besides, the flow resistance and the intensity of the growth is higher when the filtration rate increases. In the final stage of the second operating period the filters usually reach flow resistance values several times higher than the initial one (Δp_{f0}) of a given filter. For filter 1 tested at υ_{F1} = 0.16 m/s, the flow resistance assumes a value Δp_{f1} = 0.21 kPa at k_{m1} = = 728 g/m^2. For the same value of coefficient k_m, the filter tested at υ_{F2} = 0.32 m/s reaches a flow resistance Δp_{f2} = = 1.45 kPa. The conical filter operating at υ_{F3} = 0.48 m/s reaches Δp_{f3} = 3 kPa already at k_{m3} = 408 g/m^2. This results from the increase in the mass of the dust trapped in the filtration layer. The forming and significantly growing agglomerates fill the spaces between the fibers. A smaller distance between the surfaces of the filtering structures covered with dust results in the increase of the flow rate, hence the increased resistance Δp_f whose value is the function of the square of the filtration rate.

Out of the three investigated performance filters, filter 2 (υ_{F2} = 0.32 m/s) had the highest dust absorbance coefficient k_{m2max} = 1043.8 g/m^2 – almost twice as high compared to filter 1 (υ_{F1} = 0.16 m/s) and four times higher than filter 3, not exceeding the admissible flow resistance Δp_{fdop} = 3 kPa.

The efficiencyφ_f and the accuracy d_{zmax} of filtration and the flow resistance Δp_f are different for each filter and depend on the structure of the filtration layer, dust concentration in the air, dust grain size and flow rate through the filter. In the case of the investigated filters, the changes in the efficiency φ_f and accuracy d_{zmax} of filtration as well as the flow resistance depend on the airflow rate through the filter (filtration rate). As the filtration rate grows in the range υ_F = 0.16– –0.48 m/s, the efficiency of filtration and flow resistance assume increasingly higher values. The highest dust absorbance coefficient k_{m2max} = 1043.8 g/m^2 was obtained for filter 2 tested at the filtration rate υ_{F2} = 0.32 m/s.

The explanation of this phenomenon is not easy because the process of aerosol filtration has a stochastic nature difficult to describe quantitatively and qualitatively. Trapping of the particles in the porous partition is a process depending on many forces and phenomena. The particles of contaminants and the elements of the porous structure have an irregular shape and microstructure. The grains of dust deposit evenly on the surfaces of the fibers. The porosity of the partition decreases and detachment of already deposited grains may follow under the pressure of the flowing fluid.

At low filtration rates (υ_{F1} = 0.16 m/s), the dust grains have little kinetic energy and it is much more difficult for them to penetrate inside the filtration material structure. They deposit mainly on the surfaces of the fibers located near the intake side of the partition. Since the filtration layer is moist, the intensity of the grain trapping increases. Only single grains penetrate inside the partition. As more grains arrive, they deposit on the previously trapped ones. The growing agglomerates fill the spaces between the fibers leading to the trapping of the grains on the surface of the material and blocking them from penetrating inside the filtration material. The further filtration space is not used, which results in a lower dust absorbance coefficient k_m (Fig. 14).

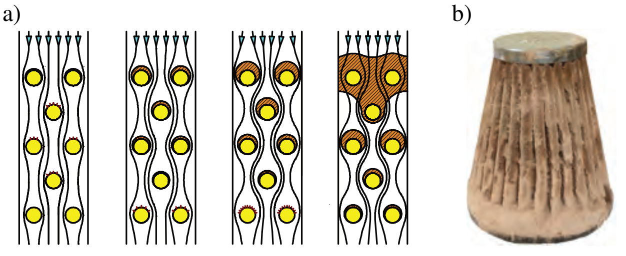

Fig. 14. Deposition of dust on the filtration material during aerosol flow at low speeds: a) change in the structure of the filtration material, b) performance filter after the tests

In such a situation, the detaching forces (vacuum) may exceed the adhesion forces of the grains to the fibers. A grain detachment phenomenon may take place and its displacement towards the inside of the filtration structure that still has spaces free from dust. In this part of the filtration structure, the filtration process continues as at the initial stage of filtration, i.e. with lower efficiency.

At high filtration rates (υ_{F3} = 0.48 m/s) the dust grains have greater kinetic energy, which is why they move inside the partition and deposit mainly on the surface of the fibers located near the outlet part of the partition. As more grains arrive in this area, agglomerates form growing significantly and blocking the flow of air. This is the reason for the abrupt increase in the flow resistance at υ_{F3} = 0.48 m/s. In this case, the filtration layer is not fully utilized. The filter reaches a value k_{m3} = 408 g/m^2 already at Δp_{f3} = 3 kPa.

From the above analysis, it results that the process of filtration in the filter structure is most effective (optimum) when the entire filtration space is used, the sign of which is the highest value of the dust absorbance coefficient k_m. Besides, the value of the flow resistance should not exceed the admissible one and the filtration efficiency should remain on a constant, high level. In the outlet air, dust grains of great size d_{zmax} (indicating grain detachment from the structure due to high flow rates) do not appear. From the investigations it results that such conditions were fulfilled during the tests on the performance filter at the filtration rate υ_{F2} = 0.32 m/s.

For this filtration rate, the characteristics were determined for the filter that was subjected to regeneration (detergents) after the first stage of the tests. Upon drying and moisturizing with mineral engine oil (for lack of the original moisturizer), tests on this filter were performed according to the methodology applied thus far.

The initial flow resistance of the original filter tested at υ_{F2} = 0.32 m/s has a value of Δp_{f3} = 0.0051 kPa. The filter after regeneration and soaking in the engine oil reaches a value of Δp_{f3p} = 0.44 kPa i.e. much higher than that of the original filter. This most likely results from the higher engine oil viscosity (compared with the original moisturizer) that soaks in the filter structure. As the mass of the dust trapped in the filter grows (increased coefficient k_m), the efficiency φ_f and accuracy d_{zmax} of filtration and the flow resistance Δp_f of the performance filter assume higher values, yet, the higher levels of these parameters were not observed in the case of the original filter. An improvement of the filtration properties is particularly conspicuous during the initial period of the filter operation. The efficiency of filtration increases from φ_{fmax2} = 61.8% (original filter) to 88.5% (regenerated filter) and the maximum size of the grains d_{zmax} in the air downstream of the filter assumes values more than 60% lower than those of the original filter and remains on the level of d_{zmax1} = 17.9 µm.

The number of the dust grains in the air downstream of the tested filter, passing through the filtering structure was recorded with the Pamas 2132 particle counter in preset measurement intervals and the results have been shown in Figs 16–18.

For each measurement cycle, along the increase in the dust grain size, their number in the air downstream of the filter decreases. In the last measurement interval of each measurement cycle there is usually one dust grain of the maximum size of d_{zmax}. The size of this grain was assumed as a criterion of assessment of the performance filter accuracy (Fig. 15).

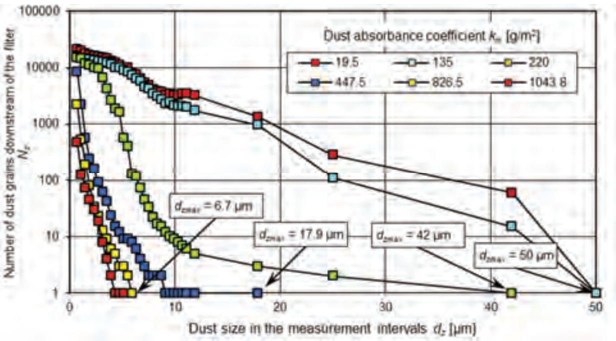

Fig. 15. Total number of dust grains in the air downstream of the performance filter during the tests at the filtration rate υ_{F2} = 0.32 m/s

In subsequent measurement cycles, as the time of the performance filter operation elapsed, the total number of dust grains passed through the filter decreased and their maximum size d_{zmax} was increasingly smaller. During the measurement cycle 2 (the dust absorbance coefficient k_m = = 19.5 g/m^2) in the cleaned air, there were dust grains of the size not exceeding d_{zmax} = 50 µm (Fig. 15). During the measurement cycle 7 (k_m = 220 g/m^2) in the air downstream of the filter, dust grains of the maximum size of d_{zmax} = = 42 µm were recorded and during the last measurement there were dust grains not exceeding d_{zmax} = 5.1 µm.

In the subsequent measurement cycles, the total number of dust grains in the air downstream of the filter decreased but not identically for all grain sizes. Along with the coefficient of dust absorbance k_m (the time of filter operation) systematically grew the number of the dust grains of small size (0.7–1.1 µm) (Fig. 16). Their share U_p in the total number of grains for k_m = 19.5 g/m^2 had the value U_p = = 7.6% and in the last measurement (k_m = 1043.8 g/m^2) the share amounted to U_p = 68%. The number of the dust grains of the size (1.1–1.5 µm) grew until U_p = 29.6% and then decreased. For the dust grains exceeding d_z = 1.5 µm, one may observe a decrease in the number of the dust grains, which indicates that it is these grains that were trapped in the filtering partition.

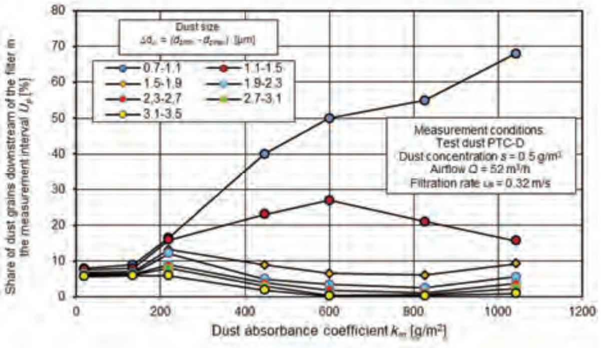

Fig. 16. Share of the dust grains in the air downstream of the performance filter during the tests at the filtration rate of υ_{F2} = 0.32 m/for preset measurement intervals (d_{zimin} – d_{zimax})

The granulometric composition of the dust upstream and downstream of the performance filter for the filtration rateυ_{F2} = 0.32 m/s has been shown in Fig. 17. For example, the share of the dust grains of the size 3.9–4.3 µm in the total number of test dust grains in the air upstream of the filter is U_p = 16.2%. In the air downstream of the filter, the share of the grains of these sizes is U_p = 4.9% for the dust absorbance coefficient k_m = 19.5 g/m^2 and U_p = 0.25% for k_m = 1043.8 g/m^2.

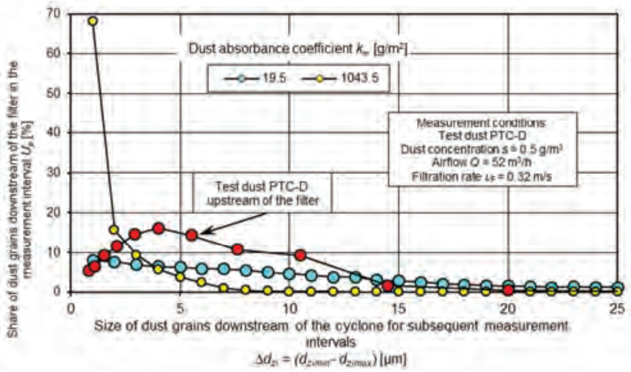

Fig. 17. Granulometric composition of dust in the air upstream and downstream of the performance filter during the tests at the filtration rate υ_{F2} = = 0.32 m/s and k_m = 19.5 g/m^2 and k_m = 1043.8 g/m^2

The results of research on the efficiency φ_f and accuracy d_{zmax} of filtration as well as the flow resistance Δp_f of the investigated performance filters and the filtration paper element have been shown in figure 18. The filter element is characterized by a better curve of the efficiency and accuracy characteristics. Performance air cleaners reach values of efficiency and accuracy that are much lower compared to the paper filter elements (Fig. 18).

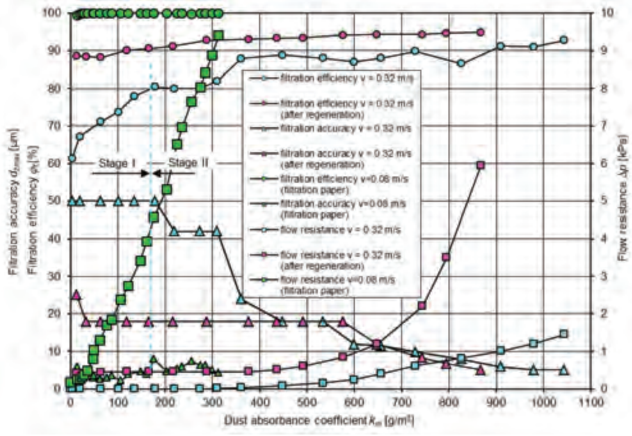

Fig. 18. Filtration efficiency φ_f, accuracy d_{zmax} and flow resistance Δp_f depending on the dust absorbance coefficient k_m of the investigated performance air cleaner and the filtration paper

The efficiency of filtration of a paper filter element already at its initial period of operation exceeds 99%. At this time performance air cleaners reach their efficiency on the level of φ_f = 46.6%÷86%. In the further periods of the paper filter element operation, the efficiency remains on the level of 99.9%. In the initial period of the paper filter element operation the maximum size of the dust grains in the cleaned air does not exceed d_{zmax} = 5.9 µm and quickly stabilizes at d_{zmax} = 2.3–3.9 µm. For performance air cleaners, the maximum size of the dust grains in the initial period does not exceed d_{zmax} = 50 µm and then slowly moves towards d_{zmax} = 5.1–5.9 µm. Such a size of the dust grains in the cleaned air is obtained by performance filters in the last, short period of their operation.

The main period of operation of a performance filter is characterized by the presence in the cleaned air of dust grains of the size in the range d_{zmax} = 20–50 µm, i.e. very hazardous to the engine friction pairs. This may lead to premature wear of such pairs, a drop in the power output and a reduction in the engine durability. From the performed investigations it results that a performance air cleaner does not ensure the required efficiency (99.5%) and filtration accuracy (5 µm) of the intake air. Therefore, it should not be applied to clean intake air in passenger vehicles.

Conclusions

1) For cleaning intake air in performance cars, air cleaners commonly referred to as performance air cleaners are applied. These are cleaners of different shapes: panel, cylindrical (fitting the original casing) or conical (with the casing removed). The filtration material used in these filters is natural-synthetic fiber of a loose structure ensuring low flow resistance. The available data related to performance filters do not contain information on the basic filtration parameters such as filtration efficiency and accuracy.
2) Performance filters are used by many drivers. They are used as filter elements fitting the original casing and as independent cleaners (conical, cylindrical) fitted directly to the intake manifold replacing the original air cleaner. As a result, an increase in the power output is obtained (up to 13%) as well as an increase in the maximum torque. In some engines, though, a drop in the power output and torque is observed. This is most likely caused by the reduced dynamic charging due to the modification of design of the original intake system.
3) For a steady filtration rate, as the mass of the dust m_{ZF} trapped in the performance filter (increased coefficient of absorbance k_m) grows, a slow increase in the efficiency and accuracy of filtration as well as flow resistance follows. As the filtration rate grows, the filtration efficiency assumes higher values, the flow resistance increases and the maximum size of the dust grains passed through is getting smaller. Such a change in the parameters of a performance filter results from the changes in the structure of the filtration material as the dust grains deposit on the surface of the fibers forming agglomerates.
4) In the initial period of the filter operation, performance filters are characterized by low efficiency (φ_f = 46.6%–86%), accuracy (d_{zmax} = 20–50 µm) and flow resistance. They have higher initial resistance. The presence of such large dust grains in the cleaned air may result in premature wear of the piston-piston ring-piston sleeve assembly. This is one of the main reasons for a drop in the engine compression and power output.

5) Performance filters reach their maximum efficiency and accuracy only in the last period of operation assuming the values φ_f = 82.1–92.7% and d_{zmax} = 5.9–17.9 μm. These values are lower than those obtained by paper filter elements (efficiency φ_f = 99.5–99.9% and accuracy d_{zmax} = 2.9–5.1 μm) in the entire range of their operation. This results from the loose structure of the filtering material of the performance air cleaners. The paper filter element, due to tighter structure packing, has a better curve of the efficiency and accuracy characteristics.
6) The characteristics of accuracy and efficiency of performance filters after regeneration have a better curve than the original performance filters. Increased efficiency and accuracy of filtration as well as flow resistance was obtained upon soaking of the filtering material in the engine oil that has higher viscosity than the original moisturizer. Regeneration of performance filters (soaked in engine oil) by using detergents is impossible.
7) Performance air cleaners, due to their low values of efficiency and accuracy of filtration, should not be used to clean intake air in passenger vehicles, as it may result in premature wear of the engine parts. The initially obtained increase in the power output resulting from the reduced flow resistance may be quickly compensated by a drop in the power output resulting from excess engine wear.

Bibliography

[1] BACZEWSKI, K., HEBDA, M. Filtracja płynów eksploatacyjnych (Filtration of operating fluids). *MCNEMT*. Radom 1992.

[2] BUCHER, T.M., TAFRESHI, H.V., TEPPER, G.C., Modeling performance of thinfibrous coatings with orthogonally layered nanofibers for improved aerosol filtration. *Powder Technology*. 2013, **249**, 43-53.

[3] CHŁOPEK, Z. Testing of hazards to the environment caused by particulate matter during use of vehicles. *Eksploatacja i Niezawodność – Maintenance and Reliability*. 2012, **2**, 160-170.

[4] Diesel Engine Air Filtration. PALL Corporation. 2004.

[5] DURST, M., KLEIN, G., MOSER, N. Filtration in Fahrzeugen. *Die Bibliothek der Technik*, Niemcy 2005.

[6] DZIUBAK, T. Operating fluids contaminantions and their effect on the wear of elements of a motor vehicle's combustion engine. *The Archives of Automotive Engineering – Archiwum motoryzacji*. 2016, **72**(2), 43-72.

[7] DZIUBAK, T., SZWEDKOWICZ, S. Experimental research on filtering fibers in a cyclone–porous barrier system. *Combustion Engines*. 2014, **158**(3), 45-55.

[8] DZIUBAK, T. The assessment of the possibilities of improvement of the extraction evenness in multicyclone dedusters fitted in special vehicles. *Combustion Engines*. 2012, **4**, 34-42.

[9] DZIUBAK, T. Methodology of research of filter paper characteristics to air filter of vehicle exploited at large air dustiness conditions. *ZEM PAN*. 2003, **4**(136), 101-117.

[10] ERDMANNSDÖRFER, H. Lesttingmoglichkeiten von Papierfiltern zur Reinigung der Ansaugluft von Diselmotoren. *MTZ*. 1971, **32**(4), 123-131.

[11] FITCH, J. Clean oil reduces engine fuel consumption. *Practicing Oil Analysis Magazine*. 2002, **11**-**12**.

[12] MULLER, T.K., MEYER, J., THEBAULT, E. et al. Dust capacity increase of air filters by oil pre-treatment. *Aerosol Technology*. 2014.

[13] GRAFE, T., GOGINS, M., BARRIS, M. et al. Nanofibers in filtration applications in transportation. *Filtration 2001 International Conference and Exposition*. Chicago, Illinois, December 3-5, 2001.

[14] GT. Tuning, car audio, samochody sportowe. 2002, 3.

[15] GT. Tuning, car audio, samochody sportowe. 2002, 45.

[16] HEIKKILÄ, P., SIPILÄ, A., PELTOLA, M. et al. Electrospun PA-66 Coating on Textile Surfaces. *Textile Research Journal*. 2007, 77(11), 864-870.

[17] JAROSZCZYK, T., FALLON, S.L., DORGAN, J.E. et al. Development of high dust capacity multi-media engine air filters. *Fluid/Particle Separation Journal*. 2003, **15**(2), 57-65.

[18] JAROSZCZYK, T., FALLON, S.L., PARDUE, B.A. Analysis of engine air cleaner efficiency for different size dust distributions. *Fluid/Particle Separation Journal*. 2002, **14**(2), 75-88.

[19] JAROSZCZYK, T., PARDUE, B.A., HECKEL, S.P. et al. Engine air cleaner filtration performance – theoretical and experimental background of testing. *AFS Fourteenth Annual Technical Conference and Exposition*, May 1, 2001, Tampa, Florida Included in the Conference Proceedings (Session 16).

[20] KOSZAŁKA, G., SUCHECKI, A. Changes in performance and wear of small diesel engine during durability test. *Combustion Engines*. 2015, **3**, 34-40.

[21] PN-ISO 5011. Filtry powietrza do silników spalinowych i sprężarek. Badanie działania. PKNM, 1994.

[22] PN-S-34040, Filtry powietrza. Wymagania i badania. PKN, 1996.

[23] SCHULZE, M., TAUFKIRCH, G. Papierluftfilter Nutzfahrzeugen. *MTZ*. 1991, **52**(12).

[24] TAUFKIRCH, G., MAYR, G. Papierluftfilter für Motoren in Nutzfahrzeugen. *MTZ*. 1984, **45**(3), 95-105.

[25] MYSŁOWSKI, J. Doładowanie silników. *WKiŁ*, Warszawa 2011.

[26] TRUHAN, J. Filter performance as the engine sees it. *Filtration & Separation*. 1997, **34**(12), 1019-1022.

[27] WANG, Q., BAI, Y., XIE, J. et al. Synthesis and filtration properties of polyimide nanofiber membrane/carbon woven fabric sandwiched hot gas filters for removal of PM 2.5 particles. *Powder Technology*. 2016, **292**, 54-63.

[28] www.bmcairfilters.com.

[29] www.K&Nfilters.com.

[30] www.8thcivic.com/forums/bolt-ons-all-motor/38066-f1-intake.html.

[31] www.renaultsport-clio.blogspot.com/2006/09/bmc-cda-carbon-fibre-intake-air-filter.html.

[32] www.protonfilters.pl/filtry-sportowe.htm.

[33] www.google.pl/search?q=filtr+stożkowy+osłony+gorącego+powietrza&rlz=1C1CAFB_enPL683PL683&espv=2&biw=1280&bih=894&tbm=isch&tbo=u&source=univ&sa=X&ved=0ahUKEwjimeD8jKbSAhWD2CwKHeS8BlgQsAQIGQ&dpr=1.

[34] www.google.pl/search?q=filtry+stożkowe&oq=filtry+stożkowe&aqs=chrome.0.69i59j0l5.9375j0j8&sourceid=chrome&ie=UTF-8#q=filtry+sto%C5%BCkowe+bmc&*.

Tadeusz Dziubak, DSc., DEng. – Faculty of Mechanics Military University of Technology, Warsaw, Poland.

e-mail: *Tadeusz.Dziubak@wat.edu.pl*

Article citation info:
SIDOROWICZ, M., PIELECHA, I. The impact of injector placement on the dose preparation conditions in a gasoline direct injection system. *Combustion Engines*. 2018, **172**(1), 35-43. DOI: 10.19206/CE-2018-104

Maciej SIDOROWICZ
Ireneusz PIELECHA

CE-2018-104

The impact of injector placement on the dose preparation conditions in a gasoline direct injection system

Direct fuel injection requires appropriate conditions for proper ignition of the formed mixture. The proper combustion process is shaped by the direct fuel injection, whose parameters vary. Preparation of the dose requires proper injector placement in the combustion chamber. This article focuses on the issue of the injector specific spatial and angular position in order to implement the injection and atomization of the fuel. The injector's pseudo-optimal location has been presented along with several changed positions. The research was conducted as a simulation experiment using AVL FIRE 2017 software. The best position of the injector was selected based on the fuel spraying and injection process indicators. It has been shown that the spatial position has the most impact and the injector placement angle is of secondary importance.

Key words: *gasoline direct injection, fuel spraying, simulation software*

1. Introduction

Internal combustion engines with SI remain the main drives in passenger cars, and their position on the market will strengthen [6]. This trend is influenced by, among others, the current aim to reduce the share of CI engines in passenger cars, due to their negative environmental impact [8], and hybridization of car drives, by combining internal combustion engines with electric motors [7, 10].

The development of internal combustion engines with SI in recent years has focused on downsizing, i.e. increasing the engine's power while maintaining a small engine displacement value. This was enforced due to the apparent fuel economy (shown only in drive tests carried out under laboratory conditions) as well as the tax regulations used in many countries, where the fee for owning or purchasing a car is determined based on its engine's displacement value. Downsizing was achieved by increasing the intake air pressure supplied to the engine (mechanically, with a turbine or with a hybrid solution) and using direct fuel injection into the combustion chamber.

Gasoline direct injection is a solution that is currently very rapidly replacing indirect injection technology in spark ignition engines. The share of these injection systems in new vehicles equipped with SI engines in the US market increased in years 2009-2015 from 5% to 46%. It is believed that the share of these engines in all on-road vehicles will reach over 50% by 2020 [13]. There are many technical solutions for the fuel injection systems for SI engines, which have found commercial applications.

Direct injection allows the creation of a stratified lean fuel-air mixture [9]. There are various ways of shaping the fuel stream during direct injection, but all are aimed at creating a stoichiometric mixture in the vicinity of the spark plug, at the moment of discharge on its electrodes.

One of the methods of shaping the sprayed fuel injection stream is the spray-guided method, which consists of injecting liquid fuel in such a way that the fuel stream creates a stoichiometric mixture in the vicinity of the spark plug without interacting with any other factor aside from air.

Generally, a central position of the spark plug in the combustion chamber is preferred: this choice is motivated by the need to reduce the probability of knocking combustion, occurring when the unburned mixture furthest from the spark gap reaches auto-ignition before the arrival of the flame front. A central position of the spark plug allows a symmetrical propagation of the flame front initiated by the spark, taking a shorter path to extend combustion to the whole unburned mixture before auto-ignition occurs [5].

Injection tests were carried out by Zulkefli and Mansor [14] in relation to hydrogen direct injection. Different positions were analyzed (0, 53 and 90 deg) relative to the cylinder axis. It was found that the best position for the application of hydrogen direct injection in an internal combustion engine is the position of 0° from the combustion chamber axis. This position gives the largest mixing area and effective mass diffusivity of air and the flame can propagate uniformly for the entire combustion process.

Similar changes regarding the position of the injector are also important in dual fuel engines, in which the injection is carried out directly and indirectly. The influence of the CNG and H_2 injectors position change in the intake manifold was studied by Chintala and Subramanian [4]. It has been found that the proper location of the injector allows for a turbulence change of over 50%, which increases the combustible mixture formation rate. At the same time, the change of the injector position results in a 6% increase in the thermal efficiency of the engine and 5% increase for injected fuel pressure change (from 1 to 2 bar).

The influence of the methanol injector placement in a dual-fuel engine (diesel-methanol) was studied by Chen et al [3]. The research consisted of analyzing the change of the injector's distance from the inlet valve in the aspect of, among others, the exhaust emissions. It was found that only the maximum engine load affects changes in the emission value. An increase in NO_x and soot (FSN – filter smoke number) was observed. The influence of the methanol contribution to NO_x emission was low: no changes were noted in relation to the other injector positions, and with increasing the proportion of methanol – there was a decrease in NO_x emissions. No influence of the injector position on the emission of carbon monoxide and hydrocarbons was noted regardless of the engine load.

This way of shaping the mixture requires a geometric analysis of the injector setting in the combustion chamber, because it forces the initial conditions of the fuel stream movement. This article is intended to study this relation, to ultimately assess the applicability of such a solution.

2. Research aim and motivation

The proposed tests are a part of the study stage on the injection and combustion processes using a direct injection of liquid hydrocarbon fuels [11]. This stage focuses on determining the indicators for engine processes using one direct injection gasoline injector depending on its location in the combustion chamber of the internal combustion engine.

The aim of the research is to determine the optimal spatial position of the injector relative to the spark plug and the angular position of its axis relative to the cylinder axis. The optimal location will be determined as such at which the combustion indicators will reach their highest values. In order to assess the response, the variation of indicators will be performed.

3. Research methodology

Simulation tests were carried out using a workstation with AVL Fire 2017.0 software.

In order to examine the impact of the gasoline injector position relative to the combustion chamber, three angular positions of the injector relative to the cylinder axis and nine linear distances of the injector from the spark plug located centrally in the cylinder axis were selected as test parameters. Thus, the analysis results for 27 different injector placement positions were generated.

3.1. Combustion chamber geometry

The combustion chamber model is based on an internal combustion engine with geometrical parameters presented in Table 1.

Table 1. Modeled engine technical data

Parameter	Unit	Value
Type	–	Piston engine, 4-stroke, spark ignition
Cylinder number	–	1
Displacement	cm^3	385
Compression ratio	–	10.2
Bore	mm	83
Stroke	mm	71.2
Speed	rpm	2000

The displaceable mesh was created in the AVL Fire 2017.0 software using the Fame Engine Plus module (Fig. 1), in which the following selections were assigned:

- piston buffer,
- piston moving,
- piston non_moving.

The created mesh of size of 230 thousand cells (Table 2) served as the model for the injection and atomization analysis of gasoline (cell size: min: $5\cdot10^{-6}$ m; max: $2\cdot10^{-3}$ m).

Fuel injection and atomization tests were carried out with an angular resolution of 2 deg on the crankshaft.

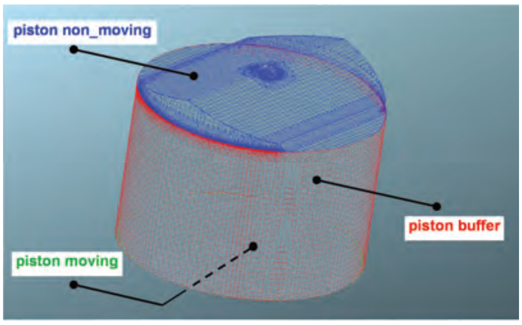

Fig. 1. The displaceable mesh of combustion volume for fuel spray simulation

Table 2. The computational mesh parameters

Mesh info	Value
Number of nodes	222671
Number of surface faces	41798
Number of tet cells	2050
Number of hex cells	177515
Number of pyramid cells	16019
Number of prism cells	34583
Total number of cells	230167
Surface area	0.031 m^2
Volume	0.000427 m^3

3.2. Different y, z distances from the spark plug

The first geometric parameter of the tests is the distance and position of the injector relative to the spark plug. As variables, the distances y and z are assumed in accordance with the AVL Fire 2017 coordinate system. The y direction coincides with the axis of the cylinder and the spark plug. The values of the y coordinate change are: 9, 10 and 11 mm. The z coordinate changes are 7, 8 and 9 mm. The x coordinate is constant and equal to 0, so that placing the injector tip is always in the yz plane. The values of coordinate variables are shown in Fig. 2.

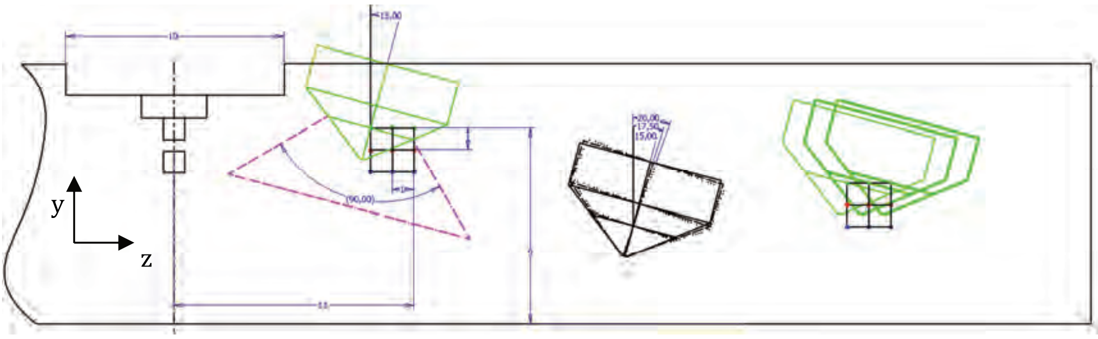

Fig. 2. Diagram of the injector position in relation to the spark plug together with the parameters selected for analysis of injection and combustion (angle, distance)

Each injector position is described by a code containing the change of position with respect to the y axis, with respect to the z axis, and the change of angle with respect to the cylinder axis:

$$\text{y(i)z(j)alpha(k)} \tag{1}$$

where: i = 7 mm, 8 mm and 9 mm, j = 9 mm, 10 mm and 11 mm, while k = 15, 17.5 and 20 deg.

3.3. Different injector placement angles

Another one of the geometrical parameters tested is the yaw angle of the injector axis with respect to the cylinder axis. Because of the different position of the injector relative to the cylinder (a spark plug is located in the cylinder axis, this is expected due to the end design solution – two injectors placed in the combustion chamber) the change in the angle of the injector axis relative to the cylinder axis is necessary. Three values were used to determine the effect of this angle on the dose mixture preparation process: 15 deg, 17.5 deg and 20 deg (Fig. 1).

3.4. Modeling the fuel injection

Fuel injection started at an angle of 670 deg and lasted 0.6 ms. The fuel dose was 13.1 mg, which corresponded to the value of the excess air ratio $\lambda = 1$.

The Schiller-Naumann drag law model C_d is an empirically evaluated equation for calculating the drag coefficient in drag force acting on the flowing particles in fluid with Re ranging from 0.2 to 1000. It is described with the equation:

$$C_d = 24/\mathrm{Re}\,(1 + 0.15\,\mathrm{Re}^{0.687}) \tag{2}$$

where Re is the Reynolds number. For the Re > 1000 the C_d has the constant value of 0.44 [6].

Fuel injection is based on the atomization of droplets taking into account the KH-RT model. The model of Kelvin-Helmholtz and Rayleigh-Taylor, which is a development of the Reitz-Diwakar model made by Reitz, is based on a linear analysis of instability which results in a dispersion equation determining the rate of initial surface disturbance in relation to the wavelength. Surface waves in the Kelvin-Helmholtz model (KH) and disturbances in the Rayleigh-Taylor model (RT) determine the distribution of droplets. These models differ in their approach to creating new droplets.

The new model takes into account the change in weight and the formation of droplets with smaller diameters. As a result, more smaller drops are obtained. The KH model is used when there are high flow rates and high density of the medium, and the RT model is used when the drops are slowed down rapidly, resulting in increased surface waves at the stop point of the droplets. This means that it is mainly used for high pressure injection (also of gasoline). Some authors [12] use this model to study direct injection of gasoline from multi-hole injectors supplied at a pressure of 7.5-12 MPa.

The following coefficient values were adopted in this model: $C_1 = 0.61$; $C_2 = 12$; $C_3 = 10$; $C_4 = 5.33$; $C_5 = 1$; $C_6 = 0.3$; $C_7 = 0.05$; $C_8 = 0.188$ [6].

C_1 is a KH-WAVE model constant to adjust stable droplet radius according to the formula:

$$R_a = C_1\Lambda \tag{3}$$

where R_a is a KH-WAVE model droplet radius, and Λ is a wave length function depending on the Weber's number of the continous phase and Ohnesorge's number of the droplet.

C_2 is a KH-WAVE model constant to adjust break-up time according to the formula:

$$\tau_a = \frac{3.7 C_2 R}{\Lambda\Omega} \tag{4}$$

where R is a droplet radius, and Ω is a break-up frequency function depending on the Weber's number of the continous phase and Ohnesorge's number of the droplet.

C_3 is a type constant to adjust break-up length according to the formula:

$$L = C_3\sqrt{\frac{\rho_d}{\rho_c}}\,d_0 \tag{5}$$

where ρ_d is a droplet density, ρ_c is a continous phase density and d_0 is a initial droplet diameter.

C_4 is an RT model constant to adjust wave length according to the formula:

$$\Lambda = C_4\frac{\pi}{K_t} \tag{6}$$

where K_t is a wave number assessed via:

$$K_t = \sqrt{\frac{g_t|\rho_d - \rho_c|}{3\sigma}} \tag{7}$$

where σ is a droplet surface tension and g_t is an deceleration of the droplet in the direction of travel.

C_5 is an RT model constant to adjust break-up time according to the formula:

$$\tau_t = C_5\frac{1}{\Omega_t} \tag{8}$$

where Ω_t is a break-up frequency assessed via:

$$\Omega_t = \sqrt{\frac{2}{3\sqrt{3}\sigma}\,\frac{g_t|\rho_d - \rho_c|^{1.5}}{\rho_d + \rho_c}} \tag{9}$$

C_6 determines the fraction of the parcel volume which has to be detached until child parcels are initialized. Its value is within the range from 0.1 to 0.5.

C_7 determines the fraction of the shed mass which is finally transformed into child parcels. Its value is within the range from 0.01 to 0.3.

C_8 is a constant to adjust droplet normal velocity according to the formula:

$$V_{norm} = C_8\Lambda\Omega \tag{10}$$

3.5. Evaporation modeling

The Dukowicz evaporation model describes the heat and mass transfer processes impact on the droplet-fluid border. The model is based on the following assumptions [1]:

- spherical symmetry,
- quasi steady gas-film around the droplet,
- uniform droplet temperature along its diameter,
- uniform physical properties of the surrounding fluid,
- liquid-vapor thermal equilibrium on the droplet surface.

The following coefficient values have been used in the model: $E_1 = 2$; $E_2 = 2$. E_1 is a heat transfer multiplicative factor and E_2 is a mass transfer multiplicative factor; both act on the transfer coefficient [1].

4. Impact of injector placement on fuel atomization conditions

Various injector positions were analyzed in terms of changes to: mass of evaporated fuel, mass of remaining (unevaporated) fuel, diameter of fuel droplets, turbulence kinetic energy, dissipation of energy and excess air ratio.

Figure 3 presents the results of fuel atomization analysis taking into account the change of the injector's position in the direction of the y axis (according to Fig. 2). The most advantageous position is far in the combustion chamber (reduction of the y coordinate). In this position (value y = 7 mm), the amount of vaporized fuel is the highest at a constant crankshaft angle (analysis was done for the angle 690 deg).

This is due to the proper distance of the injector from the spark plug electrodes. This injector position prevents the fuel stream from reaching the spark plug electrode and allows to increase the fuel evaporation. The extreme positions of the injector along the variable y (position changes in relation to the cylinder axis) relative to the solution adopted (y = 7 mm) result (at a crankshaft angle of 690 deg) in:

- increasing the evaporated fuel mass by 7.4%;
- decreasing the unevaporated fuel mass by 18.9%;
- reducing the droplet diameter by 2.6%;
- increasing the turbulence kinetic energy by 7.1%;
- increasing the energy dissipation by 17.7%;
- increasing the excess air ratio by 7.5%.

Changes in the position of the injector relative to the z axis (distance from the spark plug) do not cause such large changes in the indicators analyzed above (Fig. 4). The best solution is the location (z = 9 mm), because the evaporated fuel mass is the largest. The extreme position of the injector along the variable z (position changes in relation to the cylinder axis) with respect to the adopted solution (z = 9 mm) results (at an angle of 690 deg) in:

- increasing the evaporated fuel mass by 4.3%;
- decreasing the unevaporated fuel mass by 10.8%;
- reducing the droplet diameter by 6.8%;
- increasing the turbulence kinetic energy by 3.9%;
- increasing the energy dissipation by 8.2%;
- increasing the excess air ratio by 4.4%.

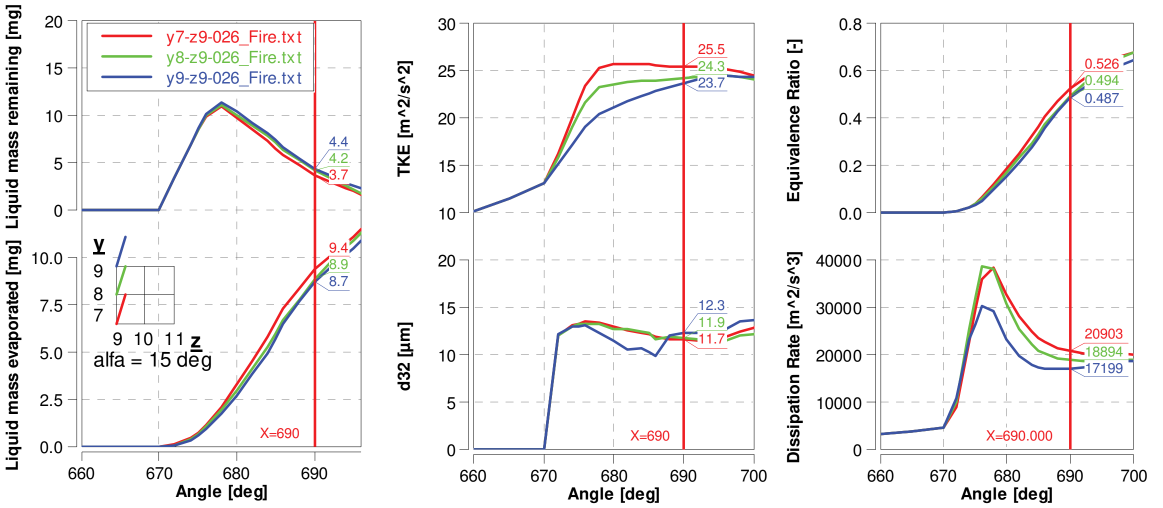

Fig. 3. Impact of the injector position change in the combustion chamber – y coordinate (changes in the injector placement height in the combustion chamber)

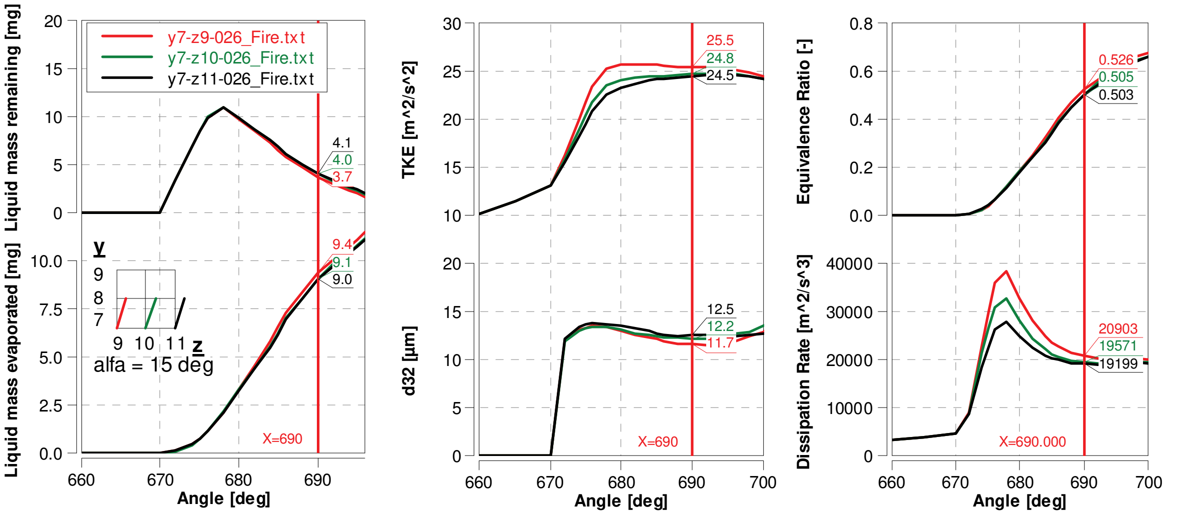

Fig. 4. Impact of the injector position change in the combustion chamber – coordinate z (changes of the injector distance from the spark plug in the combustion chamber)

The smallest change of the angular position of the injector (in relation to changes in y and z) leads to changes in the analyzed indicators (Fig. 5). The best solution is the angular position alpha = 15 deg, because the mass of evaporated fuel is the largest. Extreme positions of the injector (changes of the angular position) relative to the adopted solution (alpha = 15 deg) result (at an angle of 690 deg) in:

- increasing the evaporated fuel mass by 1.1%;
- decreasing the unevaporated fuel mass by 2.7%;
- reducing the droplet diameter by 2.6%;
- no change in the turbulence kinetic energy;
- increasing the energy dissipation by 0.1%;
- increasing the excess air ratio by 1.1%.

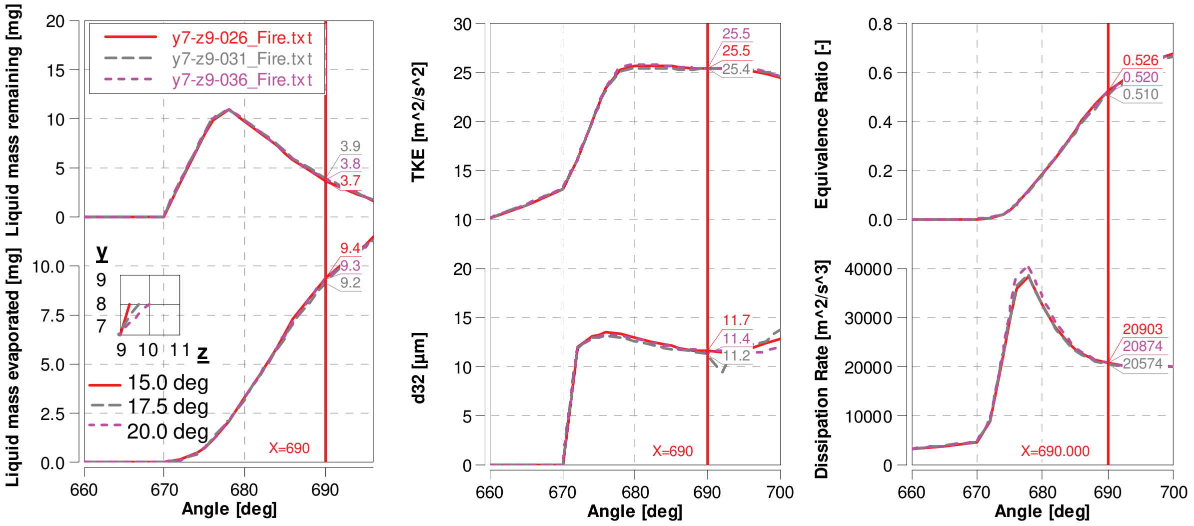

Fig. 5. Impact of the change of the injector position in the combustion chamber – alpha angle

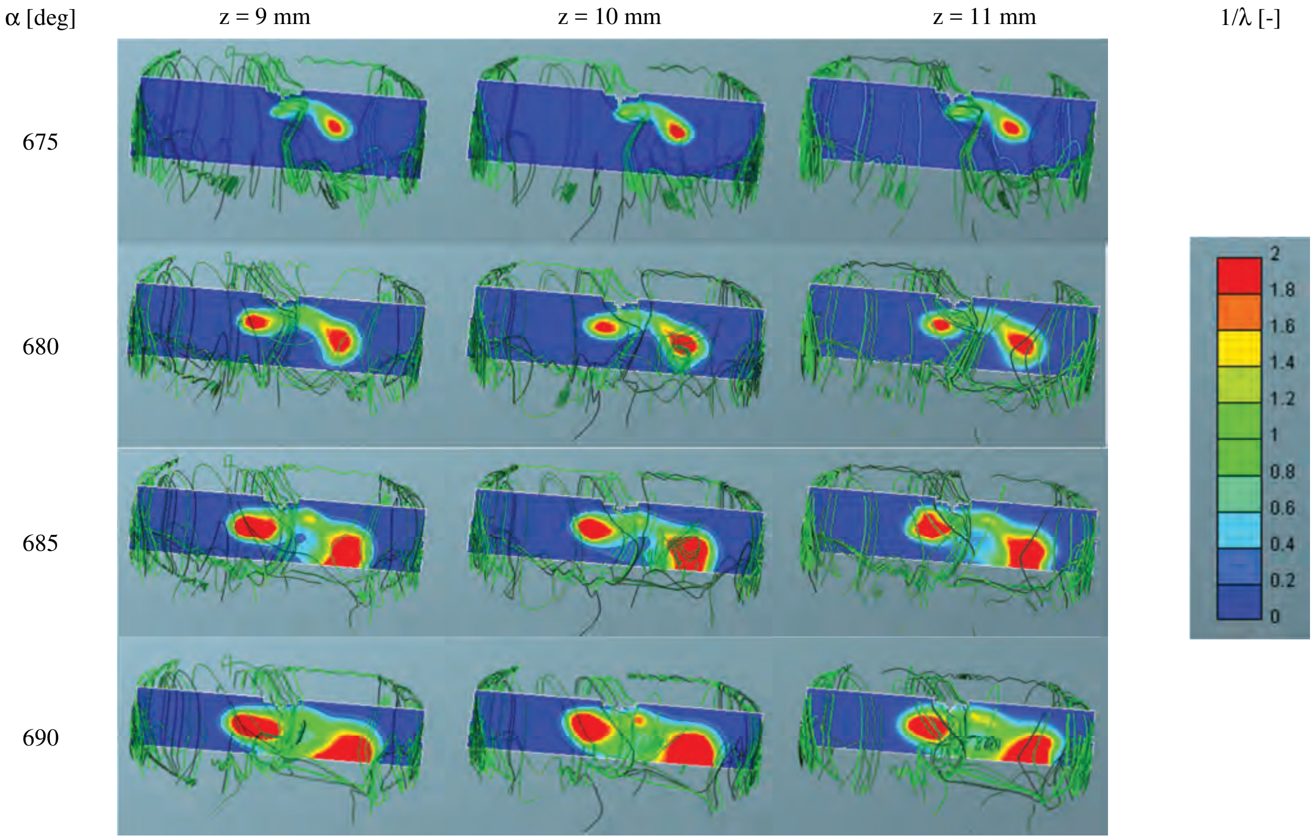

Fig. 6. Distribution of factor 1/λ in the combustion chamber for different positions of the injector with respect to the z axis (position code y(7)z(i)alpha(15), where i = 9, 10, 11, which means y = 7 mm, alpha = 15°)

The results of local fuel atomization processes were also helpful in further analysis. The distribution of the equivalence coefficient (1/λ) indicates its sensitivity to the injector location in the combustion chamber (Fig. 6). The figure shows three different injector positions relative to the z axis. Changing the position of the injector (its offset from the injector, thus increase in the z coordinate) results in a differentiation of the excess air coefficient around the spark plug. Excess air of 1 in the vicinity of the plug is limited by area. A tendency that remains present independent of the crankshaft angle.

Figure 7 shows the excess air coefficient constant value isosurface for gasoline injection depending on the angle of the crankshaft rotation at different z-coordinate values.

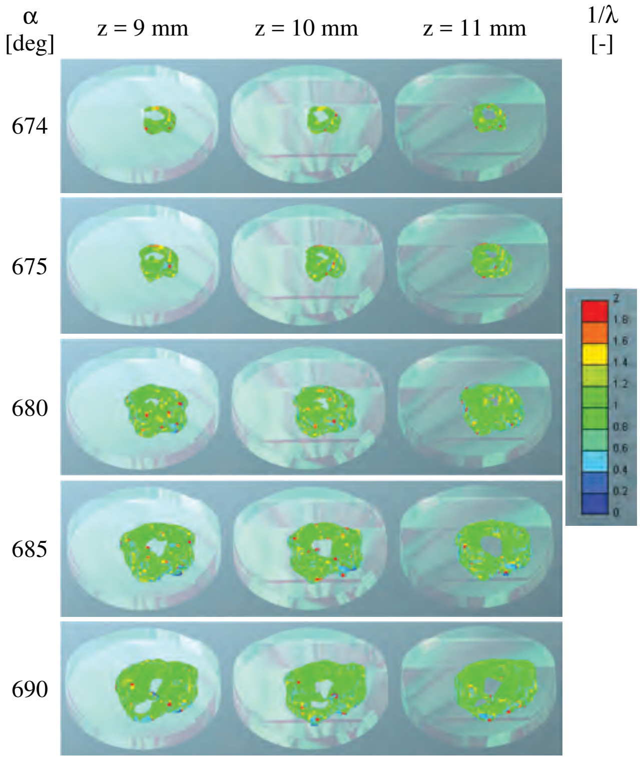

Fig. 7. Constant value isosurface λ = 1 on the combustion chamber background at various injector positions with respect to the z axis (position code y(7)z(i)alpha(15), where i = 9, 10, 11, which means y = 7 mm, alpha = 15°)

The presented isosurface indicate that a proper injector location results in specific effects in the development of the fuel dose in the combustion chamber. Due to the varied positioning of the injector, it is possible to choose the solution that is most advantageous in terms of fuel injection and atomization.

The different positioning of the injector also affects changes in the turbulence kinetic energy (TKE), which is responsible for the mixing of fuel and air. Its increase is observed during the fuel delivery from an injector located closer to the spark plug axis (Fig. 8). It follows that the closer position of the injector with respect to the spark plug results in a better fuel atomization and its mixing with the air, and thus such position allows to increase the evaporation of fuel.

5. Comparative analysis of the injector placement in the combustion chamber

First, the mass of evaporated fuel was determined for all injector positions relative to the angle of its location (Fig. 9a) at the engine's working angle of 690 deg. The comparison indicates that the largest mass of evaporated fuel is does not occur at the same injector position at each one of its placement angles. The highest values of evaporated fuel were obtained at the location coordinates of y(7)z(9)alpha(15) and y(7)z(9)alpha(20) – which means y = 7 mm and z = 9 mm at the angles of 15 and 20 deg. However, at an angle of 17.5 deg, the best option was to place the injector at the coordinates y = 7 and z = 11 (code y(7)z(11)alpha(17.5)).

Analysis of the average excess air ratio in the combustion chamber (at an angle of 690 deg) shows similar tendencies (Fig. 9b) to previous considerations. The largest values of the global excess air ratio were obtained for the same sequences.

These considerations prompted the authors to determine the best injector position through pseudo-optimization. With the obtained values of evaporated fuel mass, diameter of fuel droplets, turbulence kinetic energy, dissipation of energy, excess air ratio and the average temperature in the combustion chamber at an angle of 690 deg on the crankshaft, the data was scaled.

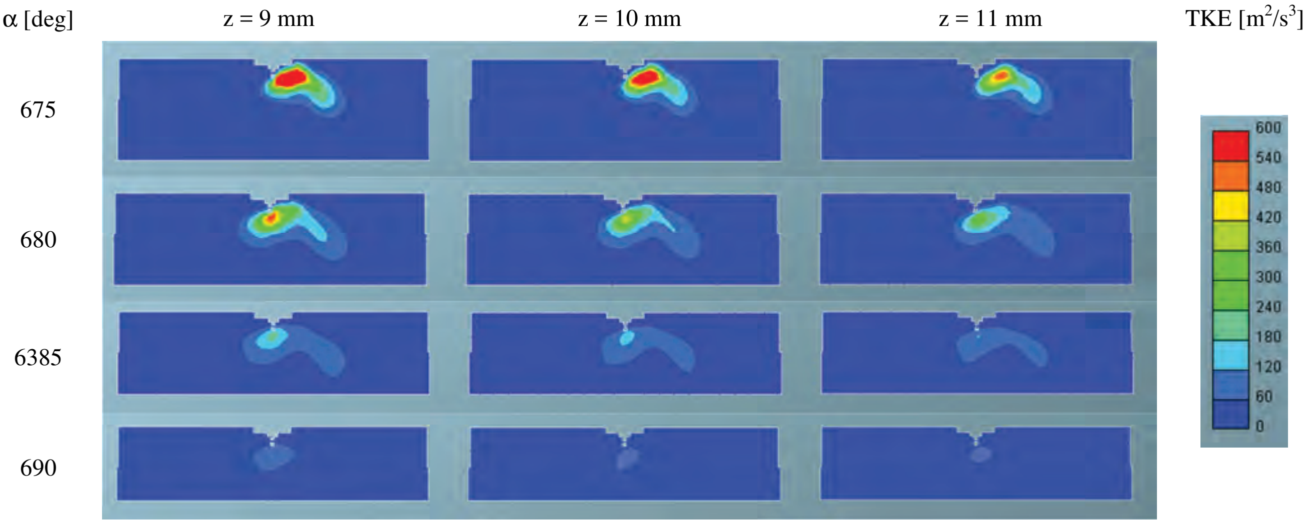

Fig. 8. TKE changes at different injector positions relative to the z axis (location code y(7)z(i)alpha(15), where i = 9, 10, 11, which means y = 7 mm, alpha = 15°)

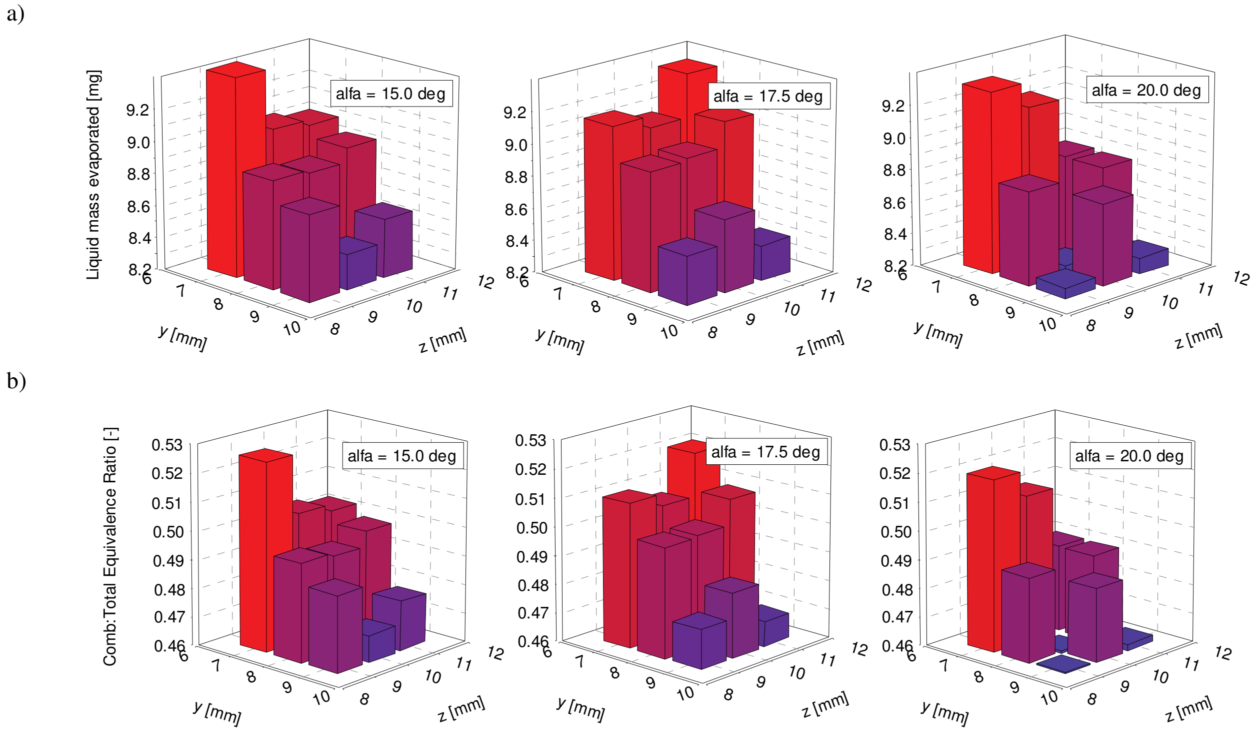

Fig. 9. Changes in fuel atomization indicators: a) weight of evaporated fuel, b) equivalence ratio (1/lambda) at various injector positions in the combustion chamber

Thus the following values have been used:

- the best value for a given indicator to take (the largest mass of evaporated fuel, smallest droplet diameter, the smallest energy dissipation, the largest TKE, the smallest equivalence factor – the largest value of excess air ratio and the highest temperature of the fuel dose) that can be obtained is equal to 1;
- the worst possible indicator value is 0.

The scaling was performed on this basis, and the results are presented in Table 3. The values of particular indicators have been assigned to each of the injector's positions.

Table 3. Relative values of fuel atomization and conditions present in the combustion chamber at individual injector positions

y	z	alfa	Liq. mass rem.	d32	Dissip. rate	TKE	Equiv. ratio	Temperature	Index
mm	mm	deg	kg	m	m^2/s^3	m^2/s^2	-	K	[-]
7	9	15	✓ 1.00	! 0.43	✓ 1.00	✓ 0.99	✓ 1.00	✗ 0.00	⇧ 4.42
		17.5	✓ 0.76	! 0.56	✓ 0.91	✓ 0.94	✓ 0.76	✗ 0.30	⇧ 4.25
		20	✓ 0.91	! 0.51	✓ 0.99	✓ 1.00	✓ 0.91	✗ 0.19	⇧ 4.50
	10	15	✓ 0.68	✗ 0.29	! 0.66	! 0.60	✓ 0.68	✗ 0.26	⇨ 3.17
		17.5	✓ 0.70	✗ 0.32	✓ 0.74	✓ 0.73	✓ 0.70	✗ 0.33	⇗ 3.53
		20	✓ 0.77	✗ 0.32	✓ 0.79	✓ 0.79	✓ 0.77	✗ 0.28	⇗ 3.73
	11	15	! 0.65	✗ 0.19	! 0.56	! 0.46	! 0.65	✗ 0.28	⇨ 2.79
		17.5	✓ 0.93	! 0.37	! 0.60	! 0.55	✓ 0.93	✗ 0.11	⇗ 3.49
		20	! 0.46	✗ 0.32	! 0.66	✓ 0.68	! 0.46	! 0.54	⇨ 3.13
8	9	15	! 0.52	! 0.37	! 0.48	! 0.33	! 0.52	! 0.40	⇨ 2.64
		17.5	! 0.58	✗ 0.31	! 0.49	! 0.35	! 0.58	! 0.47	⇨ 2.78
		20	! 0.45	! 0.43	! 0.45	! 0.36	! 0.45	✓ 0.67	⇨ 2.81
	10	15	! 0.51	! 0.41	! 0.43	✗ 0.31	! 0.51	! 0.43	⇨ 2.61
		17.5	! 0.60	✗ 0.33	! 0.42	! 0.34	! 0.60	! 0.44	⇨ 2.72
		20	✗ 0.00	✗ 0.00	! 0.42	! 0.38	✗ 0.00	✓ 0.90	⇩ 1.70
	11	15	! 0.59	✗ 0.24	! 0.33	✗ 0.29	! 0.59	✗ 0.28	⇘ 2.32
		17.5	✓ 0.73	✗ 0.21	✗ 0.33	✗ 0.29	✓ 0.73	✗ 0.20	⇘ 2.50
		20	! 0.46	✗ 0.26	✗ 0.32	! 0.33	! 0.46	! 0.55	⇘ 2.38
9	9	15	! 0.41	✗ 0.24	✗ 0.04	✗ 0.01	! 0.41	! 0.62	⇩ 1.74
		17.5	✗ 0.21	✓ 0.73	✗ 0.00	✗ 0.00	✗ 0.21	✓ 0.86	⇘ 2.02
		20	✗ 0.01	✓ 1.00	✗ 0.00	✗ 0.10	✗ 0.01	✓ 1.00	⇘ 2.13
	10	15	✗ 0.15	✗ 0.17	✗ 0.04	✗ 0.08	✗ 0.15	✓ 0.75	⇩ 1.33
		17.5	! 0.34	✗ 0.23	✗ 0.04	✗ 0.13	! 0.34	✓ 0.68	⇩ 1.76
		20	! 0.39	✓ 0.77	✗ 0.03	✗ 0.17	! 0.39	✓ 0.72	⇘ 2.47
	11	15	✗ 0.27	✗ 0.15	✗ 0.07	✗ 0.17	✗ 0.27	! 0.57	⇩ 1.49
		17.5	✗ 0.14	✗ 0.12	✗ 0.06	✗ 0.23	✗ 0.14	✓ 0.70	⇩ 1.39
		20	✗ 0.04	✗ 0.24	✗ 0.06	✗ 0.28	✗ 0.04	✓ 0.85	⇩ 1.52

Changes in these values occur in the range of <0;1>. The table also contains a pictogram analysis, which shows that the most positive results occur when placing the injector at the coordinates y = 7 mm and z = 9 mm or z = 10 mm. The worst position of the injector is the one with the y coordinate of y = 9 mm.

Due to the fact that it was still impossible to determine the best injector position, the normalized values of process indicators were summed for each of the injector positions (Fig. 10). Using such a summation method, the maximum possible value is 6 (when all normalized indicator values obtained were equal to 1). The highest value of 4.50 normalized indicators was obtained for the injector position with the co-ordinates y = 7, z = 9 and the angle alpha = 20 deg (code: y(7)z(9)alpha(20)), as shown in the column titled "Index" in Table 3. It should be noted, however, that all the injector angular positions at y = 7 and z = 9 (closest to the spark plug) obtained the highest values of the normalized sums.

Additionally, in Fig. 10, the sums of normalized fuel atomization indicators are summarized (sum of the "Index" column for individual injector positions). They were calculated as follows:

$$y(7\ \mathrm{mm}) = \Sigma\ y(7)z(j)\mathrm{alpha}(k) \tag{11}$$

$$y(8\ \mathrm{mm}) = \Sigma\ y(8)z(j)\mathrm{alpha}(k) \tag{12}$$

$$y(9\ \mathrm{mm}) = \Sigma\ y(9)z(j)\mathrm{alpha}(k) \tag{13}$$

$$z(9\ \mathrm{mm}) = \Sigma\ y(i)z(j)\mathrm{alpha}(k) \tag{14}$$

$$z(10\ \mathrm{mm}) = \Sigma\ y(i)z(j)\mathrm{alpha}(k) \tag{15}$$

$$z(11\ \mathrm{mm}) = \Sigma\ y(i)z(j)\mathrm{alpha}(k) \tag{16}$$

$$\mathrm{alpha}(15\ \mathrm{deg}) = \Sigma\ y(i)z(j)\mathrm{alpha}(15) \tag{17}$$

$$\text{alpha}(17.5\ \text{deg}) = \Sigma\ y(i)z(j)\text{alpha}(17{,}5) \quad (18)$$

$$\text{alpha}(20\ \text{deg}) = \Sigma\ y(i)z(j)\text{alpha}(20) \quad (19)$$

where: i = 7 mm, 8 mm and 9 mm, j = 9 mm, 10 mm and 11 mm, while k = 15, 17.5 and 20 deg.

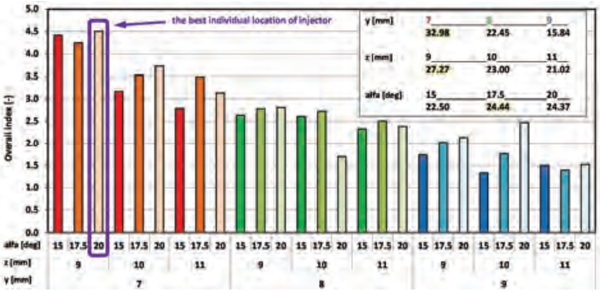

Fig. 10. Indicators of the best injector position selection based on selected quantities regarding fuel injection conditions (based on Table 1)

The performed comparison leads to the conclusion that the highest point value was obtained for the injector position y = 7 mm. This means that fuel atomization indicators take the highest values at this injector position, regardless of the other position variables. This position with the changing variable z is 9 mm. Although the best angular position turned out to be 20 deg (code y(7)z(9)alpha(20) – at y = 7 and z = 9 mm), the best results were obtained at an angle of 17.5 deg without taking into account the y and z coordinates.

The injector position change sensitivity range was determined to be:

$$\text{delta } y = 0.5(\max(y(i)z(j)\text{alpha}(k)) - \min(y(i)z(j)\text{alpha}(k))) \quad (20)$$

where the values max() and min() can be found in Table 3.

The results of these calculations are presented in Fig. 11. It follows that the results are most sensitive to the y coordinate injector position change – the height of the injector position. Another variable determining the total index sum value (expressed in numerical form in Fig. 10) is the change in distance from the axis of the spark plug. The least sensitive parameter for changes in fuel atomization indicators is the injector position angle within the limits adopted for the performed simulation tests.

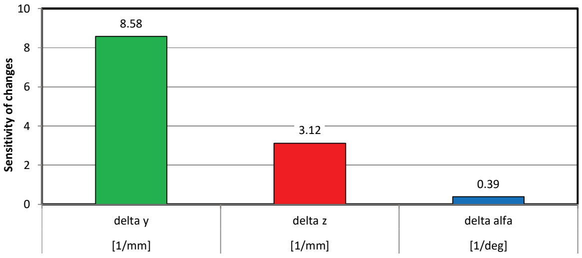

Fig. 11. The impact of changes in the size of the y, z and angle values of the injector in the combustion chamber

Conclusions

Injector location tests were conducted using computer simulation, which were used to analyze the fuel atomization indicators before ignition. The best solution was defined as one which, as a result of normalizing the indicators, allowed to obtain the largest value of the sum of all these indicator values.

The pseudo-optimal location (within the adopted model boundaries), was characterized by:

- the largest inset in the combustion chamber y = 7 mm,
- the shortest distance from the spark plug z = 9 mm,
- the highest angle in relation to the axis of the cylinder alpha = 20 deg.

The differences in the indicator values between the maximum changes in the injector inset in the combustion chamber were:

- 7.4% evaporated fuel mass;
- 18.9% unevaporated fuel mass;
- 2.6% droplet diameter;
- 7.1% turbulence kinetic energy;
- 17.7% energy dissipation;
- 7.5% excess air ratio.

The differences in the indicator values between the maximum changes in the injector distance from the spark plug were:

- 4.3% evaporated fuel mass;
- 10.8% unevaporated fuel mass;
- 6.8% droplet diameter;
- 3.9% turbulence kinetic energy;
- 8.2% energy dissipation;
- 4.4% excess air ratio.

The differences in the indicator values between the maximum changes in the injector angle relative to the cylinder axis were:

- 1.1% evaporated fuel mass;
- 2.7% unevaporated fuel mass;
- 2.6% droplet diameter;
- 0.0% turbulence kinetic energy;
- 0.1% energy dissipation;
- 1.1% excess air ratio.

Sensitivity of changes in the injector position was determined on the basis of the total indicator sum of changes in a given coordinate or angle (Fig. 11). The analysis of this sensitivity results in the following conclusions:

- the longitudinal change of the injector position is the most important value affecting changes in the fuel atomization indicators;
- this change is about 3 times more significant than the change in the position of the injector's distance from the axis of the spark plug and about 15 times more significant than the angle of the injector's position.

The conclusions obtained after the simulation analysis of the phenomenon will be taken into account in comparison of fuel atomization rates in the two injectors system and during combustion analyzes of both systems – with one and two injectors. The presence of a fuel stream from the second injector may be particularly significant, as Borowski demonstrated [2]. The second fuel stream will change the size of the turbulence and the associated with it mass of vaporized fuel.

Acknowledgements

The study presented in this article was performed within the statutory research (contract No. 05/52/DSMK/0265).

Nomenclature

C	coefficient value (injection model)
CI	compression ignition
CNG	compressed natural gas
d_{32}	Sauter mean diameter
d_0	initial droplet diameter
E	coefficient value (evaporating model)
FSN	Filter Smoke Number
g_t	deceleration of the droplet
H_2	hydrogen
KH	Kelvin-Helmholtz model
LPG	liquified petrolum gas
NO_x	nitrogen oxide
R_a	stable droplet radius
Re	Reynolds number
RT	Rayleigh-Taylor model
SI	spark ignition
TKE	turbulence kinetic energy
x	coordinate (0)
y	coordinate (direction coincides with the axis of the cylinder and the spark plug)
z	coordinate (direction coincides with the radial axis of the cylinder)
alpha	angular position
ρ_c	continuous phase density
ρ_d	droplet density
Λ	wave length function
λ	lambda value
σ	droplet surface tension

Bibliography

[1] AVL Fire 2017, AVL AST Documentation.

[2] BOROWSKI, P. Identification of the mixture creation and combustion in direct gasoline injection system with two injectors. *PhD thesis*. Publishing House Poznan University of Technology, Poznan 2016,

[3] CHEN, Z., YAO, C., YAO, A. et al. The impact of methanol injecting position on cylinder-to-cylinder variation in a diesel methanol dual fuel engine. *Fuel*. 2017, **191**, 150-163, doi:10.1016/j.fuel.2016.11.072.

[4] CHINTALA, V., SUBRAMANIAN, K.A. A CFD (computational fluid dynamics) study for optimization of gas injector orientation for performance improvement of a dual-fuel diesel engine. *Energy*. 2013, **57**, 709-721, doi:10.1016/j.energy.2013.06.009.

[5] FIENGO, G., DI GAETA, A., PALLADINO, A., GIGLIO, V. Common rail system for GDI engines modelling, identification, and control. *Springer Briefs in Automation and Robotics*. 2013. doi:10.1007/978-1-4471-4468-7_2.

[6] KAŁUŻNY, J., MERKISZ, J., GALLAS, D. et al. An innovative system for piston engine combustion with laser-induced ignition of the hydrocarbon fuel consisting carbon nanotubes. *Combustion Engines*. 2017, **168**(1), 3-14. doi:10.19206/CE-2017-101.

[7] MERKISZ, J., PIELECHA, I. *Mechanical systems for hybrid vehicles*. Publishing House Poznan University of Technology. Poznan 2015.

[8] MERKISZ, J., PIELECHA, J. *Nanoparticle emissions from combustion engines*. Springer Tracts on Transportation and Traffic, Springer International Publishing Switzerland, 2015, 8.

[9] PIELECHA, I. A study of direct multiple gasoline injection and combustion in terms of control of the engine processes. *Series of the dissertations*. No. 473, Publishing House Poznan University of Technology, Poznan 2012.

[10] PIELECHA, I., CIEŚLIK, W., SZAŁEK, A. Operation of hybrid propulsion systems in conditions of increased supply voltage. *International Journal of Precision Engineering and Manufacturing*. 2017, **18**(11), 1633-1639. doi.org/10.1007/s12541-017-0192-3.

[11] SIDOROWICZ, M., PIELECHA, I. Inflammability evaluation of hydrocarbon fuels mixtures formed directly in the combustion chamber. *Combustion Engines*. 2017, **170**(3), 57-65. doi:10.19206/CE-2017-309.

12] YI, Y., DEMINCO, C. Numerical investigation of mixture preparation in a GDI engine. *SAE Technical Paper* 2006-01-3375, 2006, doi:10.4271/2006-01-3375.

[13] ZIMMERNAM, N., WANG, J.M., JEONG, C.-H. et al. Assessing the climate trade-offs of gasoline direct injection engines. *Environmental Science & Technology*. 2016, **50**, 8385-8392, doi:10.1021/acs.est.6b01800.

[14] ZULKEFLI, M.H., MANSOR, M.R.A. The effect of injector position on direct injection hydrogen engine conditions. *Journal of Engineering Science and Technology*. Special Issue on 4th International Technical Conference 2014, 2015, 55-61.

Maciej Sidorowicz, MEng. – Faculty of Machines and Transport at Poznan University of Technology.

e-mail: *Maciej.Sidorowicz@doctorate.put.poznan.pl*

Ireneusz Pielecha, DSc., DEng. – Faculty of Machines and Transport at Poznan University of Technology.

e-mail: *Ireneusz.Pielecha@put.poznan.pl*

Article citation info:
GOŁĘBIOWSKI, W., WOLAK, A., ZAJĄC, G. Definition of oil change intervals based on the analysis of selected physicochemical properties of used engine oils. *Combustion Engines*. 2018, **172**(1), 44-50. DOI: 10.19206/CE-2018-105

Wojciech GOŁĘBIOWSKI
Artur WOLAK
Grzegorz ZAJĄC

CE-2018-105

Definition of oil change intervals based on the analysis of selected physicochemical properties of used engine oils

The paper presents the results of a thorough analysis of selected physicochemical parameters of engine oils at the end of their useful life, based on the oil change intervals assumed by vehicle users. Twelve samples of used Castrol Edge 5W/30 synthetic oil and five samples of used Castrol Magnatec 10W/40 semi-synthetic oil were tested. The Eralytics's ERASPEC OIL device was used for the assessment of the following parameters: degree of oxidation, degree of nitration, degree of sulfonation, water content, glycol content, total base number (TBN), total acid number (TAN) and kinematic viscosity at 40°C and 100°C. The research was conducted on the basis of the ASTM E2412-10 standard. The results regarding the parameter limit exceedances have also been presented in the paper. For both synthetic and semi-synthetic oils, the exceedance of kinematic viscosity measured at 40°C was particularly striking. In fourteen samples (out of seventeen tested), at least one exceedance of the limit value (out of nine analyzed) has been observed.

Key words: *degradation, engine oil, oil change, Eraspec, FT-IR, in-service oil*

1. Introduction

Lubricating oil plays an important role in ensuring engine performance and durability. However, extreme operating conditions of a combustion engine such as high temperature, high pressure and cold engine startup, strongly affect the acceleration of oil degradation. Thus, for any given in-service oil, both the changes in the chemical properties and the accompanying, broadly understood, multi-faceted deterioration of quality may be equally observed [10].

A precise determination of the degree of oil degradation is very important for technical and economic reasons; however, due to oftentimes severe and varying operating conditions, the oil aging processes should be considered individually for each drive unit [2, 12]. Most of the changes in the parameters of in-service oils during actual operation are difficult to detect. It is equally difficult to recognize (during oil operation) the moment when the oil reaches critical levels of its physicochemical properties. It may often be observed that after some period of apparently proper operation of the engine, a sudden increase in its wear or the engine failure occurs. In such cases, an in-depth analysis of the potential causes of the failure is rarely conducted, although it might reveal the impact of oil quality on the incident. Frequent oil contamination checks may help prevent engine failure as oil is a valuable source of information about the processes and causes of engine wear [8]. The effects of improper oil use or incorrectly set oil change intervals are apparent when the engine is being repaired. On the basis of the inspection of the removed pistons, the formation and the type of impurities deposited on them can be determined. It is extremely important to regularly replace used engine oil with the fresh one, which will clean the whole lubrication system (at the initial phase of service life) and then secure it at subsequent stages of use [3]. Information on the condition of an in-service lubricating oil is usually obtained through the means of analyzing changes in selected parameters in relation to the fresh products or comparing those parameters with their limit values [13]. The degree of engine oil degradation can be accurately determined by laboratory methods through analyzing a series of oil samples. With the used of laboratory methods, a number of oil parameters such as: kinematic viscosity, viscosity index, degree of oxidation, nitration and sulfonation, total acid and total base number, water and glycol content, or antioxidant content can be determined. This gives a full picture of the oil condition. Due to the fact that engine oils undergo a process of degradation under all operating conditions, they must be periodically changed. The generally accepted criteria for replacing engine oil in passenger cars i.e.: the number of kilometers traveled or the schedules based on average data prepared for different vehicles, are not always sufficient to accurately assess the level of oil deterioration [5, 9]. Too short oil change interval results in increased vehicle maintenance costs. On the other hand, when the oil change interval is too long, the engine wear may increase sharply, which might even lead to engine damage [1, 4]. Thus, the decision regarding oil change interval should mainly depend on the use and operating conditions of the vehicle [4]. The purpose of the study was to assess whether the criteria generally applied by the vehicle users as regards oil change interval are appropriate. The paper presents the results of a thorough analysis of selected physicochemical parameters of engine oils at the end of their useful life, based on the oil change intervals assumed by vehicle users. All engine oils tested came from cars used by private individuals. The parameters selected for testing provide insight into the processes of oil aging under operating conditions and contribute to determining the remaining useful life of oils [6, 7].

2. Materials and methods

The research material comprised of a series of engine oil samples collected during a standard oil change procedure from passenger cars of different manufacturers and with various levels of mileage. Only the samples of synthetic oils Castrol Edge 5W/30 and Castrol Magnatec 10W/40 were considered in the test. All of the oil samples were obtained from two car repair and servicing workshops in the area of Lublin Voivodeship. Twelve samples of used Castrol Edge 5W/30 synthetic oil and five samples of used

Castrol Magnatec 10W/40 semi-synthetic oil were tested. More detailed information concerning the cars used in the tests are presented in Table 1. The sample code includes the name of the test oil (CE – Castrol Edge, CM – Castrol Magnatec) and the type of engine [D-diesel, G-Gasoline].

Table 1. Detailed information concerning the cars used in the test

		Make of car	Engine	Sample code	Car mileage	Mileage since last oil change
CASTROL EDGE 5W/30	1.	Volvo XC 60	diesel	CED01	52 000 km	10 000 km
	2.	Volvo V50	diesel	CED02	192 000 km	10 000 km
	3.	Nissan X trial	diesel	CED03	243 000 km	11 000 km
	4.	Opel Astra	diesel	CED04	205 000 km	12 000 km
	5.	Audi A6	gasoline	CEG05	240 000 km	12 000 km
	6.	Seat Leon	diesel	CED06	122 000 km	14 000 km
	7.	Audi Q7	diesel	CED07	166 000 km	15 000 km
	8.	Skoda Fabia	diesel	CED08	136 000 km	15 000 km
	9.	Skoda Fabia	diesel	CED09	120 000 km	16 000 km
	10.	VW Touareg	diesel	CED10	293 000 km	24 000 km
	11.	BMW X5	diesel	CED11	212 000 km	28 000 km
	12.	BMW E61	diesel	CED12	169 000 km	30 000 km
CASTROL MAGNATEC 10W/40	1.	Ford Mondeo MK II	diesel	CMD01	294 000 km	10 000 km
	2.	Mercedes C220	diesel	CMD02	195 000 km	10 000 km
	3.	Ford Mondeo MK II	gasoline	CMG03	233 000 km	12 000 km
	4.	Daihatsu Terios	gasoline	CMG04	181 000 km	13 000 km
	5.	Skoda Romster	gasoline +LPG	CMG05	280 000 km	15 000 km

In order to determine the qualitative changes of the engine oils at the end of their useful life, they were analyzed with the use of ERASPEC OIL apparatus manufactured by Eralytics. It is a portable mid-range infrared FT-IR spectrometer designed to measure the key parameters of lubricating oils, which fully complies with the requirements of European and American standards. The device was used for the assessment of the following parameters: degree of oxidation, degree of nitration, degree of sulfonation, water content, glycol content, total base number (TBN), total acid number (TAN) and kinematic viscosity at 40°C and 100°C. The tests were conducted on the basis of the ASTM E2412-10 standard. The samples and the apparatus were prepared in accordance with the manufacturer's recommendations printed in the user manual. In order to determine the condition of oils, the limit values for the parameters tested were adopted based on the subject literature. This also required determination of the initial values of the selected oils; that is why, the samples of fresh Castrol Edge and Magnatec oils were tested. The physicochemical properties of the oils, measured at the beginning of the experiment are presented in Table 2. Details of the adopted limit levels and values that may be found in the subject literature are given in Table 3.

Table 2. The physicochemical properties (as measured) of fresh Castrol Edge 5W/30 and Castrol Magnatec 10W/40 engine oils used in the tests

Name	Unit	Castrol Edge 5W/30	Castrol Magnatec 10W/40
Kinematic viscosity at 40°C	mm^2/s	68,7	68,2
Kinematic viscosity at 100°C	mm^2/s	11,0	10,9
TBN	mgKOH/g	5,52	7,38
TAN	mgKOH/g	2,16	1,38

Table 3. Details related to limit values

Parameter	Unit	Limit values				
		According to subject literature				Adopted in this paper
		[11]	[5]	SAE J300-2015	[10]	
Kinematic viscosity (40 °C)	[mm^2/s]	–	±15%	–	±15%	±15% => (5W) – min 58.4; max 79.1 (10W) – min 57.9; max 78.4
Kinematic viscosity (100 °C)	[mm^2/s]	14.5–15.7	–	(5W) – min 9.3 max <12,5 (10W) – min 12,5 max <16,3	±15%	±15% => (5W) – min 9.3; max 12.5 (10W) – min 9.4; max 12.7
Total Acid Number	[mg KOH/g]	At the point of intersection, of both TAN & TBN trend lines,	–	–	6 mg KOH/g	+2.5 mg KOH/g (5W) – max 3.9 (10W) – max 4.7
Total Base Number	[mg KOH/g]	50% reduction	< 30%	–	< 30%	< 50% (5W) – max 3.7 (10W) – max 2.8
Degree of oxidation	[Abs/ (0.1 mm)]	-	> 1.0	–	> 0.4	> 0.4
Degree of nitration	[Abs/ (0.1 mm)]	-	> 1.0	–	> 0.4	> 0.4
Degree of sulfonation	[Abs/ (0.1 mm)]	-	> 1.0	–	> 0.4	> 0.4
Water content	[% m/m]	-	> 0.3	–	–	> 0.2
Glycol content	[% m/m]	-	> 0.3	–	–	> 0.3

Source: own elaboration

The measurements were made in triplicate. The results obtained were statistically analyzed using the Statistica 12 software package. In order to present the obtained results, a box and whisker chart was used for each of the analyzed variables, in three kilometer intervals (10-12k, 14-16k and 24-30k). The following items were included in the charts: values tested (outliers and extremes); median and data frame (quartiles – 25. and 75. percentile).

3. Results and discussion

All of the Castrol Magnatec 10W40 semi-synthetic oil samples tested exceeded the kinematic viscosity limit value at 40°C (Fig. 1). For the CMG03 sample, the oil viscosity exceeded the minimum limit of critical value, whereas in the rest of the samples, even the maximum value adopted was exceeded. It should be noted that higher viscosity was observed in the group of vehicles with higher mileage (14,000–16,000 km).

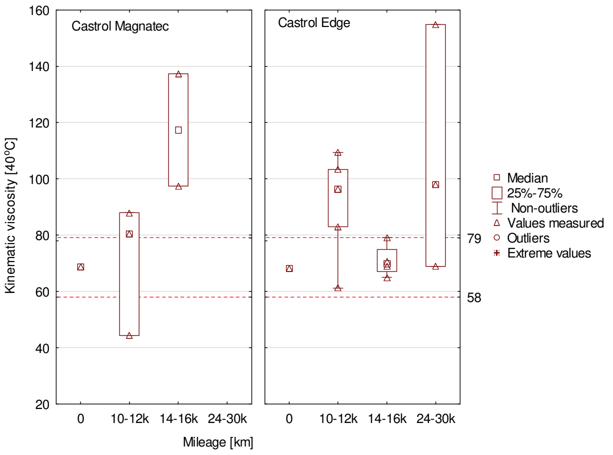

Fig. 1. Kinematic viscosity at 40°C of the engine oils tested

Upon analyzing the results of kinematic viscosity tests at 40°C for Castrol Edge 5W30 synthetic oil (Fig. 1) it was found that five of the samples tested were within the acceptable range. For seven of the samples tested, the upper limit was exceeded, indicating that the viscosity of the oil became too high.

Similarly, analyzing the kinematic viscosity at 100°C of used engine oils (Fig. 2), it can be observed that in three of the samples of semi-synthetic Castrol Magnatec 10W40 oil, the critical values were obtained. These were the following oil samples: CMG04, CMD02 and CMG03. For the first two samples, too high oil viscosity (14.27 and 12.8 mm^2/s, respectively) was noted, whereas in the case of the CMG03 sample – it was too low (6.47 mm^2/s).

On the one hand, too high viscosity greatly hampers the oil spreading on the surfaces of the cooperating parts of the engine, while too low viscosity (too thin oil film) results in a lack of adequate protection against friction. High soot content may be the reason for the exceedance of the limit value. In the case of diesel engines, the reason might also be the dilution of oil with fuel, and in the case of (petrol) gasoline engines – excessive oxidation. Two samples (CMG01 and CMG05) were within acceptable range.

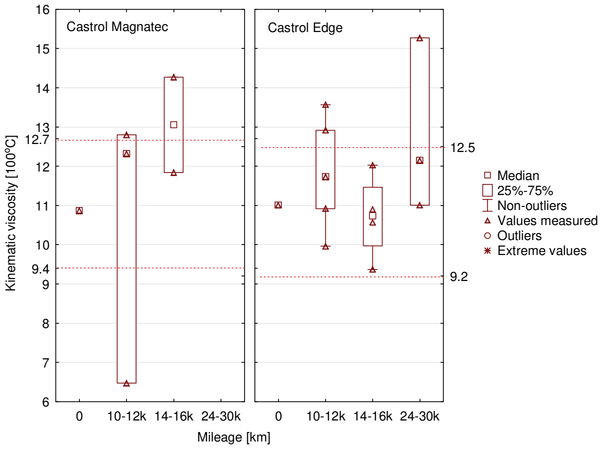

Fig. 2. Kinematic viscosity at 100°C of the engine oils tested

For Castrol Edge 5W30, three samples exceeded the critical value (Fig. 2). These were the following: CEG05, CED11 and CED02. In all cases, the oil viscosity became too high after the service life ended. A very high viscosity was observed for the CED11 sample after 28,000 km, indicating a rise in viscosity resulting from oil thickening by degradation products. In the remaining nine samples the kinematic viscosity was within the limits.

The next test parameters examined were total base number (TBN) and total acid number (TAN). The total base number is a measure of the alkaline reserve, thanks to which the oil has the ability to neutralize acidic oxidation or sulphate products, and the total acid number is a measure of this acidification. The results of the TBN measurements of the oil samples tested are presented in Fig. 3. Upon analyzing the TBN measurement results in used Castrol Magnatec oil samples, it was found that all of them were within the specified limits and did not fall below the accepted minimum limit of 3.7 mg KOH/g.

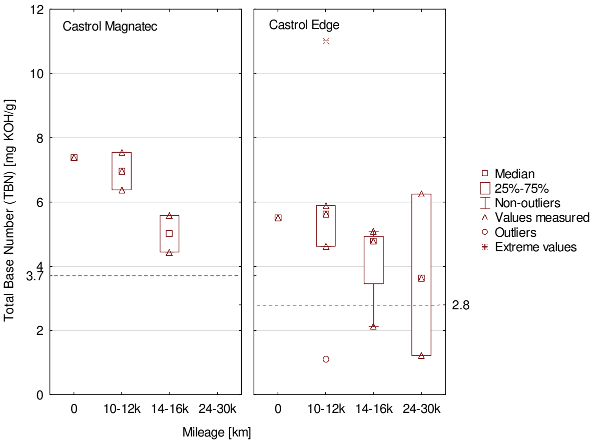

Fig. 3. The Total Base Number analysis for the engine oils tested

From among all of the analyzed samples of Castrol Edge, nine showed a value higher than the assumed minimum, while in three samples the achieved value was lower than the assumed minimum. These were the following samples: CED03 – 1.11 mg KOH/g, CED12 – 1.22 mg KOH/g and CED06 – 2.13 mg KOH/g. Such TBN values are insufficient to neutralize the acids. One sample showed a very high TBN level – 11.02 mg KOH/g. It was collected from a car coded as CEG05. In both examined groups, a downward trend can be observed depending on the degree of oil use.

The Total Acid Number analysis (TAN) in the Castrol Magnatec oils tested showed that three samples exceeded the assumed critical value of 3.9 mg KOH/g. These were: CMG04 with 6.24 mg KOH/g, CMG05 with 4.70 mg KOH/g and CMG03 with 3.97 mg KOH/g (limit value only slightly exceeded). It is noteworthy that oils up to 10–12,000 km of mileage do not exceed the critical TAN value.

Upon analyzing the test results for Castrol Edge synthetic oil, it was observed that none of the examined samples exceeded the limit value of 4.6 mg KOH/g. Nevertheless, two of the samples showed values which were very close to the limit – CED12 (4.54 mg KOH/g) and CED03 (4.54 mg KOH/g). The results of Total Acid Number analysis for the oils tested are presented in Fig. 4.

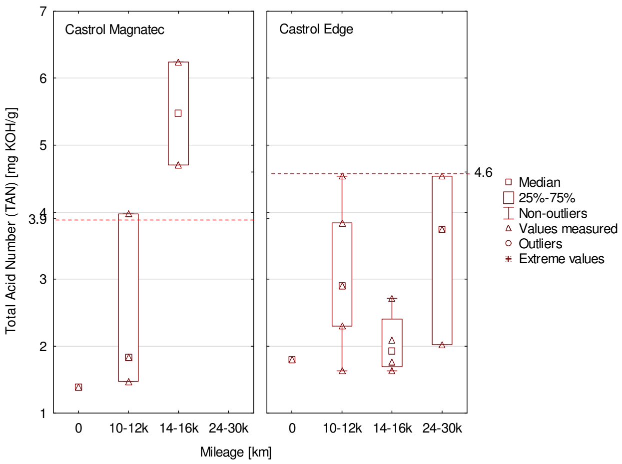

Fig. 4. The Total Acid Number analysis for the engine oils tested

Oxidation is a natural process occurring during the service-life of oil. Too high degree of oil oxidation results in oil degradation, loss of its lubricating properties and a decrease in corrosion protection. Among Castrol Magnatec 10W/40 oil samples tested, only one of them exceeded the assumed critical value (CMG03 – 0.43 Abs/0.1 mm). In the Castrol Edge 5W/30 group, two samples exceeded the limit value (CED03 – 0.46 Abs/0.1 mm and CED12 – 0.45 Abs/0.1 mm). The test results showed an upward trend in oxidation depending on the degree of oil use. The degree of oxidation of the engine oils tested is presented in Fig. 5.

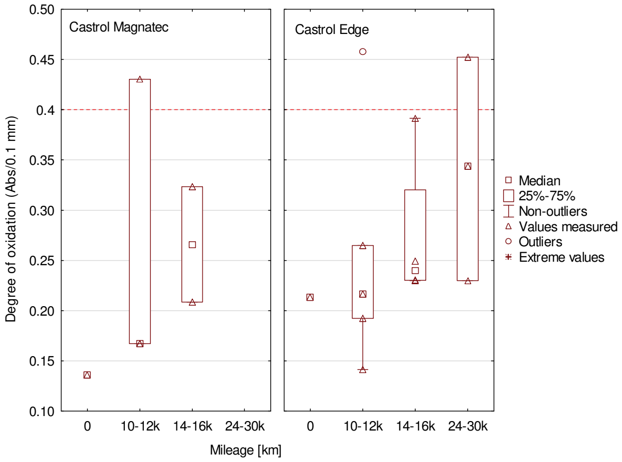

Fig. 5. The degree of oxidation of the engine oils tested

Nitration is the process by which deposits form as a result of the reaction of oil with nitrogen oxides (NO_x). This process leads to the formation of oil sludge and other deposits on the metal parts of the engine, thus contributing to oil degradation, loss of its lubricating properties and a decrease in corrosion protection. Nitration is a particular problem for engines equipped with exhaust gas recirculation (EGR). The degree of nitration of the engine oils tested is shown in Fig. 6.

The highest value of the degree of nitration was observed for CMG04 – 0.203 Abs/0.1mm; and just like in the case of all other samples tested, the obtained value was within the limit of no more than 0.4 Abs/0.1 mm (the reference line is outside the scale range). It is worth noting that even high levels of mileage (30,000 km) had no significant effect on the degree of nitration.

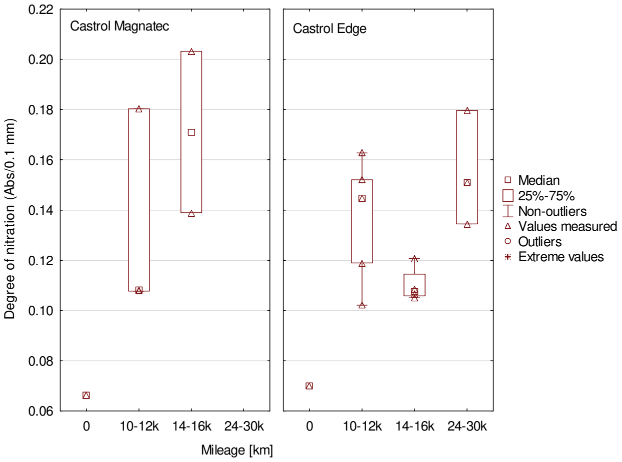

Fig. 6. The degree of nitration of the engine oils tested

The next parameter analyzed was the degree of sulfonation of used engine oils. This is a process that stems from the reaction of sulfur (mainly contained in fuel) with oxygen. As a result of this process, sediment is formed inside the engine, and with addition of water, also sulfuric acid. Sulfonation increases the wear of quality additives in engine oils. This is of particular importance if the engines are equipped with an EGR system. The degree of sulfonation of the engine oils tested are presented in Fig. 7.

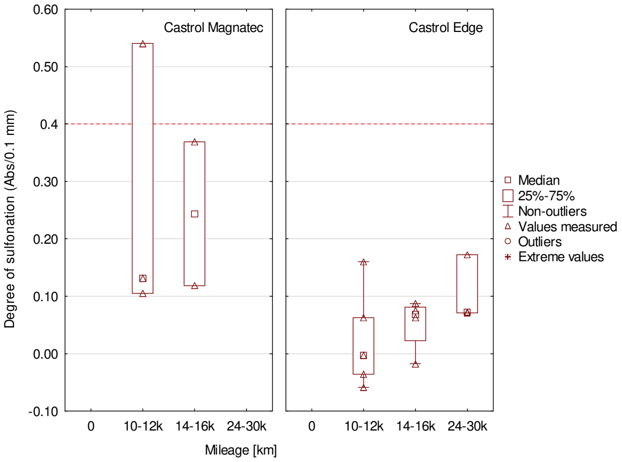

Fig. 7. The degree of sulfonation of the engine oils tested

The test results show that all of the Castrol Edge 5W30 oil samples were below the assumed maximum limit (0.4 Abs/0.1 mm), whereas in the group of Castrol Magnatec 10W40 oils – one sample exceeded the limit value (CMG03 – 0.54 Abs/0.1 mm).

The last parameters tested were water (Fig. 8) and glycol content (Fig. 9). The presence of water in engine oil adversely affects the corrosion protection and leads to oil degradation. Too high water content may indicate leaks in the lubrication system, defects or leaks in water separators, or leakage from the cooling system. Upon analyzing the test results for the presence of water in the examined engine oils, it was found that all Castrol Magnatec oil samples showed lower values than the upper limit of tolerance, whereas in two of the Castrol Edge oil samples those values were exceeded. One of the samples was collected from a car with self-ignition engine and mileage of 10,000 km since the last oil change (CED02 – 0.24 Abs/0.1 mm), and the other from a car with a self-ignition engine and mileage of 28,000 km since the last oil change (CED11 – 0.34 Abs/0.1 mm).

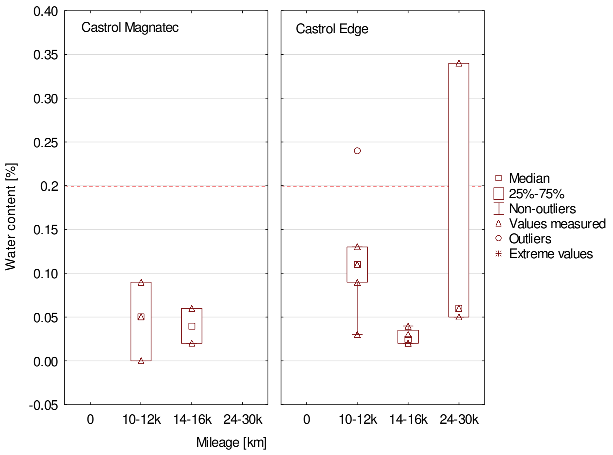

Fig. 8. The water content of the engine oils tested

Generally, there should be no glycol in engine oils. However, if glycol content is detected, it may indicate an engine defect, particularly a damaged engine head or the wear of a gasket under the engine head. Analysis of glycol content in oil can provide valuable information in situations requiring engine repair. The test results show that three of the Castrol Magnatec oil samples exceeded the assumed limit value. Two of the samples were collected from cars with spark ignition engines, one of them had the mileage of 10,000 km since the last oil change (CMD01 – 1.6%), and the other – the mileage of 13,000 km since the last oil change (CMG04 – 1.3%). The third sample was collected from a car with spark ignition engine and LPG gas installation with the mileage of 15,000 km since the last oil change (CMG05 – 1.5%).

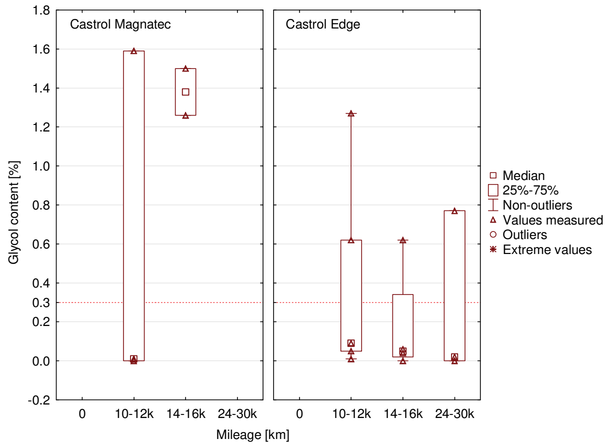

Fig. 9. The glycol content of the engine oils tested

In the Castrol Edge group of oils, it was found that as many as four samples exceeded the assumed limit value. Three of the samples were collected from cars with self-ignition engines and the following mileages since the last oil change: 12,000 (CED04), 15,000 (CED07) and 28,000 km (CED11). One sample, collected from a spark ignition engine with the mileage of 12,000 km (CEG05) showed the highest level of glycol content – 1.27% which may indicate that some of engine components should be repaired.

Exceedances of the limit values for the analyzed oil parameters are summarized in Table 4. In the group of vehicles whose engines were lubricated with a semi-synthetic oil, two and more exceedances were found for each of the tested vehicles. The situation was different for vehicles whose engines were lubricated with a synthetic oil. In three of the cars tested no exceedances were found, and in two other cars only one exceedance per car. The parameter that showed the highest number of exceedances was the kinematic viscosity at 40°C – for synthetic oil seven exceedances were observed (out of 12 samples tested), and five (out of 5 samples tested) for semi-synthetic oil. The parameters that showed the lowest number of exceedances for synthetic oils were: the degree of oxidation, water content and TAN – for which two exceedances each were recorded. It is worth noting that no exceedances were found for the degree of nitration and sulfonation. Similar situation was observed for semi-synthetic oils where the lowest number of exceedances was found for the degree of oxidation and sulfonation - one oil sample per each parameter. No exceedances were found for the degree of nitration, water content and TBN.

Upon analyzing the results of the study, it can be observed that it might be difficult to detect a relationship between the oil quality at the point of oil change with the technical state of the engine expressed by its mileage, as the exceedances were found for both vehicles with the mileage of about 100,000 km and for vehicles with the mileage of over 200,000 km. At the same time, in the group of synthetic oils for vehicles with no exceedances found, there were some with the mileage of 120–130,000 km as well as some with the mileage of nearly 300,000 km.

When taking into account the mileage since the last oil change, there are no clear trends visible either. The semi-synthetic oil was generally changed after 10–15,000 km, whereas the synthetic one from 10,000 km up to even 30,000 km (according to the engine manufacturer's approval as long-life oil). In several cases, engine oil with the mileage of 16,000 and even 24,000 km since the last change did not show any limit value exceedances. On the other hand, in some cases even relatively small mileage (of ca. 10–13,000 km) would exhibit exceedances for more than one parameter. It may then be concluded that oil condition strongly depends on the operating conditions. In only two cases (CED04 and CMG04) the decision to change oil after only 11,000–13,000 km traveled was actually made too late. On the other hand, one of the vehicles (CED10), after 24,000 km traveled, showed no exceedances. The abovementioned vehicles were off-road ones, so it might be presumed that the first two were actually used in difficult road conditions (the oil wears faster), and the third one was operated in more standard road driving conditions. These cases suggest that the oil change interval should be determined not only on the basis of the car mileage (mileage since the last oil change), but also taking into account the conditions under which the vehicle is generally used. According to Idzior and Wichtowskiej [2016], with regard to the purchase price of a new or used engine, frequent oil changes are a relatively low cost procedure. It should be considered, however, that oil changes should not take place more often than every 10,000 km – and that is mostly due to environmental reasons – unless the conditions of use do not allow for such long use of oil. Individual parameter values should always be analyzed together with the limit value exceedances.

Table 4. Exceedances of the limit values for the analyzed oil parameters: a summary

		Sample code/ Make of car	Engine	Car mileage [km]	Mileage since last oil change [km]	Viscosity at 40°C	Viscosity at 100°C	TAN	TBN	Degree of oxidation	Degree of nitration	Degree of sulfonation	Water content	Glycol content	**Total**
CASTROL EDGE 5W/30	1.	CED01/Volvo XC 60	diesel	52 000	10 000	✓	X	✓	✓	✓	✓	✓	✓	✓	**1/ 9**
	2.	CED02/Volvo V50	diesel	192 000	10 000	X	✓	✓	✓	✓	✓	✓	X	✓	**2 / 9**
	3.	CED03/Nissan X trail	diesel	243 000	11 000	X	✓	X	X	X	✓	✓	✓	✓	**4 / 9**
	4.	CED04/Opel Astra	diesel	205 000	12 000	X	X	✓	✓	✓	✓	✓	✓	X	**3 / 9**
	5.	CEG05/Audi A6	gasoline	240 000	12 000	X	✓	✓	✓	✓	✓	✓	✓	X	**2 / 9**
	6.	CED06/Seat Leon	diesel	122 000	14 000	✓	✓	✓	X	✓	✓	✓	✓	✓	**1 / 9**
	7.	CED07/Audi Q7	diesel	166 000	15 000	X	✓	✓	✓	✓	✓	✓	✓	X	**2 / 9**
	8.	CED08/Skoda Fabia	diesel	136 000	15 000	✓	✓	✓	✓	✓	✓	✓	✓	✓	**0 / 9**
	9.	CED09/Skoda Fabia	diesel	120 000	16 000	✓	✓	✓	✓	✓	✓	✓	✓	✓	**0 / 9**
	10.	CED10/VW Touareg	diesel	293 000	24 000	✓	✓	✓	✓	✓	✓	✓	✓	✓	**0 / 9**
	11.	CED11/BMW X5	diesel	212 000	28 000	X	X	✓	✓	✓	✓	✓	X	X	**4/ 9**
	12.	CED12/BMW E61	diesel	169 000	30 000	X	✓	X	X	X	✓	✓	✓	✓	**4/ 9**
		Total				**7**	**3**	**2**	**3**	**2**	**0**	**0**	**2**	**4**	
		Sample code/ Make of car	Engine	Car mileage	Mileage since last oil change	Viscosity at 40°C	Viscosity at 100°C	TAN	TBN	Degree of oxidation	Degree of nitration	Degree of sulfonation	Water content	Glycol content	**Total**
CASTROL MAGNATEC 10W/40	1.	CMD01/Ford Mondeo MK II	diesel	294 000	10 000	X	✓	✓	✓	✓	✓	✓	✓	X	**2 / 9**
	2.	CMD02/Mercedes C220	diesel	195 000	10 000	X	X	✓	✓	✓	✓	✓	✓	✓	**2/ 9**
	3.	CMG03/Ford Mondeo MK II	gasoline	233 000	12 000	X	X	X	✓	X	✓	X	✓	✓	**5 / 9**
	4.	CMG04/Daihatsu Terios	gasoline	181 000	13 000	X	X	X	✓	✓	✓	✓	✓	X	**4 / 9**
	5.	CMG05/Skoda Romster	gasoline +LPG	280 000	15 000	X	✓	X	✓	✓	✓	✓	✓	X	**3 / 9**
		Total				5	3	3	0	1	0	1	0	3	

4. Conclusions

The parameters of in-service engine oils oftentimes vary depending on the operating conditions, number of kilometers traveled (mileage), operating time, technical conditions of the engine and its components. Any changes in the engine oil properties exceeding the lower and upper limit ranges adopted for them bring negative effects in the form of the possibility of damaging the engine or its components [3]. The assessment of the condition of used lubricating oils is based on the in-depth oil analysis. The oil condition is compared with the parameters of a fresh oil and then with the limit values which the oil should not reach. If at least one parameter value reaches the limit, it means that the oil does not function properly in the engine. In order to restore normal operating conditions, it is necessary to take remedial action, most often in the form of oil change. The conducted research made it possible to determine the distribution of the exceedances for the measured parameters of the engine oils tested. The following exceedances have been found: kinematic viscosity at 40°C (70%) and at 100°C (35%), the glycol content (41%) and the Total Acid Number (29%).

The obtained results did not bring an unequivocal answer to the question posed, whether the mileage since the last oil change – generally used to determine the oil change interval – is actually the most reliable criterion. In the case of three vehicles CED08/Skoda Fabia, CED09/Skoda Fabia and CED10/VW Touareg) no exceedances were found, so the oil still retained its useful life although the vehicle user decided to change it. In two other cases one exceedance per vehicle was found, which might suggest that the oil change interval assumed was appropriate. Yet, in over 70% of the samples tested more than one exceedance was detected. Assuming then that the best moment to change oil is when only one of its parameters exceeds the limit value, more than two-thirds of oils tested were actually changed after exceeding the critical point. However, considering the number of these exceedances and the parameters in which the exceedances have taken place, the assessment becomes even more convoluted. Small deviations can only become the basis for further oil monitoring.

Based on the obtained results it may be concluded that considering the vehicle mileage and the mileage since the last oil change, it is impossible to determine the speed of oil degradation. Some vehicles may often be used on highways, and others will be primarily used for urban or even off-road driving. Depending on the operating conditions, the process of oil degradation may be different; and thus, changing those conditions during the car use will be reflected by different speeds of oil degradation. Therefore, the point at which the oil should be changed will also vary. That is why, different time intervals should be used to replace the engine oil depending on the vehicle's operating profile. Such an approach may bring many benefits, the most important of which is the reduction of vehicle maintenance costs.

The research should be regarded as a pilot study, aimed at addressing the basic aspects of the problem. It should be noted, however, that introducing more vehicles and parameters into the study, as well as investigating various driving styles, might make it possible to verify the appropriateness of the oil change standards proposed by manufacturers.

Acknowledgements

The publication was funded by appropriations of the Faculty of Production Engineering University of Life Sciences in Lublin and Faculty of Commodity Science, Cracow University of Economics, within the framework of grants to maintain the research potential.

Bibliography

[1] BASU, A., BERNDORFER, A., BUELNA, C. et al. Smart sensing of oil degradation and oil level measurements in gasoline engines. *SAE Technical Paper*. 2000.

[2] GOMÓŁKA, L., AUGUSTYNOWICZ, A., MACIĄG, A. Analiza stopnia degradacji oleju smarującego w silnikach spalinowych. *Silniki Spalinowe*. 2011, **50**.

[3] IDZIOR, M., WICHTOWSKA, K. Badanie wpływu przebiegu pojazdów na zmiany właściwości olejów silnikowych. *Autobusy : technika, eksploatacja, systemy transportowe*. 2016, **17**(6).

[4] JUN, H.-B., KIRITSIS, D., GAMBERA, M. et al. Predictive algorithm to determine the suitable time to change automotive engine oil. *Computers & Industrial Engineering*. 2006, **51**(4).

[5] KRAL, J., KONECNY, B., KRAL, J. et al. Degradation and chemical change of longlife oils following intensive use in automobile engines. *Measurement*. 2014, **50**.

[6] KRUPOWIES, J. Analiza zmian właściwości użytkowych olejów smarowych firmy BP w czasie ich eksploatacji. *Zeszyty Naukowe Akademia Morska w Szczecinie*. 2006, **10** (82).

[7] KRUPOWIES, J. Badania i ocena zmian właściwości użytkowych olejów urządzeń okrętowych. *Studia Akademia Morska w Szczecinie*. 2009, **49**.

[8] MALINOWSKA, M. Analiza zanieczyszczeń oleju silnikowego stosowanego w silniku Cegielski-Sulzer 3AL25/30. *Zeszyty Naukowe Akademii Morskiej w Gdyni*. 2014, **83**.

[9] SEJKOROVÁ, M., HURTOVÁ, I., GLOS, J. et al. Definition of a Motor Oil Change Interval for High-Volume Diesel Engines Based on its Current Characteristics Assessment. *Acta Universitatis Agriculturae et Silviculturae Mendelianae Brunensis*. 2017, **65**(2).

[10] URZĘDOWSKA, W., STĘPIEŃ, Z. Wybrane zagadnienia dotyczące zmian właściwości silnikowego oleju smarowego w eksploatacji. *Nafta-Gaz*. 2012, **12**.

[11] VASANTHAN, B., DEVARADJANE, G., SHANMUGAM, V. Online condition monitoring of lubricating oil on test bench diesel engine & vehicle. *Journal of Chemical and Pharmaceutical Sciences*. 2015, **9**.

[12] WOLAK, A., ZAJĄC, G. The kinetics of changes in kinematic viscosity of engine oils under similar operating conditions. *Eksploatacja i Niezawodnosc – Maintenance and Reliability*. 2017, **19**(2).

[13] WOLAK, A., ZAJAC, G. Changes in the operating characteristics of engine oils: a comparison of the results obtained with the use of two automatic devices. *Measurement*. 2017, **113C**.

Wojciech Gołębiowski, MSc. – Department of Power Engineering and Transportation at University of Life Sciences in Lublin.

e-mail: *Wojciech.Golebiowski@up.lublin.pl*

Artur Wolak, DEng. – Department of Industrial Commodity Science at Cracow University of Economics.

e-mail: *Artur.Wolak@uek.krakow.pl*

Grzegorz Zając, DSc., DEng. – Department of Power Engineering and Transportation at University of Life Sciences in Lublin.

e-mail: *Grzegorz.Zajac@up.lublin.pl*

Article citation info:
PIELECHA, I., CIEŚLIK, W., SZAŁEK, A. The use of electric drive in urban driving conditions using a hydrogen powered vehicle – Toyota Mirai. *Combustion Engines*. 2018, **172**(1), 51-58. DOI: 10.19206/CE-2018-106

Ireneusz PIELECHA
Wojciech CIEŚLIK
Andrzej SZAŁEK

CE-2018-106

The use of electric drive in urban driving conditions using a hydrogen powered vehicle – Toyota Mirai

Vehicles with electric propulsion systems are increasingly more often equipped with solutions that improve their drive system's efficiency. The latest vehicle model with a fuel cell hybrid system – Toyota Mirai was used in this experiment. The design of this vehicle is similar to that of hybrid vehicles in many aspects. However, new fuel cell technologies are being developed for automotive use, including compressed hydrogen tanks and control systems. The article presents an analysis of a fuel cell operation during vehicle start-up and driving, with particular emphasis on the hydrogen injection strategy of the three fuel injectors used in the fuel cell. The fuel cell interaction with the high-voltage battery has also been characterized. It has been shown that increase in the electrical supply voltage of the vehicle's electric motor can be observed at high torque values of the electric motor. The maximum voltage gain – approximately three times (up to about 650 V) – allows for double the torque of the drive system compared to the standard value.

Key words: *fuel cell, HEV vehicle, hydrogen fuel*

1. Introduction

The transport development strategy, approved for implementation by the European Commission, calls for the reduction of greenhouse gas emissions from the transport sector. Realization of these assumptions with the conventional drive systems will not be possible. Leading car manufacturers, aware of the challenges they face, to work intensively on alternative drives for passenger vehicles. The introduction of a hybrid drive in 1997 by the major car manufacturer, Toyota, was the effect of this new research strategy [8]. The combination of an electric and conventional drive system has made it possible to significantly reduce the atmospheric CO_2 emissions. In the first generation of Toyota Prius the average CO_2 emission was 120 g/km [1] while the latest version of its fourth generation produces merely 70 grams per kilometer [2]. This company estimates that since the introduction of the Prius, the replacement of 10 million conventional-type diesel cars with 10 million hybrid cars has reduced the CO_2 emissions by over 77 million tons. The fact that more and more manufacturers are using hybrid drives in Europe, North America and Asia serves as a confirmation of this drive's potential.

Despite the popularity of this kind of drive system, the requirements set by the European Commission to reduce carbon dioxide emissions will still be impossible to reach. It is only the task of creating a zero-emission vehicle, posed to the car manufacturers, that will eventually allow for the implementation of this transport development strategy. All leading manufacturers want to achieve these goals by putting vehicles with electric drives into mass production. The main issue is: what will be the energy carrier – automotive battery or hydrogen.

Hydrogen as an energy carrier allows a vehicle – at a standard refueling pressure of 70 MPa and a hydrogen mass of 5 kg – to cover a distance up to 550 km. The use of such high pressure requires special tank designs that are already mass-produced. The established hydrogen refueling standards for passenger cars also requires a larger investment in the construction of a hydrogen refueling stations. The main advantage of this standard is the time of refueling 5 kilograms of hydrogen, i.e. filling the tank from 0 to 100% which takes about 3 minutes. This is the main argument for this type of energy carrier, as opposed to the time consuming charging of electric vehicles. The safety of using fuel cell powered vehicles is also supported by the fact that they are actually refueled by drivers without any supervision. The construction of self-service stations was adopted as a standard solution.

Does this energy carrier already provide a clear and unambiguous alternative to conventional propulsion? The hydrogen production process itself is known and popular. It can be produced, from coal, through the electrolysis of clean water, even by composting municipal waste. The challenge remains to find and popularize a method that meets two mutually exclusive criteria: the purity of hydrogen and its price. At present, the cost of hydrogen is about 9 Euro per kilogram, which makes the cost of operation comparable to the operating costs of a vehicle with a 1.8 dm^3 displacement petrol engine.

The widespread use of hydrogen as a source of energy requires, in some parts of the world, the further development of the hydrogen refueling station infrastructure and, in many other parts, building and establishing this infrastructure from scratch.

The use of a high-voltage battery as an automotive energy carrier requires finding a solutions to the fundamental problems of the vehicle's range and battery charging time. Although research aiming to eliminate these problems has been ongoing for over a century, they have yet to be effectively overcome. The latest generation of batteries, not only used by Tesla, provide a range of 150–200 km after just 30 minutes of charging time. The maximum range of the vehicle is up to 450 km, but it takes at least a few hours to charge the battery to full (with three-phase power supply) or even upwards to 30 hours (for normal household use). In order to reach the 200 km range after only 30-minute charging it becomes necessary to use super-fast chargers. Their charging time shortens the full recharge time to 4.5 hours. The power requirement for one station, however, is 480 V/ 200 A×3.

Undoubtedly, the construction of fast charging stations, usually referred to as superchargers, and the use of supercapacitors are currently considered as the best solution for obtaining a large range of the vehicle with a fully charged battery. Nevertheless, this technology also requires the construction of a charging station infrastructure. It is also extremely important to provide energy for the infrastructure to do its job. It is necessary to build a power grid with a very efficient current source – which is also a technical and economic challenge.

For the person owning and driving a car, the important are parameters such as: the price of fuel, the vehicle range, the availability of fuel and the ease of refueling. For the considered energy carriers, the current price and availability of speak for the use of batteries. This is due to the fact that the initiative of construction of the electric vehicle charging infrastructure had already been undertaken as well as the incentive in the form of a reduced cost recharging or even free sources of electricity that have been provided.

By contrast, hydrogen as an energy carrier that is being distributed to fuel cells in the automotive industry has an undoubtful advantage in the form of fast refueling and a much larger vehicle range after refueling. The poor availability of hydrogen refueling stations is due to the very short history of this technology and as a result of its dynamic development. Hydrogen as fuel looks to have a huge future ahead, merely by the fact that it is possible to produce it in the process of waste disposal, and waste is a big problem for our civilization.

Production of the Toyota Mirai vehicles started in Japan in December of 2014, and the sales in the US in the following year. In Europe, the first vehicles were sold in 2015 in Great Britain, Germany and Denmark, and in 2016 also in Belgium. In the same year Toyota Mirai was launched in Norway and Sweden. There are 5 hydrogen refueling stations in Norway. It is estimated that by 2020 there will be more than 20 of them. Sweden has hydrogen refueling stations in Stockholm, Gothenburg and Malmo. Based on Toyota data, it is estimated that 700 hydrogen-powered vehicles were sold in 2015 and about 2,000 in 2016. The sale values are expected to reach about 3,000 vehicles in 2017, with an increase to 30,000 in 2020.

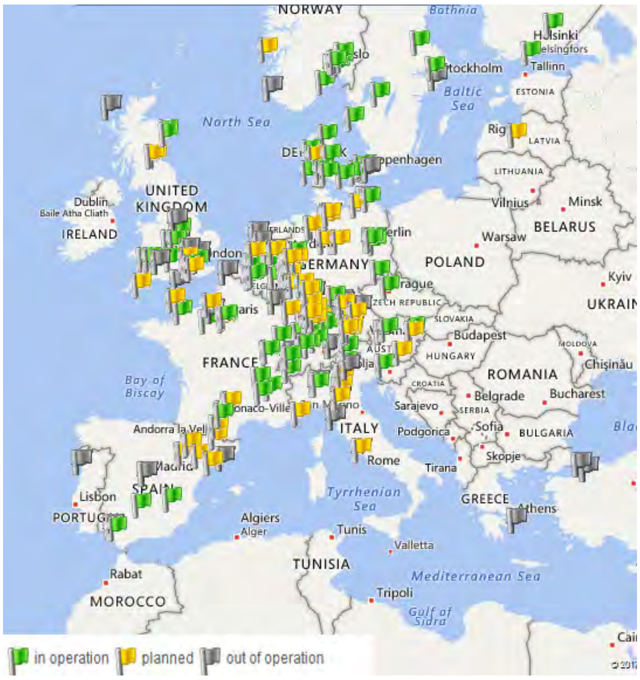

Fig. 1. Map of hydrogen refueling stations in Europe [4]

Two hydrogen tanks with a pressure of 70 MPa were used in the Toyota Mirai vehicle (Fig. 2). Thus the largest unit mass density of compressed hydrogen was obtained. The voltage from the fuel cell stack is converted to 650 volts and fed to the electric AC motor. Technical fuel system data of the vehicle with fuel cells is presented in Table 2.

Table 1. Fuel cell vehicles available on the automotive market

	Toyota Mirai	**Hyundai ix35 Fuel Cell**	**Honda Clarity Fuel Cell**
			
Acceleration 0-60 mph	9.6 s	12.5 s	11 s
Fuel Cell power	113 kW	100 kW	103 kW
Engine power	113 kW	100 kW	130 kW
Top speed	179 km/h	161 km/h	200 km/h
Range	ca. 550 km (NEDC test)	594 km	482 km
H_2 storage	70 MPa	70 MPa	70 MPa

The latest fuel cell drive solutions include more electronic controls than their predecessors. Previous versions of drive development (Fig. 3 – left) had a fuel cell and an inverter that connected directly to the electric motor and fed with the same voltage. The current solution uses a voltage boost, which allows to increase the electric motor supply voltage up to 650 V.

In the new generation of fuel cells, some parts were eliminated and others significantly consolidated, which simplified the whole device structure (Fig. 4).

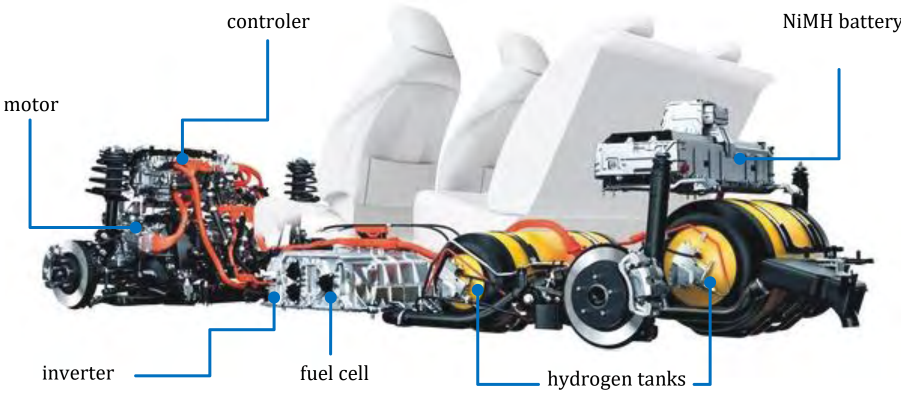

Fig. 2. Components distribution of the Toyota Mirai hydrogen system [6, 7]

Table 2. Toyota Mirai vehicle drive system characteristics [7]

Parameter		Value
Vehicle	mass	1850 kg
	maximum speed	179 km/h
Vehicle range	type approval cycle	approx. 550 km (NEDC test)
Fuel cell	type	PEM (polymer electrolyte)
	power	114 kW
	power density	2.0 kW/kg; 3.1 kW/dm^3
	cell number	370
	humidification	Internal circulation
Electric motor	type	synchronous AC
	maximum power	113 kW
	maximum torque	335 N·m
Battery	type	NiMH
Hydrogen storage	volume of tanks pressure/mass	front – 60 dm^3, back – 62,4 dm^3 70 MPa/5 kg H_2
Refueling	time	3 min

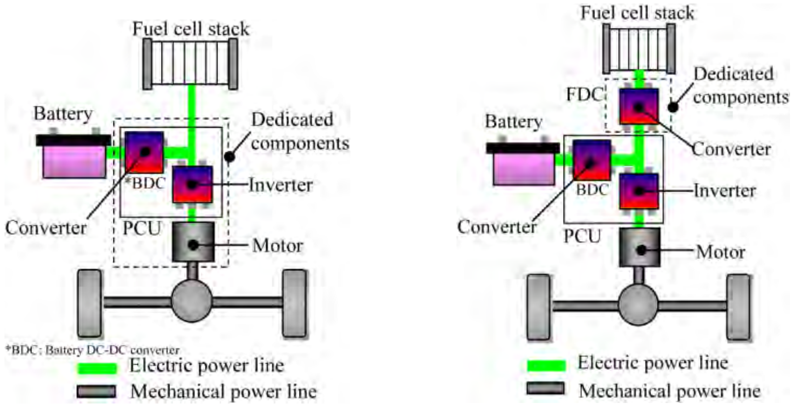

Previous version Mirai system

Fig. 3. Generations of Toyota vehicles fuel cell configuration [3]

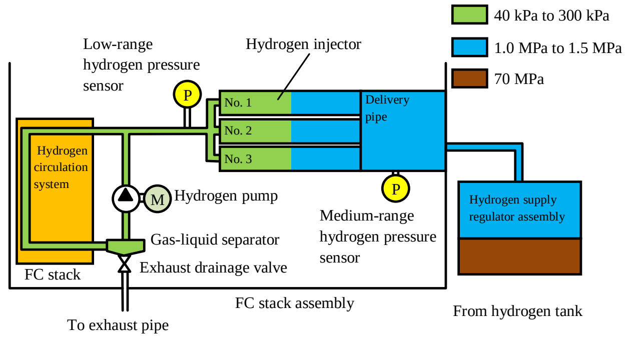

Fig. 4. The fuel cell power supply system schematic [5, 9]

Toyota Fuel Cell System (TFCS) is the world's first fuel cell system without an external humidifier. The fuel cell stack control and the control system was refined so that the water formed at the bottom of the cathode was transported to the front of the upper cathode part via internal circulation through the anode. The characteristic feature of the fuel cell system used in the tested vehicle is the three hydrogen injectors, that operate depending on the load on the system and their operation is the basis for the analysis carried out in the article.

Figure 5 shows the possible driving modes of the first mass-produced fuel cell vehicle. These modes are analogous to modes in hybrid vehicles, except that the function of the energy generator is to fill the fuel cell stack (as opposed to the diesel engine in HEV vehicles). The modes are: standstill loading, starting, normal driving, braking (energy recovery) and acceleration. Block diagrams indicate the systems used to drive the vehicle when in the driving mode. Two directions of energy flow are possible: the use of energy – in the form of hydrogen or electricity stored in a high-voltage battery, and the recovery of energy to charge the HV battery.

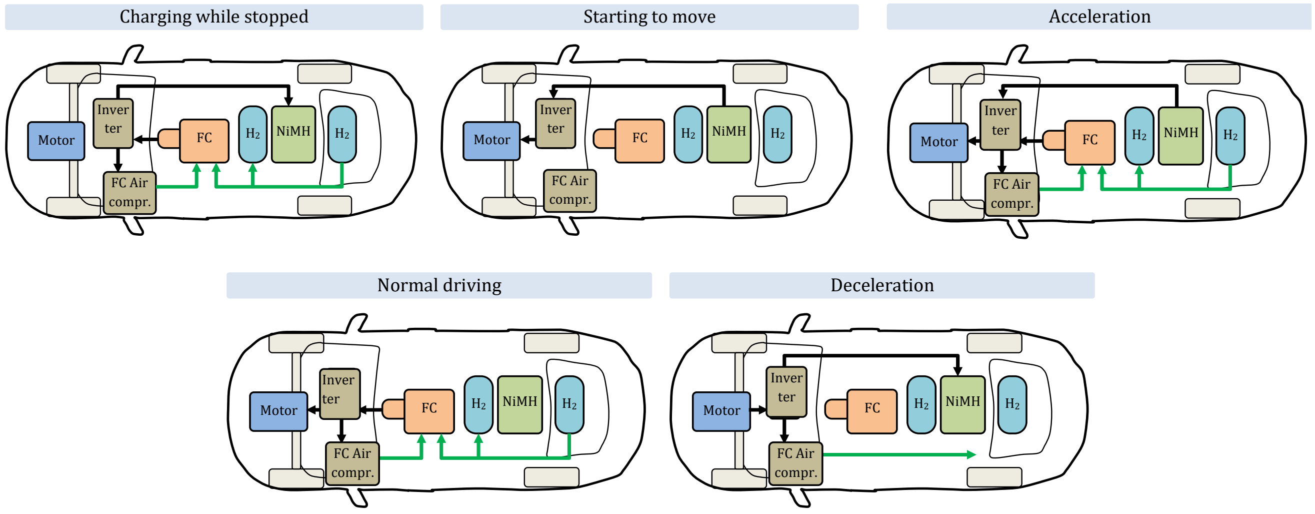

Fig. 5. Drive mode of Toyota Mirai [6]

2. Fuel cell tests

The aim of the fuel cell tests for the vehicle was to analyze the operating conditions of the fuel cell in relation to its power supply. Due to the use of three hydrogen injectors in the supply system, the control method was interesting.

The study was conducted in several vehicle operating states, in each case analyzing:

a) starting the fuel cells,
b) standard operating conditions of a fuel cell,
c) cooperation of the fuel cell with energy storage systems.

3. Fuel cell start

The fuel cell analysis was performed during the first test drive of the Toyota Mirai vehicle in Poland (the vehicle mileage was approximately 3,000 km at the time). Because of the limited amount of hydrogen and the short time of vehicle availability, the study was performed during the vehicle presentation in Warsaw. Drive data registration was based on the use of diagnostic monitors (FC – Fuel Cell and FCDC – Fuel Cell Direct Current) implemented in the OBD system. Recording of selected cell parameters from the presented diagnostic monitors was done using an OBD connector and a computer equipped with TechStream software. The number of recorded parameters affects the frequency of data recording. In the presented studies this frequency was:

– 8 to 20 Hz when recording 51 parameters of the FC monitor,
– 8 to 16 Hz when recording 91 parameters of the FCDC monitor.

The Toyota Mirai vehicle drive system analysis was performed in fuel cell start-up conditions. The first 20 seconds of operation after the system start were analyzed.

The fuel cell start-up began from the state of being switched off completely (as seen by the level of minimum voltage in Fig. 6). Within seconds (2–3 seconds), the value of the voltage generated by the cell stack was 315 V with a current of 32 A. The rated power (10 kW) is 10% of its maximum power. After a 10 second period, the current generated from the fuel cell increased (up to 40 A), which increased the power to about 13 kW. These conditions require only hydrogen injection by one injector placed in the power supply (Fig. 4).

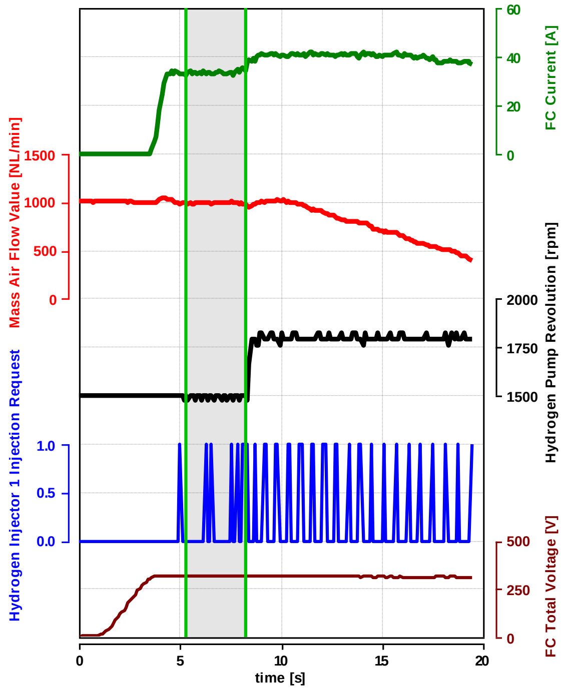

Fig. 6. Changes in fuel cell operating parameters during start-up (vehicle stopped)

Maintaining the operating parameters of the cell after its start-up requires an increased rotational speed of the hydrogen pump (from 1500 to 1800 rpm) and a much higher frequency of hydrogen injection by the injector 1. The supply of hydrogen is performed at a pressure of 122 kPa and the air pressure is maintained at 100 kPa.

4. Fuel cell driving operating conditions

4.1. Analysis of a fuel cell operation

The drive operation evaluation began with an analysis of the test vehicle traffic conditions. Figure 7 shows the comparison of the conditions of the four Toyota Mirai routes. For three of those routes (routes 1, 2 and 3) the maximum traveling speeds are comparable and reach 50 km/h. On these routes the time spent stationary is also close in value (equal to 50% of the total test time) – Fig. 7a. Route 4 is characterized by an increased maximum vehicle speed. The test duration values are varied and range from 160 to 330 seconds respectively. The analysis of the time density of three driving phases, divided into: driving without acceleration (a = 0), acceleration (a > 0) and braking (a < 0) indicates that each drive had a similar driving parameters. In particular, routes 1–3 have a time density of up to 10% at constant speed and about 20% at acceleration and deceleration each.

The fuel cell power analysis shown in Fig. 8 during vehicle acceleration indicates a high level of its performance.

Maximum power of the fuel cell during acceleration is reached after 3.5 seconds. Hydrogen injectors are switched on gradually with the power demand. The third injector was used only after obtaining about 70 kW cell power generation. With the increase in electric current, the maximum voltage of the cell is reduced, which is in line with the typical characteristics of its operation. Resistance losses then increase, thus limiting the voltage value when increasing the current output [5]. The maximum current of the cell is 468 A at 244 V. The vehicle speed under these conditions was only 40 km/h.

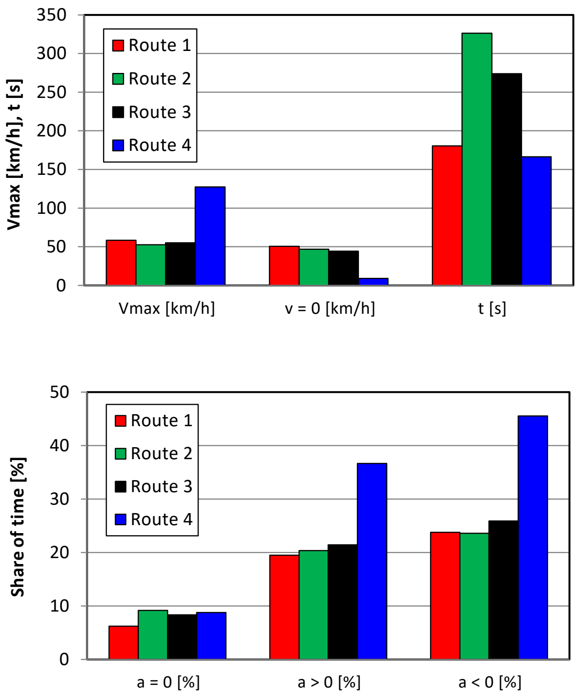
a)

b)

Fig. 7. Road test results of the Toyota Mirai vehicle: a) the vehicle speed, b) the vehicle acceleration time density (excluding the vehicle being stationary)

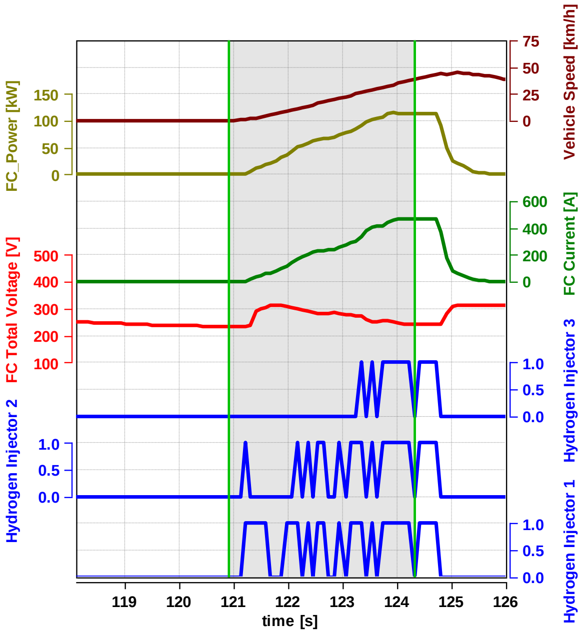

Fig. 8. Example of changes in hydrogen fuel supply (three injectors) against speed variations (average speed) of driving a Toyota Mirai (route 1)

The analysis of the hydrogen injectors operation relative to the driving conditions is shown in Fig. 9. For each test run of different instantaneous speeds and the resulting accelerator pedal position, the work of the individual hydrogen injectors is shown. On this basis, the use of injectors was evaluated based on the position of the accelerator pedal. It was assumed that this value was proportional to the load on the propulsion system.

The analysis was conducted for several acceleration pedal positions: 0%, 0-25%, 25-50%, 50-75%, and 75-100%. Data obtained from this analysis indicate the use of two injectors mainly. The third injector is only used during the final range of accelerator pedal position.

The results shown in Fig. 9 indicate the low speed of the vehicle forcing the third injector to operate.

An analysis was also carried out to summarize the effect of the speed and load on the operating conditions of hydrogen fuel injectors in the fuel cell. Injectors 1 and 2 are operated at each tested vehicle speed and for loads ranging from 0 to 100% (Fig. 10). The use of injector no. 3 is only required for loads exceeding 60%, which were respective of vehicle speeds in the range of 25 to 130 km/h.

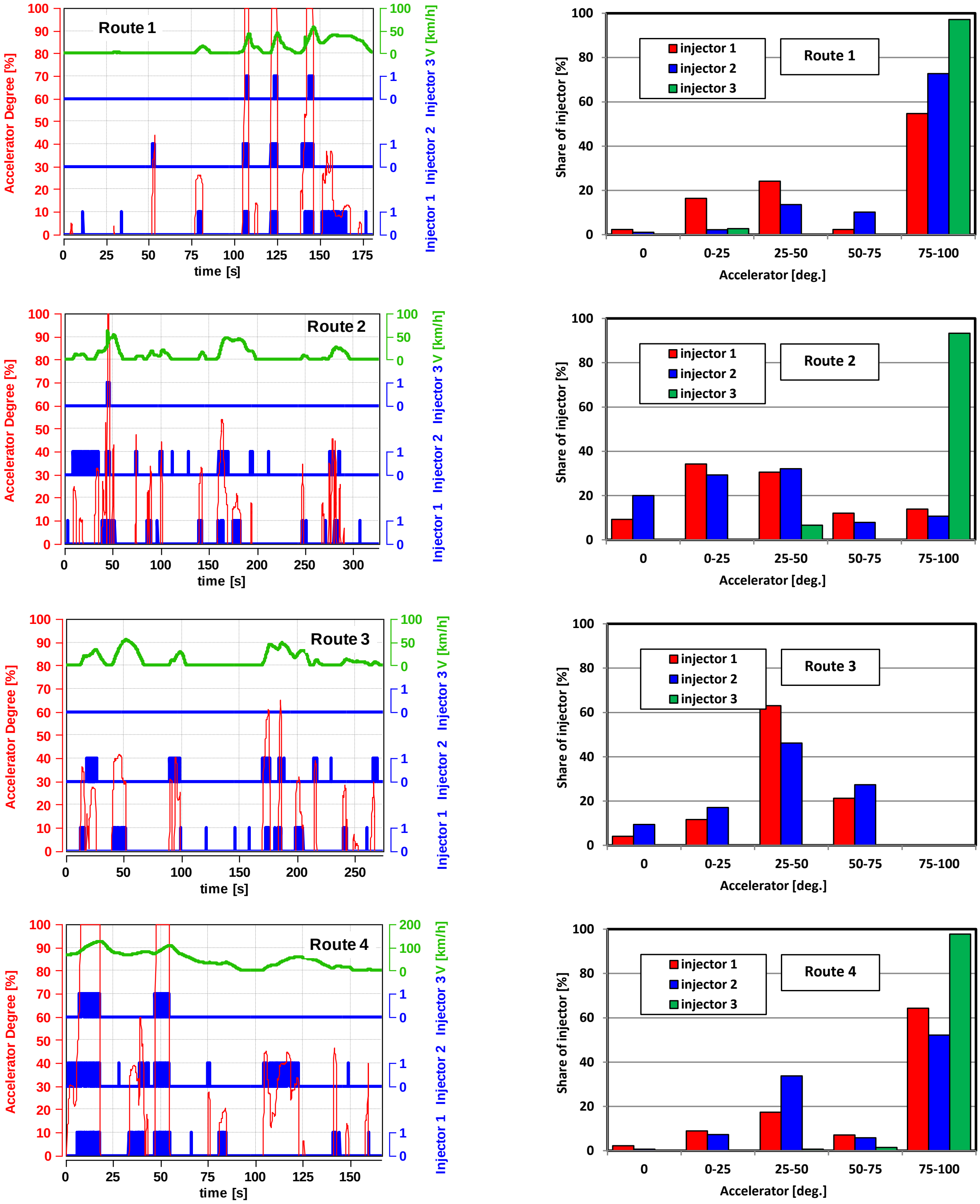

Fig. 9. Analysis of the fuel cell hydrogen power supply conditions by three injectors, along with the injector operating time densities (accelerator pedal positions)

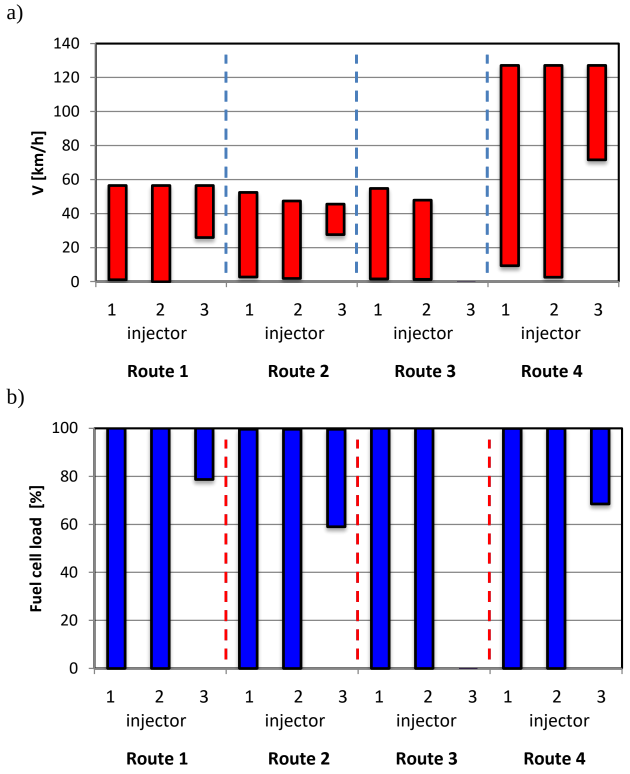

Fig. 10. The influence of vehicle speed (a) and fuel cell load (b) on operating conditions of the hydrogen fuel injectors in the fuel cell

3.2. The interaction of fuel cell and high-voltage battery

The hydrogen drive configurations shown in Fig. 3 indicate that the current systems will use so-called boosts (analogous to hybrid drives) to increase the voltage applied to the electric motor. The fuel cell DC-DC converter (FDC) increases the voltage from the fuel cell up from a maximum of 315 volts to 650 volts. This arrangement allows to double the power of the electric motor driving the vehicle. The conditions for this voltage gain during the operation of the Mirai Toyota system are shown in Fig. 11. It is evident that during vehicle acceleration, the input voltage to the FDC achieves a maximum value (about 315 V), while the output of the converter is above 600 V. Additionally, the high-voltage battery operation is noted to aid the fuel cells – discharging during acceleration (positive current values) and charging during most braking maneuvers. Despite varying driving conditions, the battery charge level is maintained at 52–62%. This level of charge is also used in hybrid vehicles, which extends the battery lifetime.

Based on the above relationships, the HV battery operating conditions have been analyzed. According to Fig. 12a, the charging of the battery is carried out at increased voltage to about 315 V (fuel cell operating voltage). Significant battery charge time applies to small charging currents up to 50 A. Its discharge consists in using a current of up to 20 A, however, the maximum values exceed 120 A.

The electric motor operating conditions indicate the use of its full characteristics (Fig. 12b). Regenerative braking mainly occurs in areas of small torque values and in the range of average speeds.

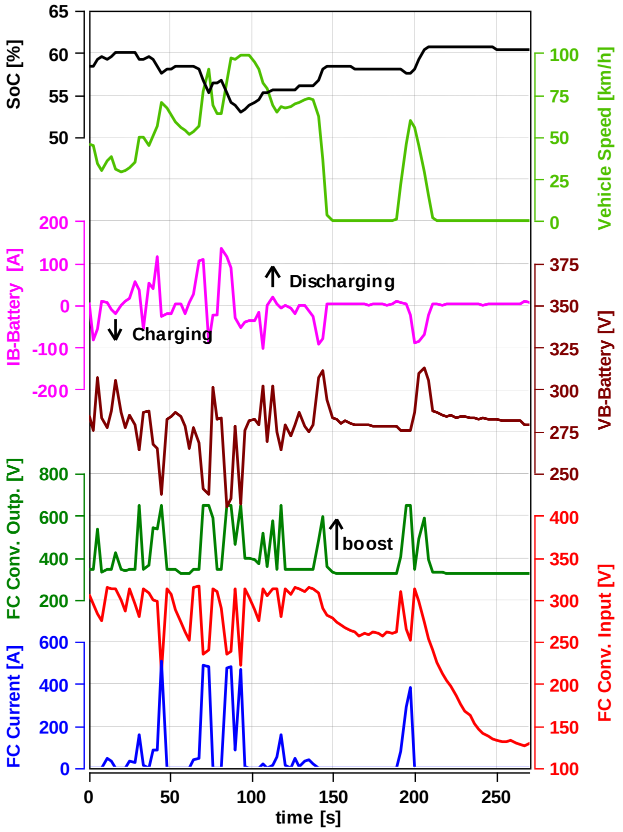

Fig. 11. Operating conditions for the voltage boost circuit for the voltage generated by the fuel cell

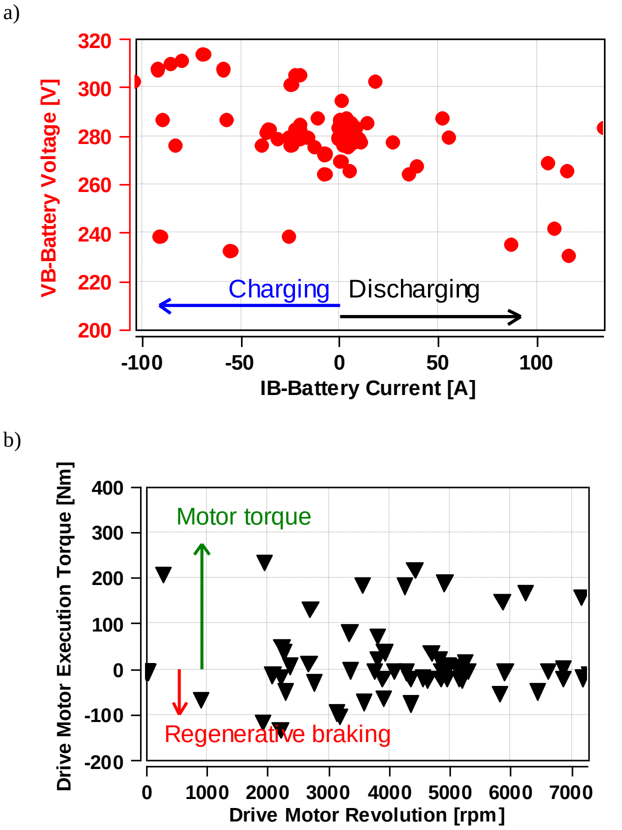

Fig. 12. Operating conditions of the systems: a) high-voltage battery, b) electric machine acting as a motor or generator

4. Conclusions

The Toyota Mirai is the first mass-produced vehicle to feature three independent fuel cell hydrogen injectors. An analysis of the fuel cell system in the vehicle in typical traffic conditions allows to pinpoint the key aspects of this system's operation:

1. The maximum value of the fuel cell voltage (315 V) when moving from zero is obtained after approximately 4 seconds during the vehicle start-up.
2. The full power of the fuel cell for vehicle acceleration is available after about 3.5 seconds after the vehicle has stopped (fixed operating conditions of the fuel cell).
3. The use of three hydrogen injectors allows for a wide range of possible ways of obtaining the desired flow of hydrogen for the fuel cell supply; The third injector is activated only during a high fuel cell load values at 75-100% of the accelerator pedal position. Analysis of the results indicates that the third injector is only running at speeds exceeding 35 km/h.
4. Equipping the power management system with a voltage boosting circuit for the electric motor power supply allows the voltage to be increased from 315 V to 650 V. The driving conditions that necessitate the operation of the so-called boost is rapid acceleration of the vehicle regardless of the charge level of the high-voltage battery.

Due to the limited time availability of the vehicle for the study future research will be conducted on both the chassis dynamometer in the standardized NEDC test as well as in real vehicle driving conditions at comparable distances. Then the results of the study will be comparable with the results from hybrid vehicles already tested by the Authors. This analysis will allow for a complete assessment of the propulsion system's energy consumption relative to other vehicles. The limitation in carrying out such tests is, however, that there is currently no infrastructure for refueling such vehicles in Poland.

The study presented in this article was performed within the statutory research (contract No. 05/52/DSMK/0265).

Acknowledgements

The authors would like to thank Toyota and Lexus Academy in Toyota Motor Poland Company Sp. z o.o. in Warsaw for their provision of an vehicle for testing.

Nomenclature

a	acceleration	IB	battery current
AC	alternating current	NiMH	nickiel hydride battery
CO_2	carbon dioxide	OBD	on board diagnostic
FC	fuel cell	TFCS	Toyota Fuel Cell System
FCDC	fuel cell direct current	v	speed
FDC	fuel cell direct current converter	Vmax	maximum speed
HEV	hybrid electric vehicle	t	time
HV	high voltage	VB	battery voltage

Bibliography

[1] Approval of a vehicle Toyota Prius: e11*98/14*0131*04.

[2] Approval of a vehicle Toyota Prius: e11*2007/46*2971*01.

[3] HASUKA, Y., SEKINE, H., KATANO, K., NONOBE, Y. Development of boost converter for Mirai. *SAE Technical Paper*. 2015, 2015-01-1170.

[4] Hydrogen Filling Stations in Europe www.netinform.net/H2/H2Stations (accessed 17.03.2017).

[5] KOJIMA, K., SEKINE, S., Development trends and scenario for fuel cell vehicles. *Toyota Technical Review*. 2011, **57**(2), 39.

[6] MERKISZ, J., PIELECHA, I. Układy elektryczne pojazdów hybrydowych. *Publishing House Poznan University of Technology*, Poznań 2015.

[7] Outline of the Mirai. www.toyota-europe.com (accessed 14.03.2017).

[8] The Hybrid that Started it All. www.toyota-global.com (accessed 15.03.2017).

[9] YUMIYA, H., KIZAKI, M., ASAI, H. Toyota Fuel Cell System (TFCS). *EVS28 International Electric Vehicle Symposium and Exhibition*. Korea, 3-6.05.2016.

Prof. Ireneusz Pielecha, DSc., DEng. – Faculty of Machines and Transport of Poznan University of Technology.

e-mail: *Ireneusz.Pielecha@put.poznan.pl*

Wojciech Cieślik, MEng. – Faculty of Machines and Transport in Poznan University of Technology.

e-mail: *Wojciech.Cieslik@put.poznan.pl*

Andrzej Szałek, DEng. – New Technologies Expert, Toyota and Lexus Academy, Toyota Motor Poland.

e-mail: *Andrzej.Szalek@toyoyta.pl*

Article citation info:
KOWALSKI, J. The influence of the fuel spray nozzle geometry on the exhaust gas composition from the marine 4-stroke diesel engine. *Combustion Engines*. 2018, **172**(1), 59-63. DOI: 10.19206/CE-2018-107

Jerzy KOWALSKI

CE-2018-107

The influence of the fuel spray nozzle geometry on the exhaust gas composition from the marine 4-stroke diesel engine

The paper presents experimental research on a 4-stroke, 3-cylinder, turbocharged AL25/30 Diesel engine. Research consisted in investigating the effect of the geometry of the fuel injectors on the exhaust gas composition from the engine. During measurements, the engine was operated with a regulator characteristic of a load range from 40 kW to 280 kW, made by electric water resistance. The engine was mechanically coupled to the electric power generator. Three observations were made for each engine load, operating with fuel injectors of varying geometry. All considered types of injectors were installed on all engine cylinders. Mentioned injectors differed in the size of the nozzle holes diameters, holes numbers and angles measured between the holes axis. Engine performance data were recorded with a sampling time of 1 s. Cylinder pressure and fuel injection pressure on the front of each injector were collected also. The composition of the exhaust gas was measured using an electrochemical analyzer. According to the results, the change of fuel nozzle geometry results in a change in fuel spraying and evaporation and consequently changes in the course of the combustion process. The effect of this is the change of the composition of the exhaust gas.

Key words: *marine Diesel engine, fuel injector geometry, combustion process, exhaust gas composition, emission*

1. Introduction

Diesel 4-stroke engines are used on ships both for main propulsion and as power generators, including emergency generators. The source of energy in such engines is the combustion process of liquid fossil fuels and the side effect is the emission of toxic compounds including carbon, sulfur and nitrogen oxides into the atmosphere. In the classic construction of marine Diesel engines, the fuel is delivered to each engine cylinder directly using multi-hole fuel injectors. The fuel dosage, its delivery time to the cylinder and the injection timing are regulated by the injector opening pressure and the regulation of the Bosch type fuel pump. In modern Diesel engines constructions, fuel delivery parameters can be controlled by electronic control systems and electromagnetic or piezoelectric valves in a fuel injector (common-rail systems). The main purpose of the fuel dose regulation is the reduction of the fuel consumption and the reduction of emissions of toxic compounds into the atmosphere for the entire engine load range. Fuel injected into the combustion chamber of the engine is broken-up and evaporated and mixed with air at the same time. The rise in temperature and pressure of the fuel and air mixture compressed by the piston causes it to auto-ignite in areas where the composition of the mixture is within its flammability limits. As a result of auto-ignition, flame propagation occurs in the combustion chamber. Note that the described processes occur simultaneously and their course is determined by the shape of the injected fuel spray [1]. The shape of the fuel spray depends on the pressure of the injected fuel, the pressure in the engine cylinder (back pressure), and the position and geometry of the fuel nozzle. Typically, the diameter of fuel injector holes is determined by the fuel pressure in the fuel system. The increase of fuel injection pressure to the cylinder results in an increased intensity of atomization and evaporation, but also an increased fuel dose penetration [2]. Reducing fuel injection holes reduces the initial diameter of fuel droplets, which promotes the intensification of fuel atomization and the evaporation [3], and prevents fuel from burning on cylinder walls. The effect of this phenomenon is shortening the auto-ignition delay [4]. It should be noted, that reducing the diameter of the fuel nozzle holes reduces their cross-sectional area. In the case, in classic construction with the Bosch pump, the reduction of the diameter of the fuel nozzle holes, with unchanged quantitative characteristics of the injection pump causes the increase of the injection pressure. In the case of common-rail systems, the reduction in the diameter of the holes results in the decrease of the fuel flow rate through the nozzle holes with relatively stable fuel rail pressure. We may counteract both phenomena by changing the number of holes in the injector. The increase of the number of holes in the nozzle promotes homogeneous combustion. Excess number of holes in the injector can cause overlap the fuel spray. Based on the study [5], it can be concluded that there is a minimum distance between fuel sprays for which the fuel evaporation is the most intense. The value of the angle of the fuel injection cone is also affected by the fuel combustion process. Too high value of this angle causes the fuel evaporation and combustion near the cylinder head walls and cylinder valves. Decreasing the value of the mentioned angle causes fuel injection towards the piston head. Moreover, according to [6], changing the fuel injection cone angle causes the change of the fuel flow rate from the nozzle.

Mentioned conditions have a significant impact on the composition of the exhaust gas. For example, according to [7] the increase of the fuel injection cone angle results in the increase of the nitric oxides (NO_x) fraction, while according to [8] the increase of the number of holes does not significantly affect the NO_x emission. A thorough analysis of this problem, based on the 3-dimensional CFD model of the combustion process, can be found in [9] and [10].

The presented analysis shows that the geometry of the fuel injector nozzle has a significant effect on the composition of the exhaust gas. Unfortunately, there are very few publications on this topic, based on experimental research on marine engines. Therefore, the aim of the study is to analyze the parameters of the combustion process in the 4-

stroke Diesel engine with the assessment of exhaust gas composition. The analysis will be carried out on the basis of the experimental results of the operating parameters and emission from the engine used in the marine applications.

2. Measurement conditions and the research object

The research object is Sulzer's 3-cylinder, 4-stroke AL25/30 Diesel engine. The engine is pulse charged by the VTR 160 Brown-Boveri turbocharger and intercooled. The fuel is diesel oil with a known specification, presented in Table 1. The fuel system consists of Bosch-type injection pumps controlled by a rotary speed control and multi-hole fuel injectors, mechanically adjustable by opening pressure. Fuel injectors are centrally located in the cylinder heads of the engine. The engine operated at a constant rotational speed of 750 rpm and was loaded by the power generator, electrically connected to the water rheostat. The basic parameters of the laboratory engine are presented in Table 2 and the schematic of the laboratory stand is presented in Fig. 1. During each observation, the engine was loaded to a value of 280 kW, determined by the electric power output from the electric power generator. Recordings of measurement results were made in quasi-steady conditions. It is assumed that mentioned conditions occur when the changes of the exhaust gas temperature measured behind the turbocharger was not greater than 1°C/min. Then the engine load was reduced by 20 kW and the measurement procedure was repeated. The measurements were conducted in the load range from 280 kW to 40 kW. Three observations were made during each engine load for variable geometry of fuel nozzles installed on all engine cylinders. Parameters of used fuel nozzles are presented in Table 3.

Table 1. Diesel oil properties

Parameter	Unit	Value
Density at 15°C	kg/m^3	823.6
Viscosity at 40°C	mm^2/s	2.57
Cetane number	–	52.9

Table 2. AL25/30 engine parameters

Parameter	Unit	Value
Rotational speed	rpm	750
Cylinder number	–	3
Cylinder diameter	mm	250
Stroke	mm	300
Compression ratio	–	12.7
Fuel nozzle opening pressure	MPa	25
Injection timing	°before TDC	18

According to Table 3 nozzles 1 and 3 differ in the fuel nozzle cone angle. The change of the diameter of holes can be considered negligible. Nozzle 2 has a reduced number of holes and an increased diameter in relation to the rest of the nozzles. The changes made resulted in a total cross section area of the nozzle 2 being 22% greater than in the nozzle 3. Combustion pressures were measured in all engine cylinders by the Kistler 6613CG1 sensors with an amplifier. Each observations consists of 7 revolutions of the engine crankshaft with sampling rate of 720 samples per shaft rotation. Fuel pressure on the front of fuel injectors was recorded by Kistler 4067E2000DS1-2.0 sensor with digital temperature compensation. In addition, temperature and pressure of the charging air, the exhaust gas, lubricating oil and cooling water of the high temperature circuit were measured at characteristic points of the engine installation. Moreover, the composition of the exhaust gas was recorded using the TESTO 350XL electrochemical gas analyzer. The air flow rate was calculated on the basis of the pressure drop measurements on the Ventouri flowmeter installed on the air intake duct. The range and accuracy of used measuring equipment are presented in Table 4.

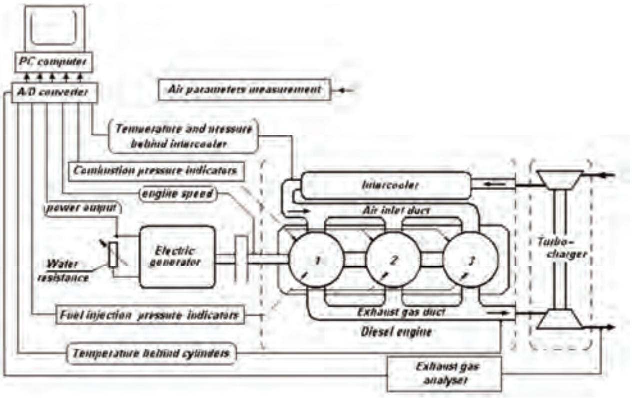

Fig. 1. The experimental setup schematic [11]

Table 3. Fuel nozzles parameters

Nozzle	Nozzle 1	Nozzle 2	Nozzle3
Holes number	9	8	9
Holes diameter [mm]	0.325	0.375	0.320
Nozzle holes angle [°]	150	158	158

Table 4. Ranges and precisions of measurement equipment

Parameter	Range	Precision values
Environment air temperature	0–60°C	±0.5°C
Environment air humidity	0–90%	±2.0%
Exhaust gas temperature	0–650°C	±1.35%
Carbon oxide	0–10000 ppm	±5.0%
Sulfur dioxide	0–5000 ppm	±5.0%
Nitric oxide	0–3000 ppm	±5.0%
Nitric dioxide	0–500 ppm	±5.0%
Carbon dioxide	0–50%	±0.5%
Oxygen	0–25%	0.8%
Temperatures	0–100°C	±0.35%
Pressures	0–4 bar	±0.3%
Fuel injection pressure	0–2000 bar	±0.8%
Combustion pressure	0– 50 bar	±2.0%
Fuel consumption [kg/h]	–	±3.0%
Electric power [kW]	–	±0.5%

3. Results and discussion

According to discussed considerations, the increase in the total cross-sectional area of the injector holes (nozzle 2) in the classical construction of the fuel system results in the reduction of fuel injection pressure. Figure 2a shows an example fuel pressure measurement on the front of the injector during operation of the engine with a load of 280 kW. According to the presented results, fuel pressure characteristics are not significantly different for different spray geometries. However, it should be noted that the sampling frequency of the pressure measurement is 720 measurements per crankshaft rotation. According to [9] the increase of the diameter and the number of fuel nozzle causes the reduction of the maximum combustion pressure. Figure 2b shows an example of the pressure characteristics measured on the indicator gap during operation of the engine with a load of 280 kW. According to presented results, the use of nozzles 2 and 3 results in the reduction of the maximum combustion pressure by about 0.5 MPa. Figure 3 presents the calculated values of specific fuel consumption (SFC) and air/fuel excess ratio. According to the presented results, the use of nozzle 3 reduces the fuel consumption by average 2.8% for all considered loads of the engine. This means that the fuel injection cone angle of 158° is the preferred solution to reduce the fuel consumption for this combustion chamber design. The worst solution in the point of fuel consumption is the nozzle 2. The increase of the diameter of the fuel nozzle holes, and limiting theirs numbers probably increases the intensity of the evaporation and the combustion process. This leads to the reduction of maximum pressure and temperature of the combustion process. It should be noted that the value of the air/fuel excess ratio, determined by the measuring the oxygen content in the exhaust gas, does not change significantly. Certain small changes are only visible when the engine operates at relatively low load.

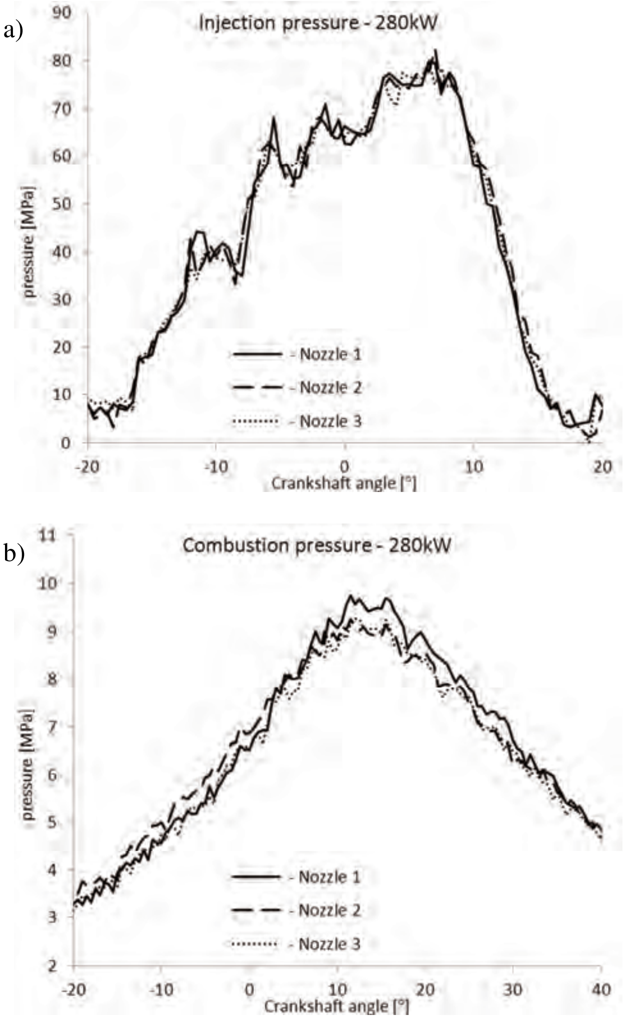

Fig. 2. The example of a) fuel injection pressure and b)combustion pressure

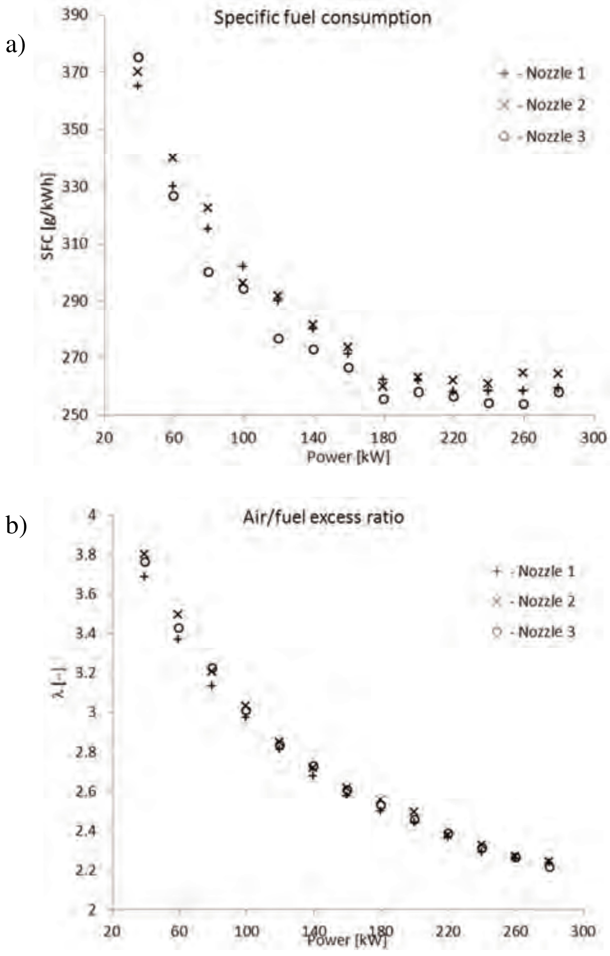

Fig. 3. Specific fuel consumption and the air/fuel excess ratio

Interesting is fact, that the use of nozzles with the geometry of Table 3 does not cause significant changes in the exhaust gas temperature measured behind the cylinders and in the front and behind the turbocharger. The use of the nozzle 2 causes the rise of exhaust gas temperature by a value not higher than 5°C and only when the engine operates with the maximum considered load. This is the evidence of the theory of the combustion process extension. For a relatively heavy load and the nozzle 2, the 2% increase of the airflow was also observed. No turbocharger speed changes and the charging air pressure changes were observed. However, the changing of the geometry of the fuel nozzles results in significant change in the composition of the exhaust gas. Figure 4 shows results of the measurement of the exhaust gas composition. The small change in the fuel consumption entails changes in the carbon dioxide (CO_2) content in the exhaust gas. Despite the smallest SFC was observed for nozzle 3, the smallest CO_2 fraction in the exhaust gas was measured for the operation of the nozzle 2. The carbon monoxide (CO) content was also higher for the nozzle 3, especially when the engine operates at a relatively high load. According to the presented results, the use of nozzle 1 results in the highest CO content in the exhaust gas. The difference in CO fraction during engine operation with a relatively high load was even 50%. Based on the results from [9] it can be stated that the reason for this is the smaller value of the fuel injection cone angle in nozzle 1.

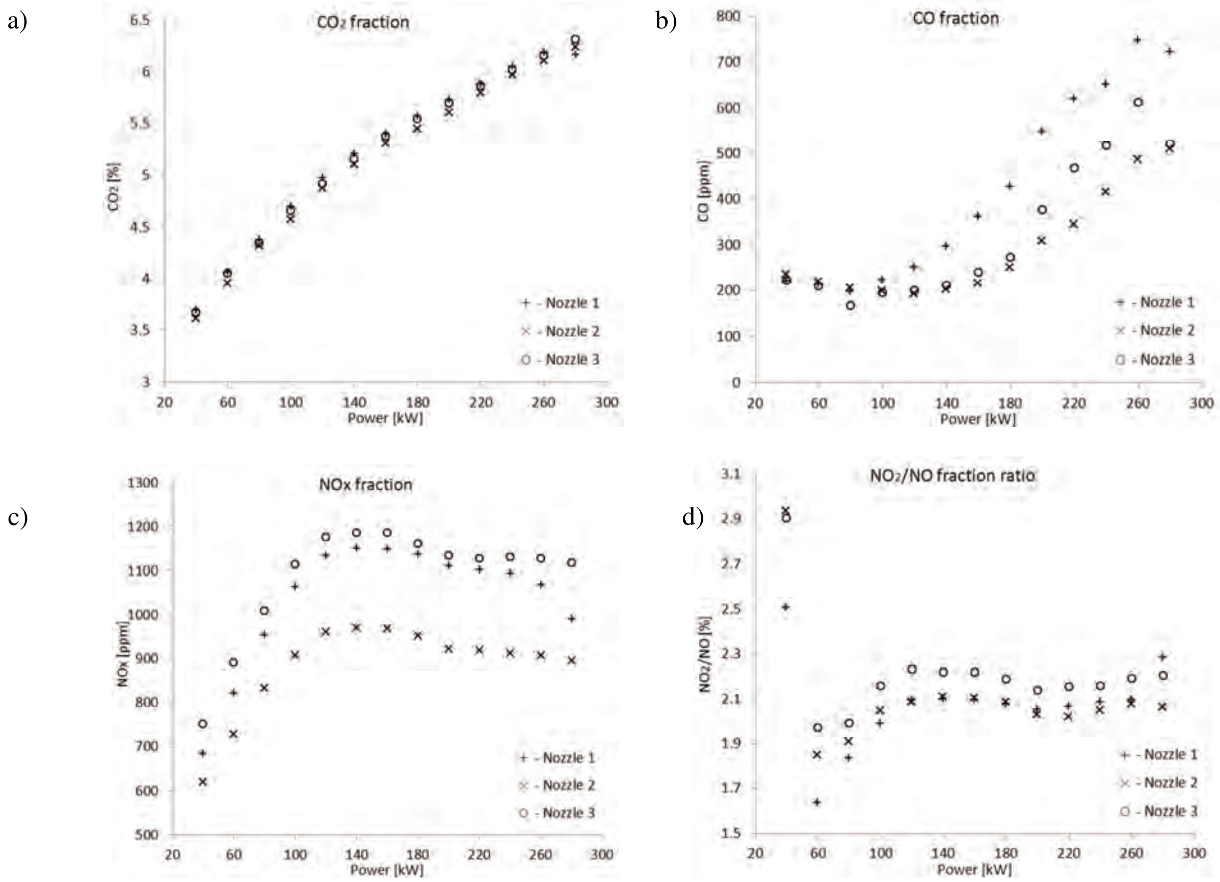

Fig. 4. Fractions of chosen chemical compounds in the exhaust gas

Figure 4c and Figure 4d show the nitric oxides fractions in the exhaust gas as a sum of nitric dioxide (NO_2) and nitric oxide (NO) and the ratio of NO to NO_2. According to the presented results, the use of the best nozzle from the fuel consumption point of view (nozzle 3) increases the NO_x fraction in the exhaust gas. This may be due to the increase of combustion temperature, but this conclusion must be taken with the great care due to the lack of appropriate measurement data. The smallest NO_x fraction was observed for nozzles 2. This result is consistent with the results of the CFD calculations for the same research object [9]. The increase of the diameter of the fuel nozzle holes and the reduction of the number of holes helps to reduce the NO fraction in the exhaust gas. It should also be noted that the use of nozzle 3 results in the increase of the NO_2 fraction in the exhaust gas. During the study, NO_x and CO emissions were also calculated. Figure 5 shows the CO and the NO_x emission. The NO_x emission value was corrected to the standard pressure, humidity and ambient conditions in accordance with the ISO 8178 standard regulation.

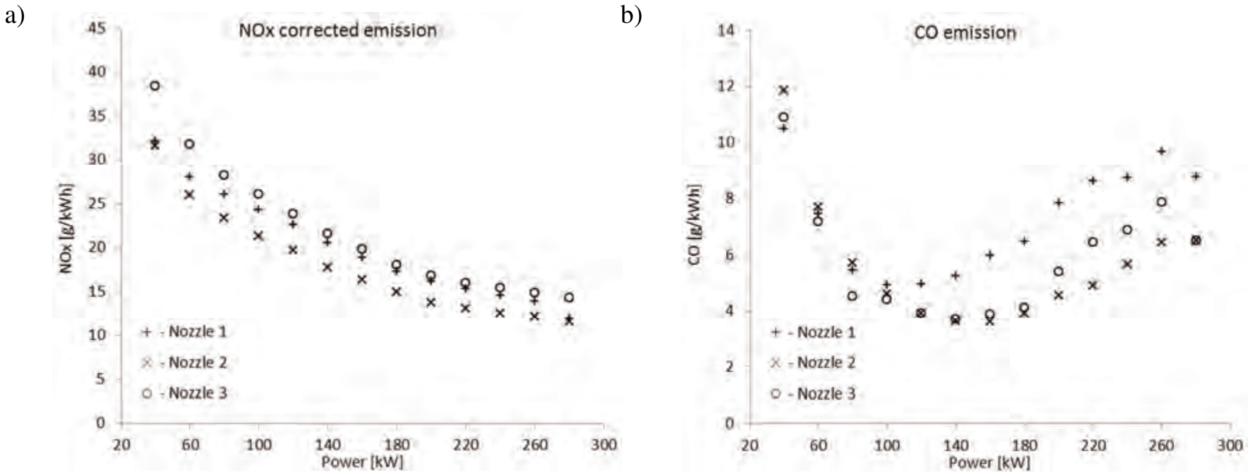

Fig. 5. Emission of the NO_x and the CO

According to the results presented in Fig. 5, the highest NO_x emission is observed during the operation of the nozzle 3 and the smallest for the nozzle 2. The reduction of NOx emission for nozzle 2 is from 21.3% to 24% for all considered loads of the engine in relation to results for nozzle 3. It should be noted that fuel nozzle 2 has the smallest number of holes with the largest diameters. As a result, the process of the evaporation and the combustion of the fuel are extended relative to the remaining geometry of nozzles. As a result, temperature and pressure of the combustion process are reduced, thus reducing NO_x emission and increasing of the fuel consumption. Obtained results of the NO_x emission are qualitatively convergent for experimental results with the use of diesel oil [12]. The increase of the diameter of the holes and the reduction the holes number causes the reduction of NO_x emission and the increase of SFC. According to results of Fig. 5b, the highest CO emission is obtained for the nozzle 1. The visible increase of emissions is evident especially during high load operation. As a result of this situation, may be fuel combustion near relatively cold cylinder walls due to too low fuel injection cone angle.

Conclusions

The paper presents the results of experimental research on the effect of changes of fuel nozzle geometry on performance parameters and emission from marine 4-stroke Diesel engine. Obtained results show that, from the engine efficiency point of view, the best solution is to use lower diameter of nozzles holes with larger numbers of holes, as is the case in the nozzle 3. The use of this solution intensifies the atomization and evaporation process. The combustion process in this case is faster, which in consequence leads to higher combustion temperature and pressure and reduced fuel consumption. However, this regulation of the combustion process leads to an increase in the NO_x emission. Reduction of the NO_x emission is possible by slowing down the combustion process. Therefore, from the point of view of the reduction of NO_x emission, it is preferable to use fuel nozzles with larger holes diameter with a limited number of holes. Such a configuration occurs in the nozzle 2. The analysis of results showed that for the shape of the combustion chamber of the test engine, a better solution is to use a higher fuel injection cone angle. In this case, the combustion takes place away from the cylinder walls, resulting in lower the CO emission.

Bibliography

[1] KIM, H.J., PARK, S.H., LEE, C.S. Impact of fuel spray angles and injection timing on the combustion and emission characteristics of a high-speed diesel engine. *Energy*. 2016, **107**, 572-579.

[2] PAYRI, R., VIERA, J.P., GOPALAKRISHNAN, V. et al. The effect of nozzle geometry over internal flow and spray formation for three different fuels. *Fuel*. 2016, **183**, 20-33

[3] YAO, C., GENG, P., YIN, Z. et al. Impacts of nozzle geometry on spray combustion of high pressure common rail injectors in a constant volume combustion chamber. *Fuel*. 2016, **179**, 235-245.

[4] PAYRI, R., VIERA, J.P., GOPALAKRISHNAN, V. et al. The effect of nozzle geometry over ignition delay and flame lift-off of reacting direct-injection sprays for three different fuels. *Fuel*. 2017, **199**, 76-90.

[5] NGUYEN, D., DUKE, D., KASTENGREN, A. et al. Spray flow structure from twin-hole diesel injector nozzles. *Experimental Thermal and Fluid Science*. 2017, **86**, 235-247.

[6] SALVADOR, F.J., LOPEZ, J.J., DE LA MORENA, J. et al. Experimental investigation of the effect of orifices inclination angle in multihole diesel injector nozzles. Part 1 – Hydraulic performance. *Fuel*. 2017, **213**, 207-214.

[7] TAGHAVIFAR, H., KHALILARYA, S., JAFARMADAR, S. et al. 3-D numerical consideration of nozzle structure on combustion and emission characteristics of DI diesel injector. *Applied Mathematical Modelling*. 2016, **40**(19-20), 8630-8646.

[8] LAHANE, S., SUBRAMANIAN, K.A. Impact of nozzle holes configuration on fuel spray, wall impingement and NO_x emission of a diesel engine for biodiesel–diesel blend (B20). *Applied Thermal Engineering*. 2014, **64**(1-2), 307-314.

[9] KOWALSKI, J. Wykorzystanie składu spalin w diagnostyce czterosuwowych silników okrętowych. Biblioteka Problemów Eksploatacji – Studia i Rozprawy. *Wydawnictwo Naukowe Instytutu Technologii Eksploatacji*, Radom 2015.

[10] SUH, H.K., LEE, C.S. A review on atomization and exhaust emissions of a biodiesel-fueled compression ignition engine. *Renewable and Sustainable Energy Reviews*. 2016, **58**, 1601-1620.

[11] KOWALSKI, J. An experimental study of emission and combustion characteristics of marine diesel engine with fuel pump malfunctions. *Applied Thermal Engineering*. 2014, **65**, 469-476.

[12] VAIRAMUTHU, G., SUNDARAPANDIAN, S., KAILASA-NATHAN, C. et al. Experimental investigation on the effects of cerium oxide nanoparticle on Calophyllumino-phyllum (Punnai) biodiesel blended with diesel fuel in DI diesel engine modified by nozzle geometry. *Journal of the Energy Institute*. 2016, **89**(4), 668-682.

Jerzy Kowalski, DSc. DEng. – Faculty of Ocean Engineering and Ship Technology at Gdansk University of Technology.

e-mail: *Jerzy.Kowalski@pg.edu.pl*

Article citation info:
CZERWINSKI, J. et al. Non-legislated emissions and PN of two passenger cars with gasoline-butanol blends. *Combustion Engines*. 2018, **172**(1), 64-72. DOI: 10.19206/CE-2018-108

Jan CZERWINSKI
Pierre COMTE
Danilo ENGELMANN
Peter BONSACK

CE-2018-108

Non-legislated emissions and PN of two passenger cars with gasoline-butanol blends

Increasing the sustainability of individual transportation and replacing a part of fossil energy in traffic by renewable energy carriers are worldwide important objectives. Bioalcohols are generally recognized as one of very useful alternatives. The global share of bioethanol used for transportation is continuously increasing. Butanol, a four-carbon alcohol, is considered in the last years as an interesting alternative fuel, both for diesel and for gasoline application. Its advantages for engine operation are: good miscibility with gasoline and diesel fuels, higher calorific value than ethanol, lower hygroscopicity, lower corrosivity and possibility of replacing aviation fuels.

In the present work, the emissions of two gasoline vehicles – with older and with newer technology – were investigated in dynamic-, stationary and cold start operation.

Key words: *alternative fuels, alcohols, nanoparticles, ammonia, cold start, emissions gasoline*

1. Introduction

1.1. Butanol and its effects on SI-engines

Butanol ($CH_3(CH_2)_3OH$) has a four-carbon structure and is a higherchain alcohol than Ethanol, as the carbon atoms can either form a straight chain (n-butanol) or a branched structure (iso-butanol), thus resulting in different properties. Consequently, it exists as different isomers depending on the location of the hydroxyl group (-OH) and carbon chain structure, with butanol production from biomass tending to yield mainly straight chain molecules. 1-butanol, better known as *n*-butanol (normal butanol), has a straight-chain structure with the hydroxyl group (-OH) at the terminal carbon.

N-butanol is of particular interest as a renewable biofuel as it is less hydrophilic, and possesses higher energy content, higher cetane number, higher viscosity, lower vapour pressure, higher flash point and higher miscibility than ethanol, making it more preferable than Ethanol for blending with diesel fuel. It is also easily miscible with gasoline and it has no corrosive, or destructing activity on plastics, or metals, like ethanol or methanol.

Several research works were performed with different butanol blends BuXX [1–9]. Generally, there are advantages of higher heat value (than ethanol). The oxygen content of butanol has similar ad-vantages, like with other alcohols: tendency of less CO & HC, but possibility of increasing NO_x (depending on engine parameters setting).

The good miscibility, lower hygroscopicity and lower corrosivity make butanol interesting alternative.

The trend of downsizing the SI-engines in the last years implies much higher specific torques and with it an aptitude of knocking and mega-knocking at high- and full load. The alcohols have a higher octane numbers (RON), are more resistant to knocking and are a welcomed solution for this new technology of engines [1].

A basic research of butanol blends Bu20 & Bu100 was performed on mono-cylinder engines with optical access to the combustion chamber [2, 3]. One of the engines was with GDI configuration. It was demonstrated, that the alcohol blend improved the internal mixture preparation and reduced the carbonaceous compounds formation and soot.

Concerning the characteristics of combustion Bu100 was similar to gasoline. This research considered only little number of constant operating points.

Using *n*-butanol in an optical port fuel injection (PFI) SI engine slightly higher combustion rates and lower formation of particulates was found compared to gasoline [4, 5]. Similarly [6] reported that the duration of the early combustion stage and length of combustion in an SI engine were, compared to gasoline, shortened with increased n-butanol share, and slightly lower variability of indicated mean pressure (IMEP) was observed when running on neat n-butanol. Shorter early combustion stage, faster combustion and better combustion stability were also observed by other researchers [7, 8].

The alcohol blend fuels E85 & Bu85 were tested on a vehicle with TWC in road application and with on-board measuring system for exhaust emissions [9]. It was stated for butanol, that it has no significant influence on CO & HC, but it increases strongly NO_x. Nevertheless, this is due to the limits of lambda regulation and as effect of it to the production of too many lean lambda excursions during the transients.

The warm operation with Bu85 was with no problems, the cold startability and emissions were not investigated.

1.2. Non-legislated emissions of gasoline cars

The most important non-legislated emission components in present discussions are: the nanoparticles (NP), ammonia (NH_3), nitrous oxide (N_2O), formaldehyde (HCHO) and acetaldehyde (MeCHO).

The nanoparticles (NP) became an important research topic, since the first introduction of legal nanoparticle counts limits (Euro 5b) for DI SI passenger cars in EU beginning of 2013. In this situation, the NP and especially the metal oxides emissions from additive packages of lube oils and fuels, be-come an important topic for all kinds of engines. Lube oil contributes to the NP-emission especially at cold start [10–12]. These new aspects have to be investigated with Ethanol blend fuels Exx.

Further gaseous substances, which may be present under certain conditions in very low concentrations in the exhaust gases are considered to be potential candidates for future legal limitation. These non-legislated emission components are: ammonia (NH_3), nitrogen dioxide (NO_2), nitrous oxide (N_2O), formaldehyde (HCHO) and acetaldehyde (MeCHO) – all of them quite easy to be measured and indicated with FTIR.

Production of ammonia (NH_3) in the exhaust of gasoline cars with TWC was demonstrated in [13] and [14] – this especially at transient operation with rich excursions of lambda. The other components were little investigated in connection with E85-operation. From the research of the authors can be stated, that with a correctly working TWC (at warm operation) there are usually no measurable concentrations of NO_2 and N_2O and the HCHO – values show a noise below 1 ppm [15]. The components HCHO and MeCHO are supposed to produce a peak at cold start, but are little investigated and presented in the literature.

The presented tests were performed in the IC-Engines Laboratory of the University of Applied Sciences, Biel, CH within the framework of project GasBut (gasoline + butanol).

This research was conducted on two cars: an older one, with MPI & $\lambda = 1$ concept and a newer one (Euro 5), with GDI, $\lambda = 1$ concept and flex fuel aptitude.

The test vehicles were driven at WLTC cold & warm, as well as at a steady state cycle (SSC). The measurements of legislated and non-legislated emissions (NP & FTIR) were attached.

Special attempts of cold starts were conducted and compared with the equivalent results with Bu0 & Exx. The tests were performed with Bu0, B15 and Bu30.

This research enabled a complete insight in the non-legislated emissions at cold start and in repetitive transient operation with quite different state of the gasoline cars.

2. Test vehicles, fuels and lubricants

The tests on gasoline vehicles were performed: with a Renault 18 Break (SI, MPI, TWC), which represents an older technology in this project and with a flex fuel vehicle (FFV) Volvo V60 (GDI, Euro 5), which represents a newer technology. These vehicles were operated with gasoline, in original condition (TWC) and with two butanol blend fuels Bu15 and Bu30. The vehicles are presented in Fig. 1 and Tab. 1.

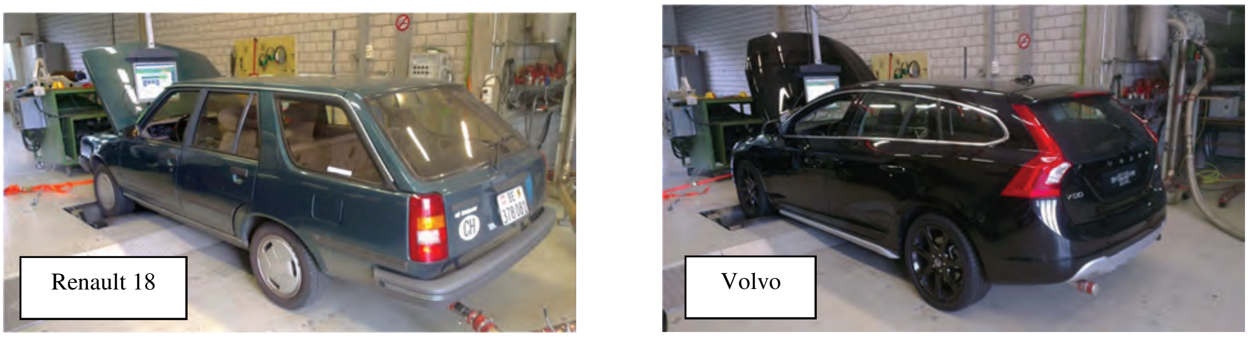

Fig. 1. Gasoline vehicles for research of emissions

Table 1. Data of tested vehicles

Vehicle	Renault 18 Break	Volvo V60 T4F
Engine code	J7T-718	B4164T2
Number and arrangement of cylinders	4 / in line	4 / in line
Displacement cm3	2164	1596
Power kW	74 @ 5000 rpm	132 @ 5700 rpm
Torque Nm	162 @ 2000 rpm	240 @ 1600 rpm
Injection type	MPI	DI
Curb weight kg	1110	1554
Gross vehicle weight kg	1585	2110
Drive wheel	Front-wheel drive	Front-wheel drive
Gearbox	m5	a6
First registration	01.04.1985	27.01.2012
Exhaust	EURO 0	EURO 5a
VIN	VF1135B00F0000505	YV1FW075BC1043598
Vehicle	Renault 18 Break	Volvo V60

Table 2. Fuel properties of the test fuels

Specification		**RON 95**	**n-butanol**
Other name		Gasoline, Bu0	1-butanol
Formula		-	$C_4H_{10}O$
Density	$[kg/dm^3]$	0.737	0.810
Stoichiometric AF-ratio	[kg air]	14.70	11.10
Lower heating value	[MJ/kg]	42.7	33.0
O_2 fraction	$[\%_m]$	1.70	21.62
Boiling range	[°C]	38-175	115-119
Blending RON		95	99
Blending MON		87	84
Self-ignition temperature	[°C]	300	343
Flash point	[°C]	<-40	34
Viscosity @ 40°C	[mPa*s]	0.83	2.9
		Bu15	**Bu30**
Density	$[kg/dm^3]$	0.748	0.759
Stoichiometric AF-ratio	[kg air]	14.12	13.55
Lower heating value	[MJ/kg]	41.1	39.6
O_2 fraction	$[\%_m]$	3.50	8.08

2.1. Fuels

The gasoline used was from the Swiss market, RON 95, according to SN EN228; n-butanol was purchased from Thommen-Furler AG. As blend fuels were used: Bu15 and Bu30 (15% vol. and 30% vol. butanol).

Table 2 presents the most important data of the fuels (according to the literature sources). It can be remarked that with increasing share of butanol the oxygen content of blend fuel increases and the heat value and stoichiometric air requirement decrease.

2.2. Lubricants

In the present tests the lube oil was not changed and analyzed – the same oil was used for all tests.

3. Test methods and instrumentation

3.1. Chassis dynamometer and standard test equipment

- roller dynamometer: Schenk 500 GS 60
- driver conductor system: Tornado, version 3.3.
- CVS dilution system: Horiba CVS-9500T with Roots blower
- air conditioning in the hall automatic (intake- and dilution air)

The driving resistances of the test bench were set according to the legal prescription.

3.2. Test equipment for regulated exhaust gas emissions

This equipment fulfils the requirements of the Swiss and European exhaust gas legislation.

- gaseous components:
  exhaust gas measuring system Horiba MEXA-9400H
  CO, CO_2 – infrared analysers (IR), HCIR, HCFID, NO/NO_X, CLA

The dilution ratio DF in the CVS-dilution tunnel is variable and can be controlled by means of the CO_2-analysis.

3.3. FTIR

FTIR (Fourier Transform Infrared) Spectrometer (AVL Sesam) offers the possibility of simultaneous, time-resolved measurement of approx. 30 emission components – among others: NO, NO_2, NO_x, NH_3, N_2O, HCN, HNCO, HCHO and MeCHO.

3.4. Nanoparticle analysis

The measurements of NP size distributions were conducted with different SMPS-systems, which enabled different ranges of size analysis:

SMPS: DMA TSI 3081 and CPC TSI 3772 (9.8–429 nm)
nSMPS: nDMA TSI 3085 and CPC TSI 3025 (3–64 nm).

For the dilution and sample preparation an ASET system from Matter Aerosol was used, Fig. 2 (ASET – aerosol sampling and evaporation tube). This system contains:

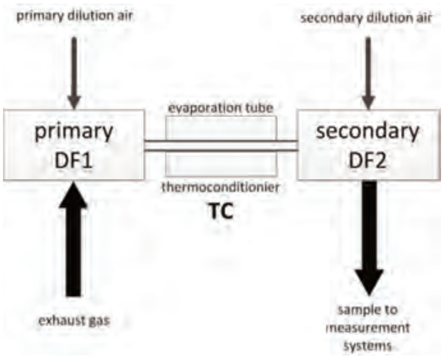

Fig. 2. Set-up of dilution stages and sample preparation for nanoparticle measurements

- Primary dilution air – MD19 tunable minidiluter (Matter Eng. MD19-2E)
- Secondary dilution air – dilution of the primary diluted and thermally conditioned measuring gas on the outlet of evaporative tube.
- Thermoconditioner (TC) – sample heating at 300°C.

The measuring set-up on chassis dynamometer and the sampling positions for particle analytics are represented in Fig. 3.

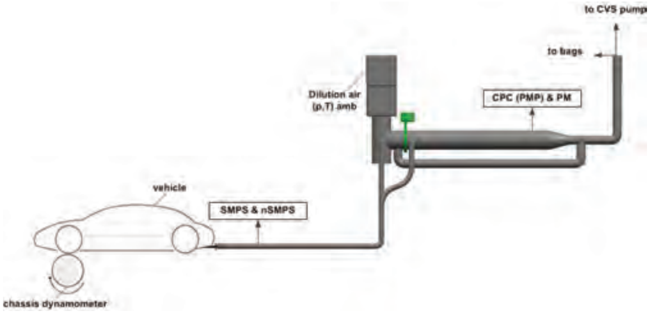

Fig. 3. Sampling of exhaust gas for analysis of particles

4. Test procedures on chassis dynamometer

The vehicles were tested on a chassis dynamometer in the dynamic driving cycles WLTC and at constant speeds in the steady state cycle SSC. SSC consists of 20 min steps at constant vehicle speeds 95, 45 km/h and idling, which are driven from the highest to the lowest speed. These vehicle speeds respond to the average speeds in parts of the WLTC. The test sequences with all fuels were identical: WLTC with cold start (20–25°C), 10 min idling for bag evaluation, acceleration to 95 km/h and continuation of the SSC.

In terms of the driving cycles an approach to find a homogenized world-wide driving cycle was finished with the development of the homogenized WLTP world-wide light duty test procedure. The WLTC (world-wide light duty test cycle) represents typical driving conditions around the world and is developed based on combination of collected in-use data and suitable weighting factors. This cycle has been used also in this study, Fig. 4. It represents different driving situation, like city, over-land and speed-way.

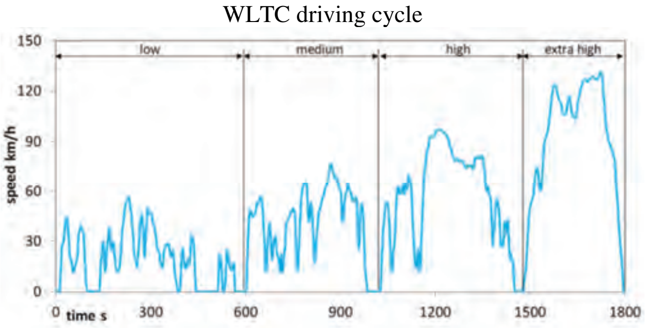

Fig. 4. WLTC driving cycle

5. Results

5.1. Comparison of emissions of vehicles with older and with newer technology

Regarding the comparison of emissions time-plots in WLTC (not represented here), it can be generally remarked for all three fuels (Bu0, Bu15 and Bu30):

- with the older vehicle (R18) there are considerably higher emissions of CO and HC at cold start and there are higher and more frequent peaks of all components (CO, HC and NO_x) during the driving cycle,
- all non-legislated emissions: NH_3, HCHO, MeCHO and N_2O are for R18 significantly higher.

Considering the integral average emissions in WLTC (whole cycle), Figs 5 and 6, these statements can be confirmed:

- higher CO- and HC-values with R18,
- with Bu15 CO is reduced more for V60, than for R18,
- with Bu30 CO for V60 stays at the level of Bu15, while for R18 it increased again to the original level of Bu0,
- HC for both vehicles is unchanged, or slightly reduced with Bu15, but it generally increases with Bu30,
- NO_x is strongly increased by both BuXX fuels for the older vehicle (R18) and it is reduced for the newer vehicle (V60) – this is a sensitive indication of better functioning of the Lambda regulation of V60, with less "lean-excursions",
- the nanoparticle emission of V60 is significantly reduced with both BuXX-fuels; the PN emission of R18 is not influenced by the fuel,
- all non-legislated emissions: NH_3, HCHO, MeCHO and N_2O are for R18 significantly higher,
- there is a tendency of increasing HCHO and MeCHO with increasing BuXX for both vehicles,
- with increasing BuXX there is an increase of NH_3 for V60 and approximately no influence for R18.

One example of time-plots of non-legislated gaseous components, with both vehicles and with gasoline (Bu0), is given in Fig. 7. It clearly demonstrates the advantages of the newer car (V60).

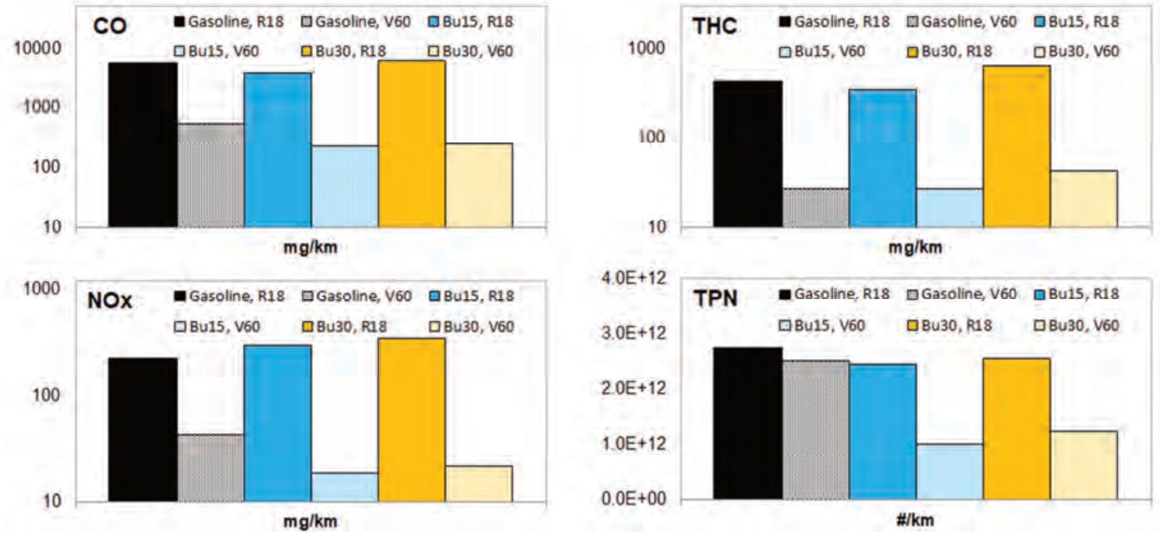

Fig. 5. Comparisons of emissions R18 vs V60 in WLTC cold with Bu0, Bu15 & Bu30

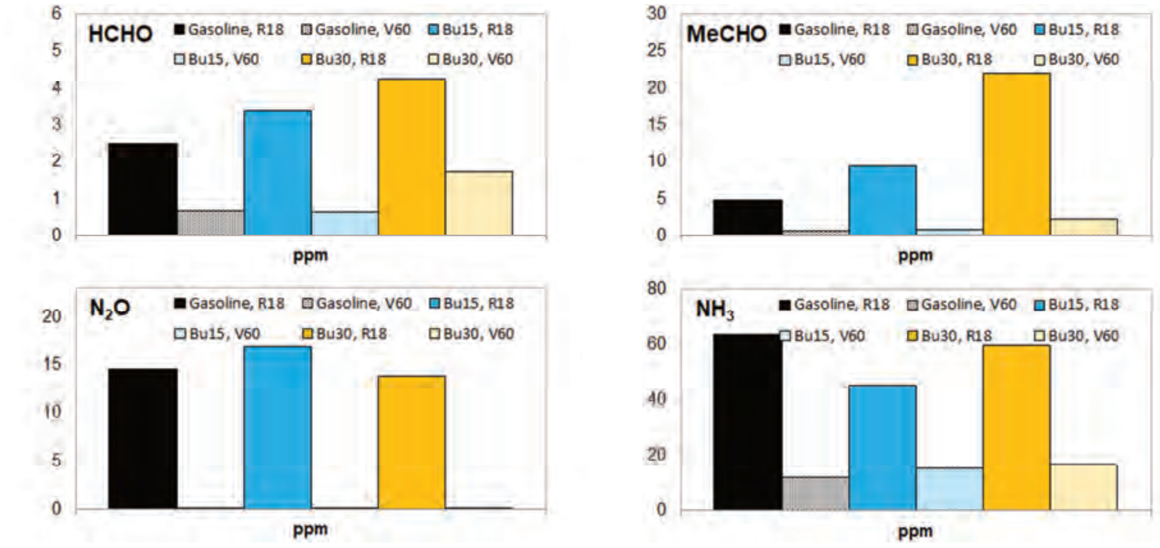

Fig. 6. Comparisons of non-legislated emissions in WLTC cold

Fig. 8 illustrates the relationships of emissions at 95 km/h (in the 1st step of SSC).

A look on the average emission values in SSC allows the general statements:

- in most cases there are higher CO-and HC-values for R18,
- with increasing Bu-content at 95 km/h there is a strong increase of NO_x for R18 and no influence on NO_x for V60,
- the nanoparticle emission of V60 is significantly reduced with both BuXX-fuels; the PN emission of R18 is not influenced by the fuel,
- in most cases the higher values of NH_3, N_2O and MeCHO are confirmed for R18.

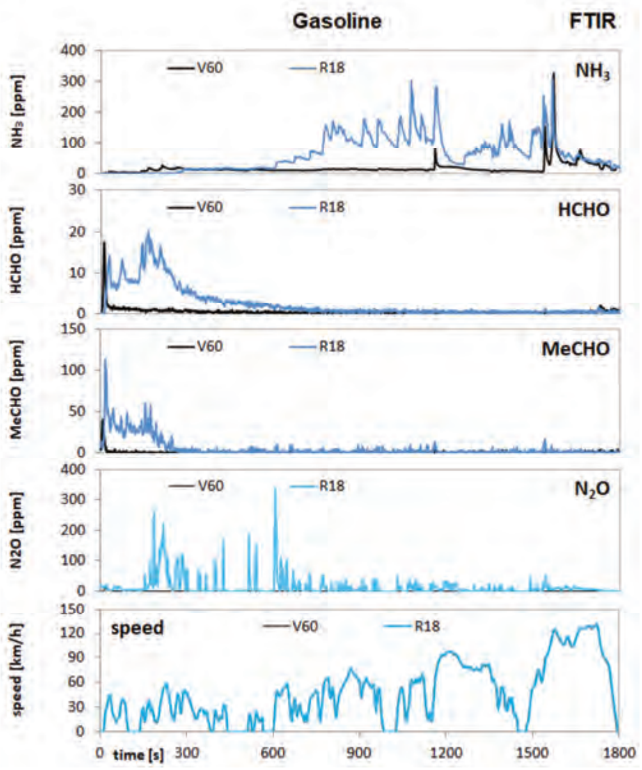

Fig. 7. Comparison of NH3-, HCHO-, MeCHO and N2O-emissions of two vehicles during the driving cycle WLTC cold

In the first step (95 km/h) Volvo (V60) has with gasoline higher nanoparticle emissions (CPC), than Renault (R18). With Bu15 and Bu30 this is no more the case, since the NP are for V60 considerable reduced with BuXX.

After switching the operation to idling there is for R18 an increase of NP (CPC), because there are the highest PN-emissions at idling for this vehicle. These NP consist in a large portion of unburned lube oil and it is not surprising that their number increases gradually with the cooling down the exhaust system and the catalyst (not represented here).

The highest NP-emissions at idling of R18, as well as their appearance mainly in the nuclei mode are documented in Fig. 9. The nanoSMPS offers at certain operating points, especially at 45 km/h, valuable supplementary information.

5.2. Non-legislated emissions of both vehicles

Figures 10 & 11 represent for both cars some non-legislated components in the first part of the cycle with cold start and warm-up. The sequence of increased emission peaks with higher Bu-content is clearly repetitive. There are considerable peak values with Bu30. For R18: HCHO up to 30 ppm and MeCHO up to 950 ppm and for V60: HCHO up to 60 ppm and MeCHO up to 220 ppm. N_2O emission peaks depend only few from the fuel variant. NH_3-values are generally low after the cold start and they become higher in the hot last part of the cycle.

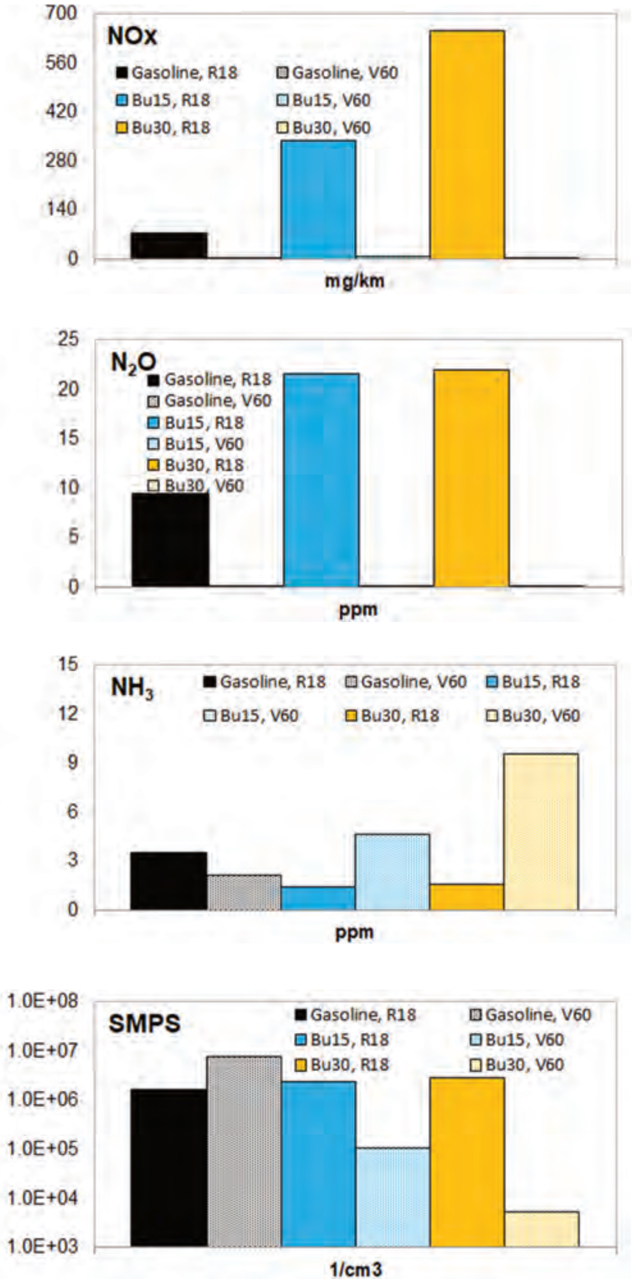

Fig. 8. Comparison of exhaust emissions of two vehicles at 95 km/h with different fuels

Figures 12 & 13 offer a consideration of SMPS particle size distributions for both vehicles, with three fuels and in all steps of the SSC.

For R18, the particle size distributions with SMPS (and with nSMPS) show principally higher PN-values with higher butanol content. At 45 km/h there is a major part of nanoparticles in the smallest sizes, below the measuring range of SMPS. The highest PN-concentration are reached at idling. This vehicle is known to produce excessive NP-emissions in nuclei mode, which originate from the higher lube oil consumption.

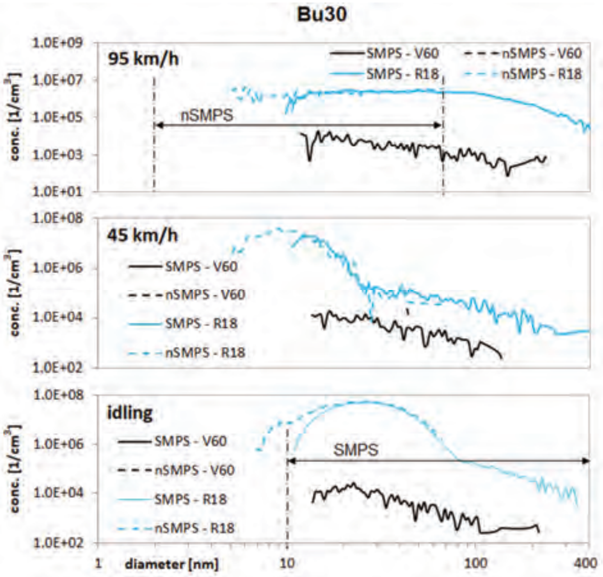

Fig. 9. Particle Size Distribution (PSD) during the SSC cycle. Comparison SMPS – nSMPS of two vehicles

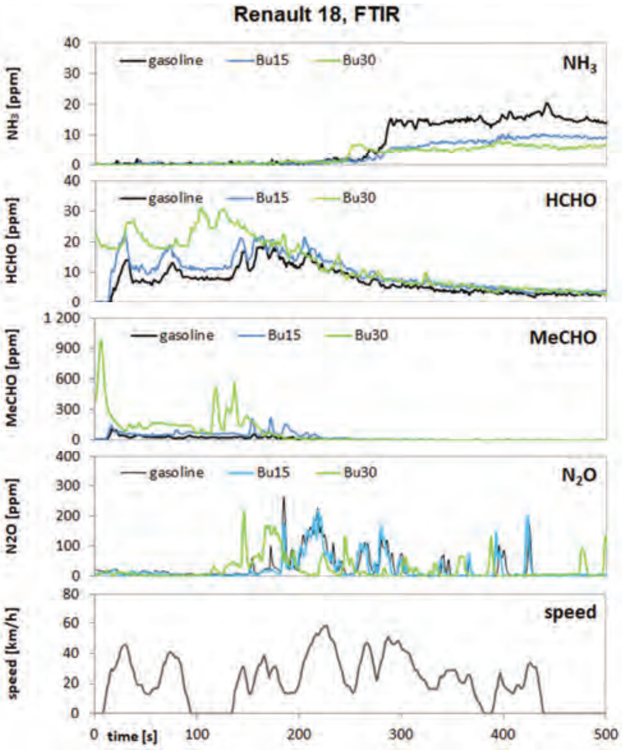

Fig. 10. Comparison of NH_3-, HCHO-, MeCHO- & N_2O-emissions in the first part of WLTC cold with different fuels

For V60, there is an inverse influence of Bu-blends: there is a clear lowering of particle number (PN) with increasing BuXX. At idling, generally the lowest PN counts concentrations are resulting.

From the comparisons in this section, it can be concluded that the different engines' ages and technology (different mixtures' preparations MPI/DI, combustion, lube oil consumption and exhaust aftertreatment) have a significant impact on the emissions and especially on the emissions at cold start.

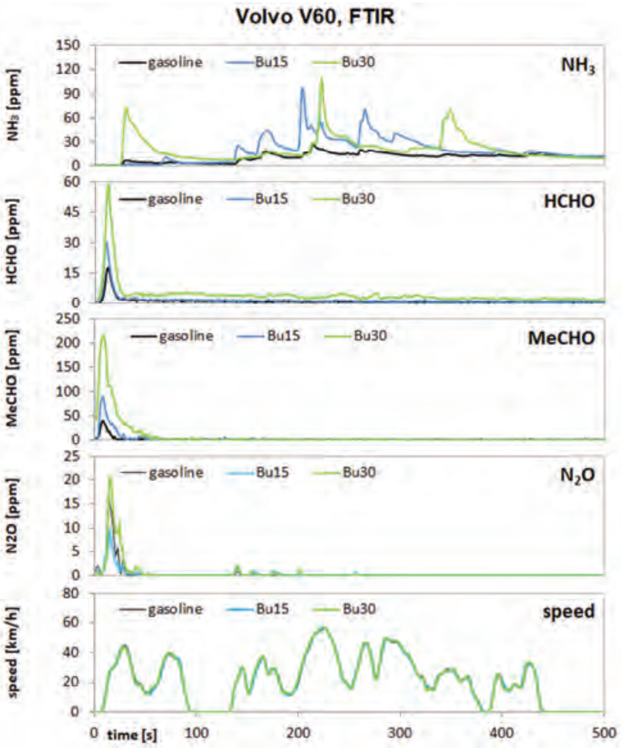

Fig. 11. Comparison of NH_3-, HCHO-, MeCHO- & N_2O-emissions in the first part of WLTC cold with different fuels

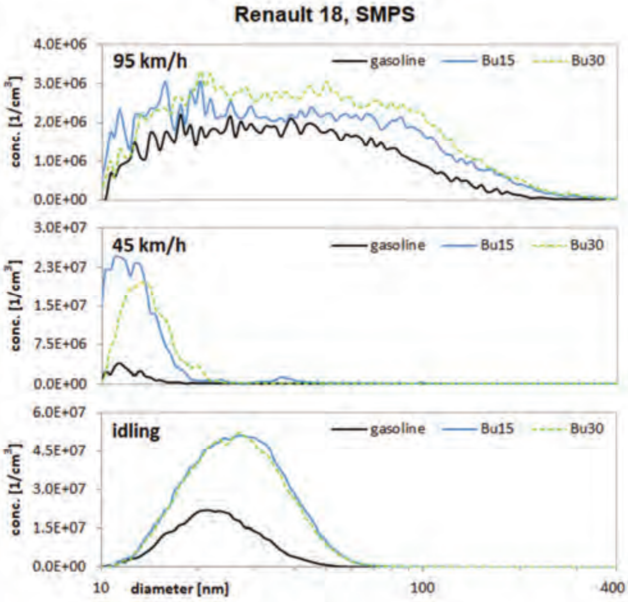

Fig. 12. Comparison of the Particle Size Distribution (PSD) during the driving cycle SSC with different fuels

5.3. Cold start

Repetitive cold start tests were performed with Volvo V60 and with Bu0/Bu15/Bu30. For cold starts (CS), two ranges of start temperature were considered: summer cold start (20 to 25°C, conditioning in the test hall), or mild winter cold start (–2 to 4°C, conditioning outside in the cold weather period). For simplification of titles and descriptions these temperature ranges will be designed, as 20°C and 0°C.

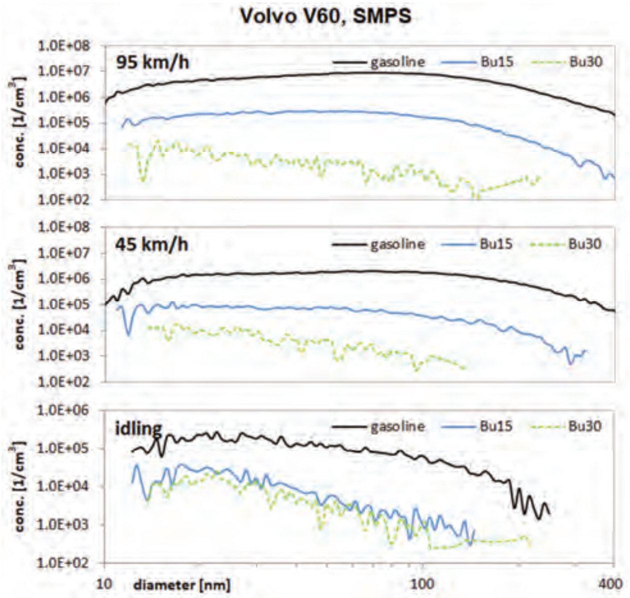

Fig. 13. Comparison of the Particle Size Distribution (PSD) during the driving cycle SSC with different fuels

In the preliminary tests with gasoline two variants of cold start were investigated:

a. cold start at idling (without chassis dynamometer),
b. cold start with acceleration to 20 km/h and v= const = 20 km on the chassis dynamometer, the braking resistances were set according to legal prescriptions and they responded to the horizontal road.

It was stated after this test period, that the CS on chassis dynamometer (with 20 km/h) does not bring any further information potentials and further research was generally limited to the CS at idling. Vehicle, which was conditioned outside for the mild winter CS was pushed in the test hall, attached to the measuring systems, started and operated in the conditions of the hall (intake air 20–25°C). After the test, the vehicle was conditioned by driving a NEDC on the chassis dynamometer.

Fig. 14 shows some non-legislated gaseous components, comparing Bu0/Bu15/Bu30 in two temperature domains of the CS: 0°C and 20°C. With higher Bu-content the peaks of formaldehyde HCHO and of acetaldehyde MeCHO increase. Starting with a lower temperature, these peak-values are higher and can attain for MeCHO 250 ppm. The ammonia NH_3 concentrations are at cold start (CS) near to zero and they increase slightly after engine warms up. Nevertheless, there is for NH_3 no correlation with fuel quality.

Fig. 15 compares the nanoparticle emissions with the fuels Bu0/Bu15/Bu30 at CS in both temperature ranges 0°C & 20°C. CPC (condensation particle counter) measures the particle numbers of all particle sizes according to the PMP-guidelines. SMPS (scanning mobility particle sizer) measures the particle numbers in function of their size.

The SMPS-particle size distributions were taken in the successive parts of the warm-up period: (1) 0–120 s; (2) 120–300 s and (3) 300–600 s.

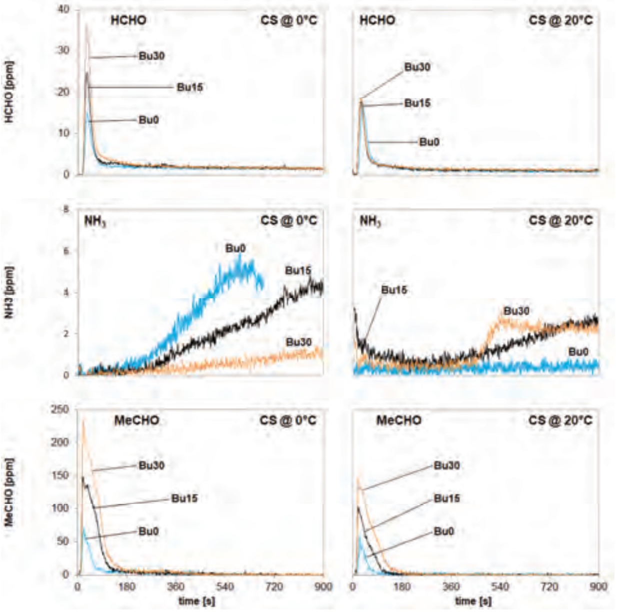

Fig. 14. Comparison of the non-legislated gaseous emissions during cold start at idling with different fuels, measured with FTIR at tailpipe

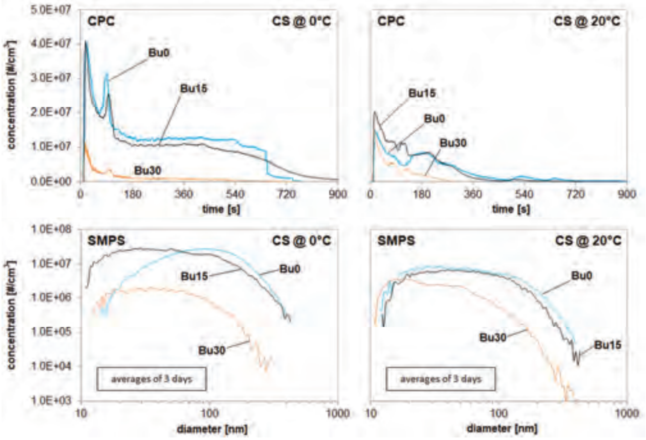

Fig. 15. Comparison of the particles counts during cold start at idling with different fuels, measured with both systems at tailpipe

The successive SMPS-scans of each CS-attempt (not represented here) showed clearly the lowest PC-level of the latest sample. The 1st sample was well repeatable and the PSD's in Fig. 4 are averages from three cold starts of the 1st scan (in the period 0–120 s).

The CPC-signals at 0°C have a second peak after approximately 2 min. This is visible particularly with gasoline (E0). This peak is a repeatable event, it can also be found in other emission courses (like N_2O) and it is attributed to the changes introduced by the engine ECU in function of temperature, like possibly catalyst heating, switching of internal EGR by vario cams, or heat management.

The most important information of Fig. 15 is that Bu15 emits similar level of particle counts concentration, like Bu0, while B30 reduces clearly the PN emissions. Bu15 has similar oxygen content like E10. Nevertheless, it was found that Bu15 produces significantly higher peaks of MeCHO and HCHO at cold start than E10 [3].

6. Conclusions

The elaborated results allow following observations for R18:

- At cold start and warm-up all three investigated fuels produce increased CO-, HC- and NP-values in similar way.
- The emissions of HCHO and MeCHO at cold start increase in the sequence of increasing butanol content.
- In the "high" and "extra high" parts of WLTC there are the highest NH_3 peaks, which coincide with the strongest acceleration events in the cycle.
- Regarding the average emission values in WLTC cold: with increasing butanol content (BuXX) there is a clear tendency of increasing the emissions of: NO_x, HCHO, MeCHO and ETOH. The average emissions of N_2O and NH_3 are independent on the BuXX.
- At steady state operation (in SSC) with increasing butanol content there are:
  - higher NO_x-values at the highest speed (95 km/h),
  - higher PN-values at all operating conditions.
- With higher butanol content, the lambda regulation of this vehicle has difficulty to compensate the higher oxygen content of the fuel. As a result, there is a leaner operation and lower NO_x-conversion in the TWC.
- Higher butanol content interferes more with the lube oil and tendentiously increases the nanoparticles counts.
- Higher butanol content also creates favourable conditions to produce more formaldehyde (HCHO) and acetaldehyde (MeCHO) at cold start.

With B30 the excessive leaning was remarkable as a less powerful load responses and worse driveability. B30 is regarded as a maximum of butanol content to be recommended for this vehicle.

For Volvo V60 and for transient operation in WLTC can be remarked:

- With increasing portion of butanol in fuel (BuXX) there are increasing peak values of HC, HCHO, MeCHO, ETOH and N_2O at cold start.
- During and after the acceleration events in the highest part of the cycle there are emission peaks of some components, but they cannot be attributed to a specific bu-content (BuXX).
- The comparison of average emission values in WLTC, confirms the lower CO- and lower PN-values with BuXX, while it is difficult to notice the difference between Bu15 and Bu30.
- The average of FTIR-values confirms the higher values of: HCHO, MeCHO and NH_3 with BuXX.
- There is a clear lowering of particle number (PN) with increasing BuXX.

Comparison R18-V60 in WLTC

- Higher CO- and HC-values with R18 and no clear influence of fuel on these emissions.
- HC for both vehicles is unchanged, or slightly reduced with Bu15, but it generally increases with Bu30.
- NO_x is strongly increased by both BuXX fuels for the older vehicle (R18) and it is reduced for the newer vehicle (V60) – this is a sensitive indication of better functioning of the lambda regulation of V60, with less "lean-excursions".
- The nanoparticle emission of V60 is significantly reduced with both BuXX-fuels; the PN emission of R18 is not influenced by the fuel.
- All non-legislated emissions: NH_3, HCHO, MeCHO and N_2O are for R18 significantly higher.
- There is a tendency of increasing HCHO and MeCHO with increasing BuXX for both vehicles.
- With increasing BuXX there is an increase of NH_3 for V60 and approximately no influence for R18.

For cold start tests with Volvo V60 can be concluded:

- With increasing butanol content (Bu0/Bu15/Bu30) the emissions at cold start are influenced in following way:
  - Higher peaks of acetaldehyde (MeCHO) at start,
  - Higher peaks of formaldehyde (HCHO) at start,
  - The nanoparticles with Bu15 have similar level as with Bu0 (both CPC and SMPS), with Bu30 they are approximately 1 order of magnitude lower.
- The higher temperature of the cold start generally lowers the emission peaks.

It is important to mention that the original plans of this project part were to test the cold start with Bu85. This was also tried in both temperature domains (0°C & 20°C) but without success. The start and the operation were not possible with this FFV. Butanol has a higher boiling point, than ethanol and therefore the quality of mixture preparation (part of evaporated fuel) with butanol is worse. The investigated vehicle (FFV) is developed for ethanol and cannot work adequately with higher butanol contents.

Acknowledgements

The authors want to express their gratitude to the institutions, which financially supported these research activities: Swiss Federal Office of Energy (BfE), Swiss Federal Office of Environment (BAFU) and Swiss Oil Association (EV).

Nomenclature

AFHB	Abgasprüfstelle FH Biel, CH
ASET	Aerosol Sampling and Evaporation Tube
ASTRA	Amt für Strassen (CH)
BAFU	Bundesamt für Umwelt, (Swiss EPA)
BfE	Bundesamt für Energie
Bu	butanol
BuXX	butanol content XX
CLA	chemiluminescent analyzer
CLD	chemiluminescent detector
CO	carbon monoxide
CO_2	carbon dioxide
CPC	condensation particle counter
CS	cold start
CVS	constant volume sampling
DF	dilution factor
DI	direct injection
DMA	differential mobility analyzer
ECU	electronic control unit

EV	Erdölvereinigung
FFV	flex fuel vehicle
FID	flame ionisation detector
FTIR	Fourier Transform Infrared analyzer
GasBut	gasoline buthanol project
HC	unburned hydrocarbons
HCHO	formaldehyde
HCN	hydrogen cyanide
HNCO	isocyanic acid
MD	minidiluter
MeCHO	acetaldehyde
NEDC	New European Driving Cycle (ECE + EUDC)
NH_3	ammonia
NO	nitrogen monoxide
NO_2	nitrogen dioxide
N_2O	nitrous oxide
N_2	nitrogene
NO_x	nitric oxides
NP	nanoparticles < 999 nm
PC	particle counts (integrated)
PN	particle numbers
PSD	particle size distribution
R18	Renault 18
SMPS	scanning mobility particle sizer
TC	thermoconditioner
TWC	three way catalyst
V60	Volvo V60
WLTC	worldwide harmonized light duty test cycle
WLTP	worldwide harmonized light duty test procedure
3WC	three way catalyst

Bibliography

[1] BRASSAT, A., THEWES, M., MÜTHER, M. et al. Massgeschneiderte Kraftstoffe aus Biomasse für Ottomotoren. *MTZ.* 2011, **12**, 988.

[2] MARCHITTO, L., MAZZEI, A., MEROLA, S.S. et al. Optical investigations of combustion process in SI and CI engines fuelled with butanol blends. *TAE Technische Akademie Esslingen, 9th International Colloquium "Fuels"*, Jan. 15-17, 2013.

[3] IRIMESCU, A., TORNATORE, C., MEROLA, S.S. et al. Integrated diagnostics for combustion investigation in a DISI engine fueled with butanol and gasoline at different load settings. *TAE Technische Akademie Esslingen, 10th International Colloquium „Fuels", Stuttgart/Ostfildern*, January 2015, p. 117.

[4] TORNATORE, C., MARCHITTO, L., VALENTINO, G. et al. Optical diagnostics of the combustion process in a PFI SI boosted engine fueled with butanol-gasoline blend. *Energy.* 2012, **45**(1), 277-287, doi: 10.1016/j.energy.2012.03.006.

[5] MEROLA, S., TORNATORE, C., MARCHITTO, L. et al. Experimental investigations of butanol-gasoline blends effects on the combustion process in a SI engine. *International Journal of Energy and Environmental Engineering*, 2012, doi: 10.1186/2251-6832-3-6.

[6] SZWAJA, S., NABER, J.D. Combustion of n-butanol in a spark-ignition IC engine. *Fuel.* 2010, **89**(7), 1573-1582, doi:10.1016/j.fuel.2009.08.043.

[7] GU, X., HUANG, Z., CAI, J. et al. Emission characteristics of a spark-ignition engine fuelled with gasoline-n-butanol blends in combination with EGR. *Fuel.* 2012, **93**, 611-617, doi:10.1016/j.fuel.2011.11.040.

[8] DERNOTTE, J., MOUNAIM-ROUSSELLE, C., HALTER, F. et al. Evaluation of butanol-gasoline blends in a port fuel-injection, spark-ignition engine. *Oil Gas Sci Technol – Rev IFP,* 2010, **65**, 45-51, doi: 10.2516/ogst/2009034.

[9] VOJTISEK-LOM, M., PECHOUT, M., MAZAC, M. Real-world on-road exhaust emissions from an ordinary gasoline car operated on E85 and on butanol-gasoline blend. *SAE Technical Paper* 2013-24-0102.

[10] CHAN, T.W., MELOCHE, E., KUBSH, J. et al. Impact of ambient temperature on gaseous and particle emissions from a direct injection gasoline vehicle and its implications on particle filtration. *SAE Technical Paper* 2013-01-0527.

[11] SONNTAG, D.B., BAILEY, C.R., FULPER, C.R. et al. Contribution of lubricating oil to particulate matter emissions from light-duty gasoline vehicles in Kansas City. *Environment Science & Technology*, 27. Febr. 2012.

[12] PORTER, S. Particle number emissions of gasoline hybrid electric vehicle. *MTZ.* 2012, **4**.

[13] HEEB, N., FORSS, A-M., BRÜHLMANN, S. et al. Three-way catalyst-induced formation of ammonia – velocity- and acceleration-dependent emission factors. *Atmospheric Environment.* 2006, **40**, 5986-5997.

[14] HEEB, N., SAXER, C., FORSS, A.-M. et al. Trends of NO-, NO_2-, and NH_3-emissions from gasoline-fueled Euro-3- to Euro-4-passenger cars. *Atmospheric Environment.* 2008, **42**, 2543-2554.

[15] CZERWINSKI, J., COMTE, P., STEPIEN, Z. et al. Effects of ethanol blend fuels E10 & E85 on the non-legislated emissions of a flex fuel passenger car. *SAE Technical Paper* 2016-01-0977.

Jan Czerwinski, Prof. DEng. – Professor in the University of Applied Sciences, Biel-Bienne, Switzerland.

e-mail: *Jan.Czerwinski@bfh.ch*

Pierre Comte, Dipl.-HTL-Ing. – University of Applied Sciences, Biel-Bienne, Switzerland.

e-mail: *Pierre.Comte@bfh.ch*

Danilo Engelmann, DEng. – Professor in the University of Applied Sciences, Biel-Bienne, Switzerland.

e-mail: *Danilo.Engelmann@bfh.ch*

Peter Bonsack, MSc. ME – Federal Office for the Environment FOEN, Bern, Switzerland.

e-mail: *Peter.Bonsack@bafu.admin.ch*

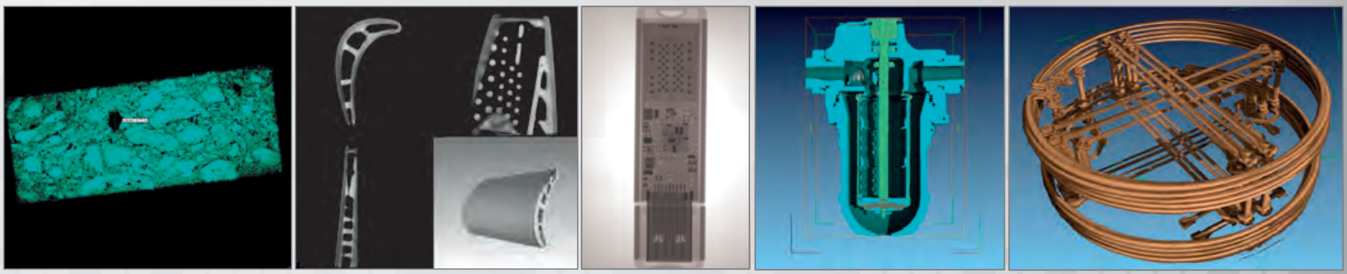


phoenix v|tome|x m

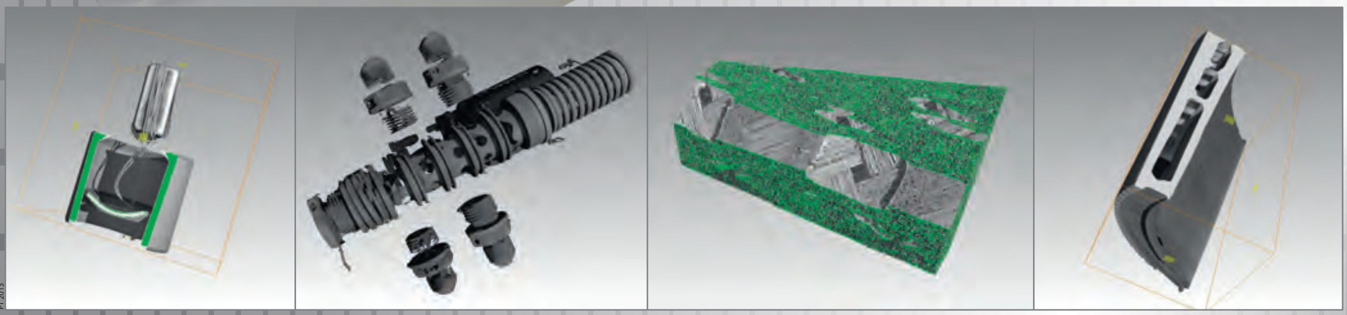

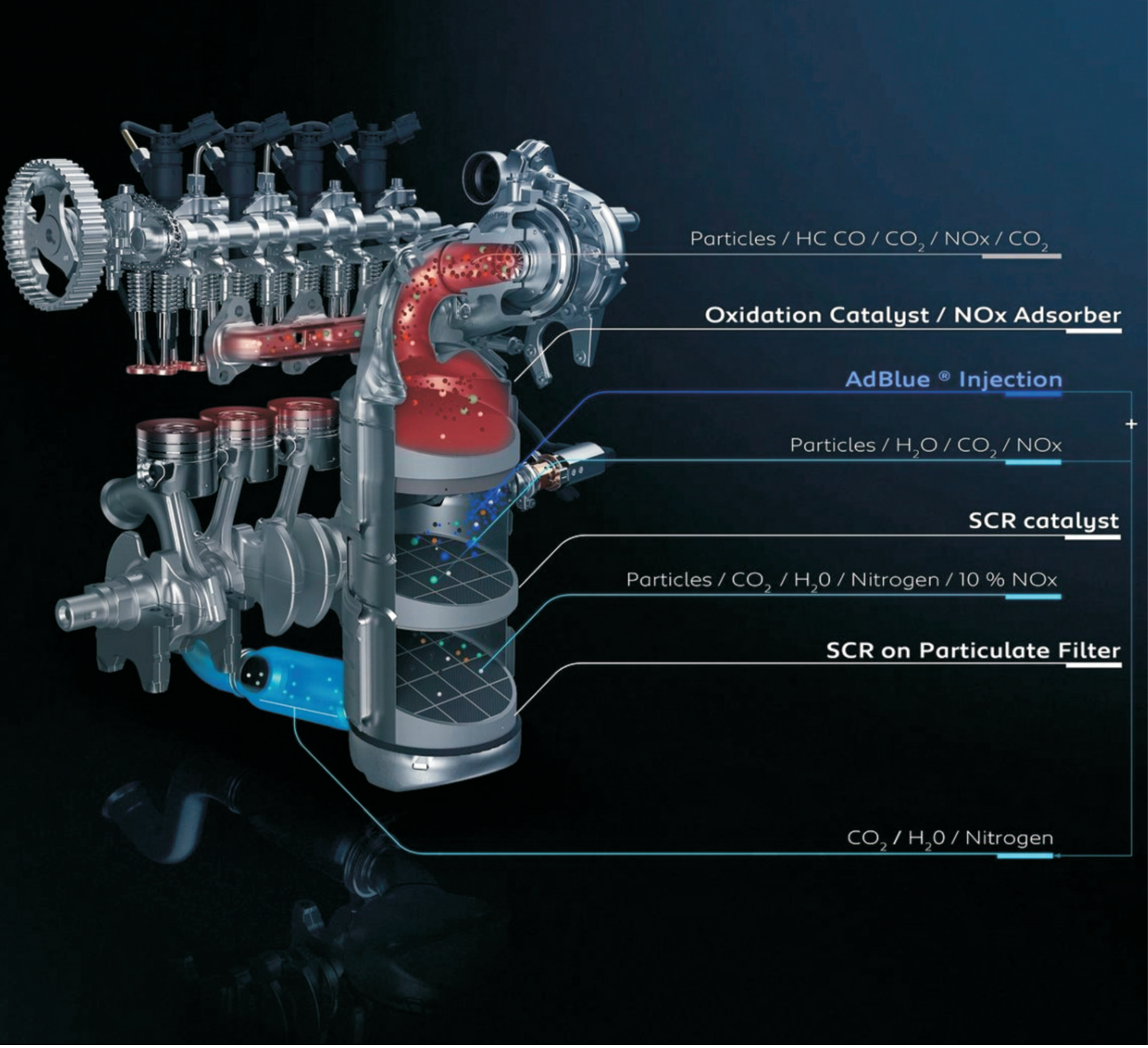

Publisher:

Polish Scientific Society of Combustion Engines

Combustion Engines

Polskie Towarzystwo Naukowe Silników Spalinowych

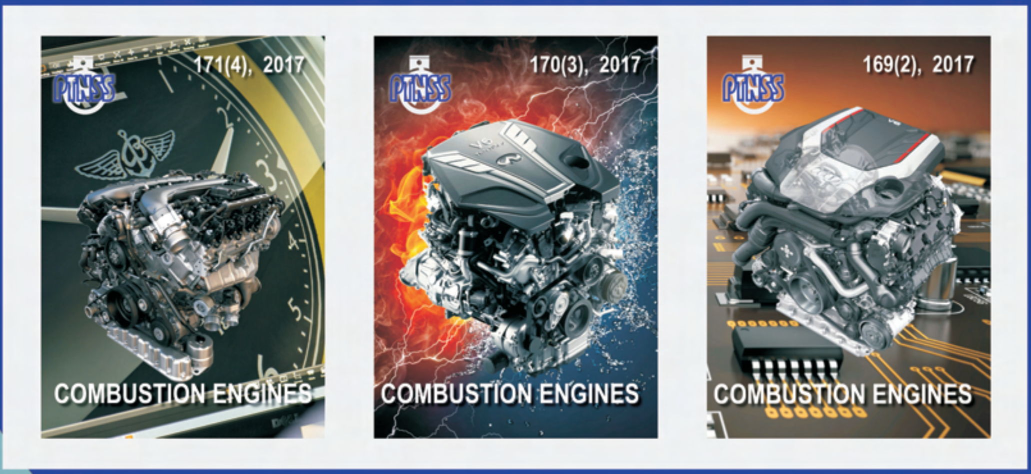

9 772300 989002

ISSN: 2300-9896

www.combustion-engines.eu